

PREDICTION OF PLASTIC INSTABILITY AND FORMING LIMITS  
IN SHEET METAL FORMING

A THESIS SUBMITTED TO  
THE GRADUATE SCHOOL OF NATURAL AND APPLIED SCIENCES  
OF  
MIDDLE EAST TECHNICAL UNIVERSITY

BY

BERKAY ŞANAY

IN PARTIAL FULLFILMENT OF THE REQUIREMENTS  
FOR  
THE DEGREE OF MASTER OF SCIENCE  
IN  
MECHANICAL ENGINEERING

SEPTEMBER 2010

Approval of the thesis:

**PREDICTION OF PLASTIC INSTABILITY AND FORMING LIMITS  
IN SHEET METAL FORMING**

submitted by **BERKAY ŞANAY** in partial fulfillment of the requirements for the degree of **Master of Science in Mechanical Engineering Department, Middle East Technical University** by,

Prof. Dr. Canan ÖZGEN  
Dean, Graduate School of **Natural and Applied Sciences**

\_\_\_\_\_

Prof. Dr. Suha ORAL  
Head of Department, **Mechanical Engineering**

\_\_\_\_\_

Prof. Dr. Suha ORAL  
Supervisor, **Mechanical Engineering Dept., METU**

\_\_\_\_\_

Prof. Dr. Bilgin KAFTANOĞLU  
Co-Supervisor, **Mechanical Engineering Dept., METU**

\_\_\_\_\_

**Examining Committee Members:**

Prof. Dr. Haluk DARENDELİLER  
Mechanical Engineering Dept., METU

\_\_\_\_\_

Prof. Dr. Suha ORAL  
Mechanical Engineering Dept., METU

\_\_\_\_\_

Prof. Dr. Bilgin KAFTANOĞLU  
Mechanical Engineering Dept., METU

\_\_\_\_\_

Assoc. Prof. Dr. Serkan DAĞ  
Mechanical Engineering Dept., METU

\_\_\_\_\_

Prof. Dr. Ali KALKANLI  
Metallurgical and Materials Engineering Dept., METU

\_\_\_\_\_

**Date:** 16.09.2010

**I hereby declare that all information in this document has been obtained and presented in accordance with academic rules and ethical conduct. I also declare that, as required by these rules and conduct, I have fully cited and referenced all material and results that are not original to this work.**

Name, Last name: Berkay ŞANAY

Signature :

# **ABSTRACT**

## **PREDICTION OF PLASTIC INSTABILITY AND FORMING LIMITS IN SHEET METAL FORMING**

Şanay, Berkay

M.Sc., Department of Mechanical Engineering

Supervisor: Prof. Dr. Suha Oral

Co-Supervisor: Prof. Dr. Bilgin Kaftanoğlu

September 2010, 130 Pages

The Forming Limit Diagram (FLD) is a widely used concept to represent the formability of thin metallic sheets. In sheet metal forming processes, plastic instability may occur, leading to defective products. In order to manufacture defect free products, the prediction of the forming limits of sheet metals is a very important issue. FLD's can be obtained by several experimental, empirical and theoretical methods. However, the suitability and the accuracy of these methods for a given material may vary.

In this study, FLD's are predicted by simulating Nakazima test using finite element software Pam-Stamp 2G. Strain propagation phenomenon is used to evaluate the limit strains from the finite element simulations. Two different anisotropic materials, AA2024-O and SAE 1006, are considered throughout the study and for each material, 7 different specimen geometries are analyzed. Furthermore, FLD's are predicted by theoretical approaches namely; Keeler's model, maximum load criteria,

Swift-Hill model and Storen-Rice model. At the end of the study, the obtained FLD's are compared with the experimental results. It has been found that strain propagation phenomenon results for SAE 1006 are in a good agreement with the experimental results; however it is not for AA2024-O. In addition, theoretical models show some variations depending on the material considered. It has been observed that forming limit prediction using strain propagation phenomena with FE method can substantially reduce the time and cost for experimental work and trial and error process.

**Keywords:** Forming Limit Diagram, Sheet Metal Forming, Nakazima Test, Strain Propagation, Finite Element Method

# ÖZ

## SAC METAL ŞEKİLLENDİRMESİNDE PLASTİK KARARSIZLIK VE ŞEKİLLENDİRME LİMİTLERİNİN BELİRLENMESİ

Şanay, Berkay

Yüksek Lisans, Makine Mühendisliği Bölümü

Tez Yöneticisi: Prof. Dr. Suha Oral

Ortak Tez Yöneticisi: Prof. Dr. Bilgin Kaftanoğlu

Eylül 2010, 130 sayfa

Şekillendirme Sınır Diyagramı (ŞSD) ince metal plakaların şekillendirilebilirliğini temsil eden sıkça kullanılan bir kavramdır. Sac metal şekillendirme uygulamalarında, kusurlu parçaların oluşmasına yol açan plastik kararsızlık meydana gelebilir. Kusuru olmayan ürünler üretmek için, sac metallerin şekillendirme limitlerinin tahmin edilmesi çok önemli bir konudur. ŞSD birçok deneysel ve teorik metotlarla elde edilebilir. Ancak, bu metotların uygunluğu ve doğruluğu belirlenmiş bir malzemeye göre farklılık gösterebilir.

Bu çalışmada, ŞSD'ları Pam-Stamp 2G sonlu elemanlar yazılım ile Nakazima testi simülasyonu yapılarak tahmin edilmiştir. Sonlu elemanlar simülasyonunda sınır gerilmeleri ölçmek için gerilim yayılma olgusu kullanılmıştır. İki farklı anizotropik malzeme, AA2024-O ve SAE 1006, çalışma boyunca ŞSD'larının değerlendirilmesinde ele alınmıştır ve her malzeme için 7 farklı numune geometrisi incelenmiştir. Ayrıca, ŞSD'ları teorik yaklaşımlarla, şöyle ki, Keeler modeli,

maksimum yük kriteri, Swift-Hill modeli ve Storen-Rice modeli ile tahmin edilmiştir. Bu çalışmanın sonunda elde edilen ŞSD'ları deneysel sonuçlarla karşılaştırılmıştır. Gerilim yayılma olgusu ile elde edilen sonuçların SAE 1006 malzemesi için deneysel sonuçlarla iyi bir uyum içinde olduğu bulunmuştur, oysaki AA2024-O için uyum içinde değildir. Ek olarak, teorik modeller değerlendirilen malzemeye bağlı olarak bazı değişimler göstermiştir. Şekillendirme sınırının sonlu elemanlar metodu ile gerilim yayılma olgusu kullanarak tahmin edilmesi, deneysel çalışma ve deneme yanılma süreçlerindeki zaman ve maliyeti oldukça düşürebileceği görülmüştür.

**Anahtar Kelimeler:** Şekillendirme Sınır Diyagramı, Sac Metal Şekillendirme, Nakazima Testi, Gerilim Yayılması, Sonlu Elemanlar Yöntemi

To My Parents

## **ACKNOWLEDGEMENTS**

I would like to express my gratefulness and appreciation to my supervisor Prof. Dr. Suha ORAL and my co-supervisor Prof. Dr. Bilgin KAFTANOĞLU for their guidance, encouragement, advice and insight throughout the study.

I would also to thank to the members of Metal Forming Center of Excellence at Atılım University, Ankara, TURKEY and Prof. Dr. Bilgin KAFTANOĞLU for their contributions and technical support for the whole study period.

In addition, I want to express my gratitude to Mr. Ahmet Kurt from ASELSAN for his comments and suggestions throughout the study.

Finally, I would like to thank my beloved family, Nusret Şanay, Emel Şanay, Bilge Şanay and my dear friends Serhat Yalçın and Celalettin Yumuş for their support and aid.

# TABLE OF CONTENTS

ABSTRACT .....	iv
ÖZ .....	vi
ACKNOWLEDGEMENTS .....	ix
TABLE OF CONTENTS .....	x
LIST OF FIGURES .....	xiii
LIST OF TABLES .....	xvii
LIST OF SYMBOLS .....	xviii
CHAPTERS	
1.INTRODUCTION .....	1
2.LITERATURE SURVEY .....	7
2.1 Deep Drawing .....	7
2.2 Stretch Drawing .....	10
2.3 Types of Defects .....	12
2.4 Previous Studies .....	13
3.OBJECT OF PRESENT INVESTIGATION .....	21
4.INSTABILITY CRITERIA AND FORMING LIMIT DIAGRAM .....	24
4.1 Maximum Load (ML) Instability .....	24
4.2 Strain Propagation Instability .....	28
4.3 Swift Model .....	29
4.4 Hill Model .....	33
4.5 Storen and Rice Instability Model .....	35
4.6 Keeler and Goodwin Model .....	42
5.FINITE ELEMENT METHOD .....	45
5.1 Review of Finite Element Analysis .....	45
5.1.1 Pre-processing .....	46

5.1.2 Solution .....	47
5.1.3 Post-processing .....	47
5.2 Modeling of Stretch Forming for Pam-Stamp .....	47
5.2.1 Mesh Generation .....	47
5.2.2 Analysis in Pam-Stamp .....	48
6.PREDICTION OF FLD BY SIMULATIVE TESTS.....	50
6.1 Nakazima Test.....	50
6.2 FE Simulations.....	53
6.2.1 Selection of Measuring Elements in FE Simulations.....	54
6.2.2 Analysis of SAE 1006.....	55
6.2.2.1 Radius=85mm .....	57
6.2.2.2 Radius=75mm .....	60
6.2.2.3 Radius=65mm .....	63
6.2.2.4 Radius=50mm .....	66
6.2.2.5 Radius=45mm .....	69
6.2.2.6 Radius=35mm .....	72
6.2.2.7 Radius=0mm .....	75
6.2.3 Analysis of AA2024-O .....	78
6.2.3.1 Width=30mm .....	81
6.2.3.2 Width=50mm .....	84
6.2.3.3 Width=70mm .....	87
6.2.3.4 Width=90mm .....	89
6.2.3.5 Width=110mm .....	90
6.2.3.6 Width=130mm .....	93
6.2.3.7 Width=200mm .....	94
6.2.4 Finite Element Predicted FLD .....	95
7.DISCUSSION OF RESULTS.....	96
7.1 Predicted Forming Limit Curves.....	96
7.2 Limit Strains of the Strain Propagation Analysis for SAE 1006 .....	100
7.3 Limit Strains of the Strain Propagation Analysis for AA2024-O .....	104
7.4 Results of Maximum Load Criteria for SAE 1006 .....	106

7.4.1 Radius=0mm .....	106
7.4.2 Radius=35mm .....	107
7.4.3 Radius=45mm .....	108
7.4.4 Radius=50mm .....	109
7.4.5 Radius=65mm .....	110
7.4.6 Radius=75mm .....	111
7.4.7 Radius=85mm .....	112
7.5 Results of Maximum Load Criteria for AA2024-O .....	113
7.5.1 Width=30mm .....	113
7.5.2 Width=50mm .....	114
7.5.3 Width=70mm .....	115
7.5.4 Width=110mm .....	116
7.6 Effects of Process Parameters .....	117
7.6.1 Friction .....	117
7.6.2 Strain Hardening Coefficient .....	118
8.CONCLUSION .....	121
REFERENCES.....	124
APPENDIX A. Hill’s Generalized Yield Criterion and Different Special Cases....	129

# LIST OF FIGURES

## FIGURES

Figure 1.1 Examples of Sheet Metal Products .....	1
Figure 1.2 Sample Stamped Products Used in Automotive Industry .....	2
Figure 1.3 Forming Methods Where the Deformation is Limited by Necking.....	3
Figure 1.4 Forming Limit Diagram.....	4
Figure 2.1 Examples of Drawn Products .....	7
Figure 2.2 Deep Drawing Tools.....	8
Figure 2.3 Deep Drawing Stages .....	9
Figure 2.4 Forces in Deep Drawing Process.....	10
Figure 2.5 Stretch Forming .....	11
Figure 2.6 Failure Modes, (a): wrinkling, (b): earing, (c): tearing.....	13
Figure 4.1 Stretching Process, (a): stresses on element of shell wall, (b): hemispherical punch and sheet metal.....	25
Figure 4.2 Force vs. Time .....	27
Figure 4.3 Strain Propagation .....	28
Figure 4.4 Equivalent Strain Increment vs. Time .....	29
Figure 4.5 Biaxial Stretching .....	30
Figure 4.6 Localized Necking Band.....	36
Figure 4.7 FLD Defined by Keeler .....	42
Figure 4.8 FLD Defined by Keeler and Goodwin.....	43
Figure 5.1 Finite Element.....	46
Figure 5.2 Initial Tool Positions.....	49
Figure 6.1 Nakazima Test .....	50
Figure 6.2 Zwick-Roell Sheet Metal Testing Machine.....	51
Figure 6.3 GOM Optical Measuring System .....	52

Figure 6.4 Nakazima Test Samples.....	52
Figure 6.5 Nakazima Tools.....	53
Figure 6.6 Nakazima Geometry of SAE 1006.....	55
Figure 6.7 Deformed States of the SAE 1006 Specimens.....	56
Figure 6.8 Deformed Geometry of R=85mm.....	57
Figure 6.9 Location of the Measuring Elements for R=85mm.....	58
Figure 6.10 Eqv. Strain Increments for the 1 <sup>st</sup> Group Elements of R=85mm.....	59
Figure 6.11 Eqv. Strain Increments for the 2 <sup>nd</sup> Group Elements of R=85mm.....	59
Figure 6.12 Deformed Geometry of R=75mm.....	61
Figure 6.13 Location of the Measuring Elements for R=75mm.....	61
Figure 6.14 Eqv. Strain Increments for the 1 <sup>st</sup> Group Elements of R=75mm.....	62
Figure 6.15 Eqv. Strain Increments for the 2 <sup>nd</sup> Group Elements of R=75mm.....	62
Figure 6.16 Deformed Geometry of R=65mm.....	63
Figure 6.17 Location of the Measuring Elements for R=65mm.....	64
Figure 6.18 Eqv. Strain Increments for the 1 <sup>st</sup> Group Elements of R=65mm.....	65
Figure 6.19 Eqv. Strain Increments for the 2 <sup>nd</sup> Group Elements of R=65mm.....	65
Figure 6.20 Deformed Geometry of R=50mm.....	66
Figure 6.21 Location of the Measuring Elements for R=50mm.....	67
Figure 6.22 Eqv. Strain Increments for the 1 <sup>st</sup> Group Elements of R=50mm.....	68
Figure 6.23 Eqv. Strain Increments for the 2 <sup>nd</sup> Group Elements of R=50mm.....	68
Figure 6.24 Deformed Geometry of R=45mm.....	69
Figure 6.25 Location of the Measuring Elements for R=45mm.....	70
Figure 6.26 Eqv. Strain Increments for the 1 <sup>st</sup> Group Elements of R=45mm.....	71
Figure 6.27 Eqv. Strain Increments for the 2 <sup>nd</sup> Group Elements of R=45mm.....	71
Figure 6.28 Deformed Geometry of R=35mm.....	73
Figure 6.29 Location of the Measuring Elements for R=35mm.....	73
Figure 6.30 Eqv. Strain Increments for the 1 <sup>st</sup> Group Elements of R=35mm.....	74
Figure 6.31 Eqv. Strain Increments for the 2 <sup>nd</sup> Group Elements of R=35mm.....	74
Figure 6.32 Deformed Geometry of R=0mm.....	76
Figure 6.33 Location of the Measuring Elements for R=0mm.....	76
Figure 6.34 Eqv. Strain Increments for the 1 <sup>st</sup> Group Elements of R=0mm.....	77

Figure 6.35 Eqv. Strain Increments for the 2 <sup>nd</sup> Group Elements of R=0mm.....	77
Figure 6.36 Nakazima Geometry of Aluminum .....	79
Figure 6.37 Deformed States of the AA2024-O Specimens .....	80
Figure 6.38 Deformed Geometry of W=30mm .....	81
Figure 6.39 Location of the Measuring Elements for W=30mm.....	82
Figure 6.40 Eqv. Strain Increments for the 1 <sup>st</sup> Group Elements of W=30mm .....	82
Figure 6.41 Eqv. Strain Increments for the 2 <sup>nd</sup> Group Elements of W=30mm.....	83
Figure 6.42 Deformed Geometry of W=50mm .....	84
Figure 6.43 Location of the Measuring Elements for W=50mm.....	85
Figure 6.44 Eqv. Strain Increments for the 1 <sup>st</sup> Group Elements of W=50mm .....	85
Figure 6.45 Eqv. Strain Increments for the 2 <sup>nd</sup> Group Elements of W=50mm.....	86
Figure 6.46 Deformed Geometry of W=70mm .....	87
Figure 6.47 Location of the Measuring Elements for W=70mm.....	87
Figure 6.48 Eqv. Strain Increments for the 1 <sup>st</sup> Group Elements of W=70mm .....	88
Figure 6.49 Eqv. Strain Increments for the 2 <sup>nd</sup> Group Elements of W=70mm.....	88
Figure 6.50 Deformed Geometry of W=90mm .....	90
Figure 6.51 Deformed Geometry of W=110mm .....	91
Figure 6.52 Location of the Measuring Elements for W=110mm.....	91
Figure 6.53 Eqv. Strain Increments for the 1 <sup>st</sup> Group Elements of W=110mm .....	92
Figure 6.54 Eqv. Strain Increments for the 2 <sup>nd</sup> Group Elements of W=110mm.....	92
Figure 6.55 Deformed Geometry of W=130mm .....	93
Figure 6.56 Deformed Geometry of W=200mm .....	94
Figure 7.1 Predicted FLC's of SAE 1006 .....	96
Figure 7.2 Predicted FLC's of AA2024-O.....	98
Figure 7.3 Minor and Major Strains of the Reference Elements for R=85mm .....	100
Figure 7.4 Minor and Major Strains of the Reference Elements for R=75mm .....	101
Figure 7.5 Minor and Major Strains of the Reference Elements for R=65mm .....	101
Figure 7.6 Minor and Major Strains of the Reference Elements for R=50mm .....	102
Figure 7.7 Minor and Major Strains of the Reference Elements for R=45mm .....	102
Figure 7.8 Minor and Major Strains of the Reference Elements for R=35mm .....	103
Figure 7.9 Minor and Major Strains of the Reference Elements for R=0mm .....	103

Figure 7.10 Minor and Major Strains of the Reference Elements for W=30mm ....	104
Figure 7.11 Minor and Major Strains of the Reference Elements for W=50mm ....	105
Figure 7.12 Minor and Major Strains of the Reference Elements for W=70mm ....	105
Figure 7.13 Minor and Major Strains of the Reference Elements for W=110mm ..	106
Figure 7.14 Load vs. Punch Progression of Specimen R=0mm .....	107
Figure 7.15 Load vs. Punch Progression of Specimen R=35mm .....	108
Figure 7.16 Load vs. Punch Progression of Specimen R=45mm .....	109
Figure 7.17 Load vs. Punch Progression of Specimen R=50mm .....	110
Figure 7.18 Load vs. Punch Progression of Specimen R=65mm .....	111
Figure 7.19 Load vs. Punch Progression of Specimen R=75mm .....	112
Figure 7.20 Load vs. Punch Progression of Specimen R=85mm .....	113
Figure 7.21 Load vs. Punch Progression of Specimen W=30mm .....	114
Figure 7.22 Load vs. Punch Progression of Specimen W=50mm .....	115
Figure 7.23 Load vs. Punch Progression of Specimen W=70mm .....	116
Figure 7.24 Load vs. Punch Progression of Specimen W=110mm .....	117
Figure 7.25 Effect of Friction on the Position of Necking.....	118
Figure 7.26 Necking State of the Specimen W=30mm .....	119
Figure 7.27 Thickness Strain History of el.no.57572 .....	120

# LIST OF TABLES

## TABLES

Table 6.1 Process Parameters.....	54
Table 6.2 Chemical Composition of SAE 1006.....	55
Table 6.3 Material Properties of SAE 1006.....	55
Table 6.4 SAE 1006 Blank Finite Elements .....	57
Table 6.5 Chemical Composition of AA2024-O .....	79
Table 6.6 Material Properties of AA2024-O.....	79
Table 6.7 AA2024-O Blank Finite Elements.....	81

## LIST OF SYMBOLS

$\varepsilon_1^*$	: Major limit strain
$\varepsilon_2^*$	: Minor limit strain
$\varepsilon_{1r}$	: Principal strain in radial direction
$\varepsilon_{2c}$	: Principal strain in circumferential direction
$\varepsilon_3$	: Thickness strain
$\varepsilon_1$	: Principal strain in major strain direction
$\varepsilon_2$	: Principal strain in minor strain direction
$\sigma_{1r}$	: Radial stress
$\sigma_1$	: Major principle stress
$\sigma_2$	: Minor principle stress
$\sigma_0$	: Yield stress for uniaxial tension
$\sigma_{ij}$	: Components of stress tensor
$\varepsilon_e$	: Equivalent strain
$\sigma_e$	: Equivalent stress
$\lambda$	: Proportionality factor
$K$	: Strength coefficient
$F$	: Traction force
$\psi$	: Angular coordinate in horizontal plane
$\theta$	: Angle between the normal and $x_1$ direction
$a, b, c, f, g, h$	: Constants in Hill's yield criterion
$n$	: Strain hardening exponent
$M$	: Exponent in Hill's yield criterion
$R$	: Anisotropy value
$r$	: Current radius to center of shell wall

$r_0$	: Initial radius to center of shell wall
$R_0$	: Anisotropy value at rolling direction
$R_{90}$	: Anisotropy value at transverse direction
$R_{45}$	: Anisotropy value at 45° to rolling direction
$t$	: Thickness
$t_0$	: Initial thickness
$\alpha$	: Stress ratio ( $\sigma_2 / \sigma_1$ )
$\rho$	: Strain ratio ( $\varepsilon_2 / \varepsilon_1$ )
$f$	: Yield function
$n_1, n_2$	: Components of the unit normal to the neck
$Q$	: Load
$\mu$	: Coefficient of friction
$a$	: Yield criterion constant

# CHAPTER 1

## INTRODUCTION

The technology of sheet metal forming has a very high importance in manufacturing. In the last decade, due to the inventions and developments of the new materials and their high quality and enhanced functionality, sheet metal forming became more popular, its application areas are extremely increased and it turned out to be one of the most preferable manufacturing techniques in industry around the world. It has a wide application area especially in automotive industry, domestic appliances, building products, aircraft industry, food and drink cans etc. Due to increase in application areas and the demand, the variety and complexity of the products are increased as well and there is a need to manufacture higher quality products in order to become a strong competitor in industry.



**Figure 1.1 Examples of Sheet Metal Products**

In an engineering point of view, the functionality and the suitability of the product should be analyzed extensively before manufacturing it in high volume. The most appropriate material and the production method under specified conditions should be selected cautiously by taking the total manufacturing cost into account. In today's technology, finite element method (FEM) is the most common method used for this purpose. By achieving FEM analysis, an engineer can investigate if a product will fail or not before manufacturing a real product. If a product fails in the analysis, the process parameters can be redefined or a new material can be used. Therefore, before starting a manufacturing in the workshop, it is important to perform a good and systematic analysis in evaluating which forming method is the most suitable to manufacture a given product with a desired quality and lowest manufacturing cost.

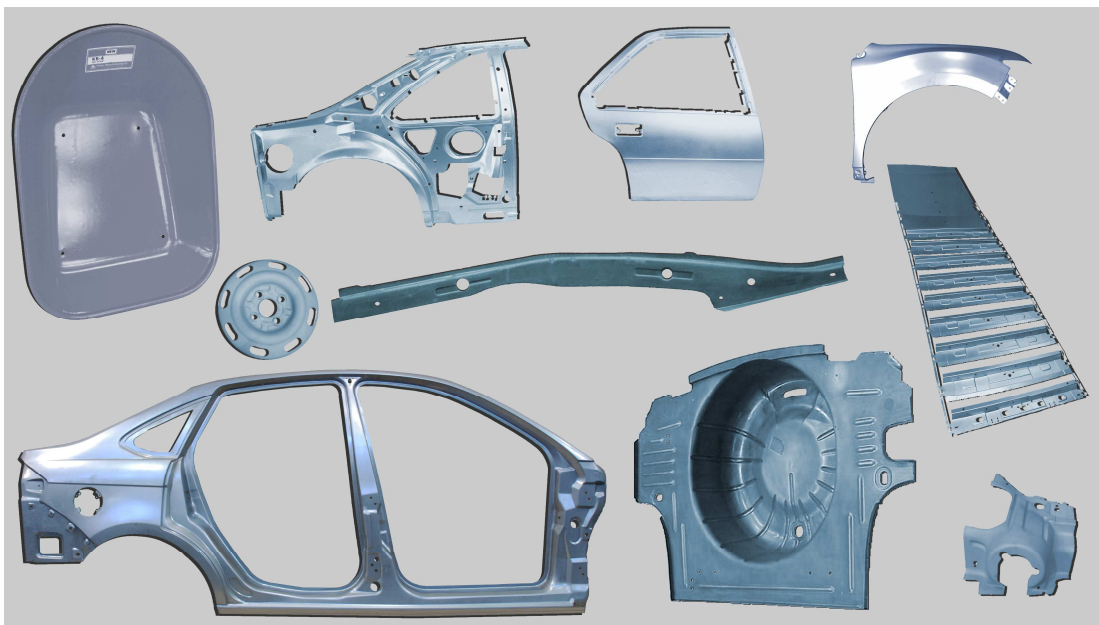


**Figure 1.2 Sample Stamped Products Used in Automotive Industry**

Sheet metal forming can be defined as the ability of metal to deform plastically or changing the shape of the sheet into a new desirable shape without necking or crack. The material properties and process parameters has a crucial role in all of the sheet metal forming operations. As an illustrate, for a deep drawing operation, material properties of the material such as yield strength, elastic modulus, anisotropy ratio,

strain hardening coefficient etc. and the process parameters as punch & die geometry, lubrication, punch speed and blank holder force determines the forming quality of the process. Therefore, a suitable material selection and determining optimum forming parameters is a must for a successive sheet metal forming process.

According to Marciniak and Duncan [1], a large number of techniques are used to achieve sheet metal parts. The common sheet metal forming processes can be listed as blanking and piercing, bending, stretching, hole extrusion, stamping, deep drawing, tube forming, fluid forming, coining and ironing (Figure 1.3). As generally known, sheet metal parts have the advantage that the material has a high elastic modulus and high yield strength so that the parts produced can be stiff and have a good strength to weight ratio. However, as previously stated, for a given process and deformation geometry, the forming limits vary from material to material. The basic concern is whether the desired deformation can be accomplished without failure of the work piece. Therefore, the research and development studies are still being made in order to evaluate the forming limits of the sheet metals.

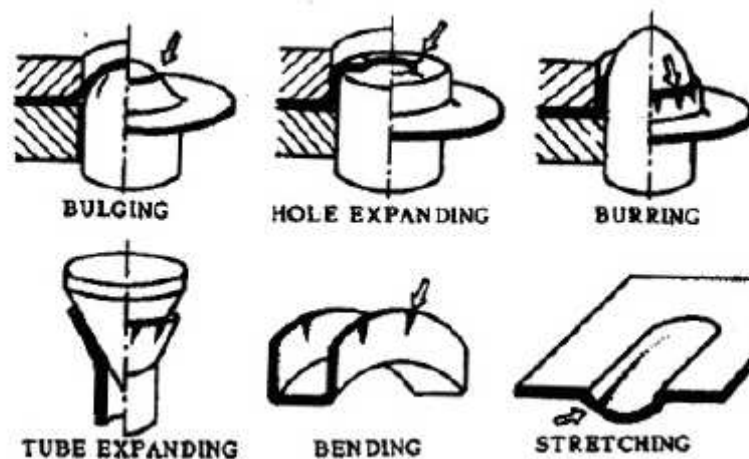


**Figure 1.3 Forming Methods Where the Deformation is Limited by Necking [2]**

To control the operation of sheet metal forming without failure, a diagram is used in which the safe, critical and failure forming regions are shown. This diagram is known as the Forming Limit Diagram (FLD). In sheet metal industry and studies, it

is widely used and considered as one of the important tool to determine the formability of sheet metals. Every sheet metal has its own forming limit diagram which determines its formability, strain limit and forming regions.

Forming limit diagram is a representation of the critical combination of the two principal surface strains major and minor above which localized necking instability is observed. For varying strain ratios, from pure shear to equibiaxial tension, the forming limit curve is plotted. When the strain ratio is positive, in other words where minor strain is positive, it means stretching is observed. In case of negative strain ratio, in other words negative minor strain, one can conclude that drawing is observed. It should also be noticed that the strains plotted are true strains.

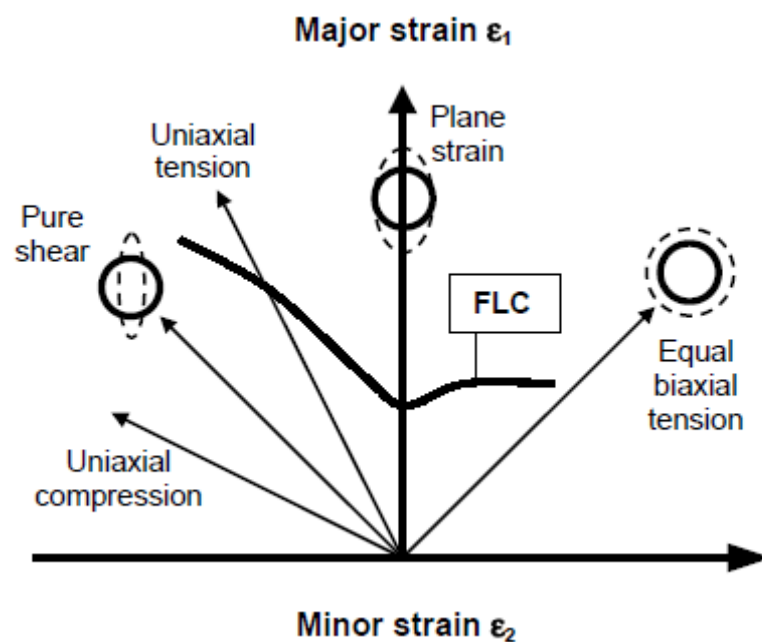


**Figure 1.4 Forming Limit Diagram**

In order to analyze the sheet metal instabilities and construct the FLD, various experimental and theoretical approaches exist.

Several types of experimental testing procedures are presented in literature in order to obtain the forming limit curves of different materials (aluminum alloys, steel,

copper, brass). Uniaxial tensile test, hydraulic bulge test, punch stretching test, Keeler test, Hecker test, Marciniak test, Nakazima test are some of the experimental procedures [3]. In uniaxial tension test, the frictional effects are eliminated and only the negative range of FLD ( $\varepsilon_2 < 0$ ) can be obtained. The hydraulic bulge test is performed to determine only the positive range of FLD ( $\varepsilon_2 > 0$ ) by changing the shape of the elliptical dies to obtain different strain paths. The frictional effects are also eliminated in this test. Next, punch stretching test can be used to obtain the FLD. In this test the specimen is clamped between a die and a blank holder and stretched by a hemispherical or elliptical punch. Different strain paths are obtained by varying the specimen geometries. Keeler test consist the use of punches of different radius to obtain different stress states to obtain the positive ( $\varepsilon_2 > 0$ ) range of FLDs. The main disadvantage of the test is the need for high amount of experimental work. By varying the friction regime, using the same die and specimen geometries the positive range of FLD can be obtained by Hecker test. Then, in Marciniak test a hollow punch is used. There is an intermediate part which has a circular hole is placed between the work piece and the punch. The aim is to obtain the tearing at the planar bottom section of the cup, otherwise cracks occurs between the cylindrical wall and the bottom. Complex geometries of punches and dies are required and there is a limitation for the positive range of the FLD. By using different specimen geometries and intermediate parts full range of FLD can be obtained. Finally, Nakazima test can be used to obtain the full range of FLD. By drawing the specimens with hemispherical punch and a circular die for varying widths, different strain paths can be obtained.

From all of the above tests, Nakazima test seems to be the most powerful and advantageous test because the tools used for the test is simple, the geometries of the specimens are not complex and full range of the FLD can be determined. Today, it is widely used in industry and sheet metal testing laboratories in order to evaluate the forming limits of the sheet metals.

In addition to these experimental studies, theoretical and empirical studies have also been performed to evaluate formability of the sheet metals.

Several researchers have been studied on the prediction of FLDs by analytical and theoretical methods. First some empirical models [4-5] are developed. Then, there occurred a need for the more accurate theoretical methods. Theoretical and numerical determination of FLDs is commonly based on localization criteria. Localization criteria based on the maximum load principle [6, 7], bifurcation analysis [8-10], limit stress analysis [11-14] and strain propagation [15] exists in literature with their drawbacks and limitations. The suitability of the proposed methods has been investigated for various materials and the new approaches are still being developed with the advances in technology.

In this study, the formability of sheet metals is predicted by simulating Nakazima testing method with performing finite element analysis in commercial FE software PAM-Stamp. Strain propagation criterion by Kaftanoğlu [15] is utilized in evaluating the forming limit strains from FE solution. FLD are also obtained applying theoretical foundations of Swift and Hill [6-7], Storen-Rice [8-10], Keeler [4-5] and maximum load condition [15]. In all the analysis, material anisotropy is taken into account for the Aluminum (AA2024-O) and Steel (SAE 1006) materials. The obtained results are compared with the experimental findings and the validity of the theoretical models and the FE simulation results are discussed.

## CHAPTER 2

### LITERATURE SURVEY

A survey of previous work held on the construction of theoretical forming limit diagrams as well as experimental studies.

Since, forming limit diagram studies and experiments based on mainly stretching operations like deep drawing and stretch forming, the deformation phenomena of the stretching operations are introduced first. Special attention is given to tensile instability failure models and localized instability.

#### 2.1 Deep Drawing

Deep-drawing is one of the methods in metal forming which is used to manufacture products from sheet metal. Nowadays, the application areas are too broad and getting wider with time. Automotive body panels, some airplane parts, cans, sinks, houses, various cups are some of the deep-drawn examples (Figure 2.1).



**Figure 2.1 Examples of Drawn Products**

The simplest deep drawing operation can be done to form a cylindrical cup. In most of the experiments and samples, cylindrical cup is formed because of the ease in analyzing of the axisymmetric geometry. The most common necessary tools for the process are shown in Figure 2.2.

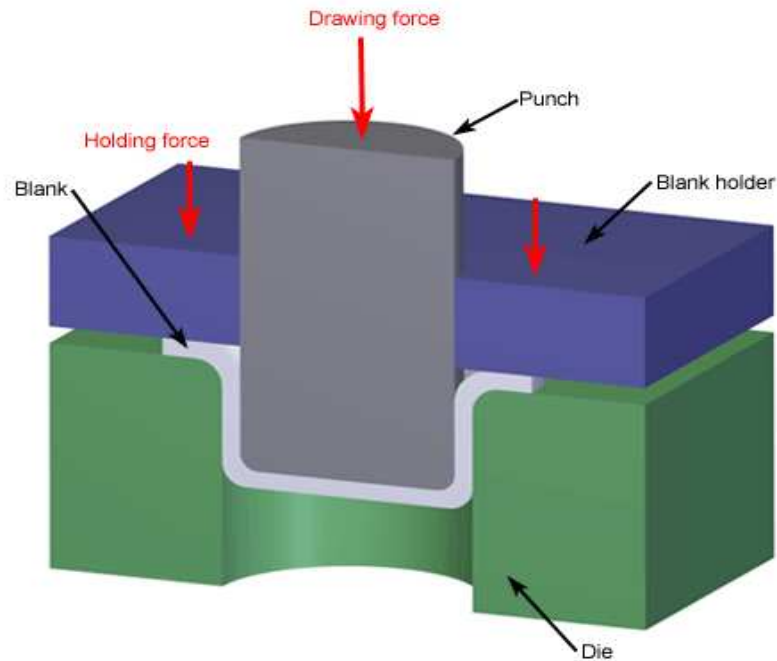


**Figure 2.2 Deep Drawing Tools**

As can be seen in Figure 2.2, initially the flat sheet material is placed between the die and the blank holder. Punch is placed at the same central axis with the die. The region where the material exists between the die and the blank-holder, between the punch and the die-wall and at the surface of the punch head is called the outer annular zone, the inner outer zone and the central zone, respectively. As the draw proceeds, the material at the outer annular zone is drawn inwards towards the profile of the die under the effect of radial tensile stress. Since the radius of the material at this zone is decreased, a compressive hoop stress is developed and that causes an increase in material thickness. In order to prevent this thickness increase at this region, blank-holder is used. Otherwise, wrinkling or folding occurs at this flange region. As the material flows over the die profile, thinning occurs due to the plastic

bending under tensile stress. Besides, because of the tensile behavior between the die and the punch, the inner part of the outer annular zone continues thinning.

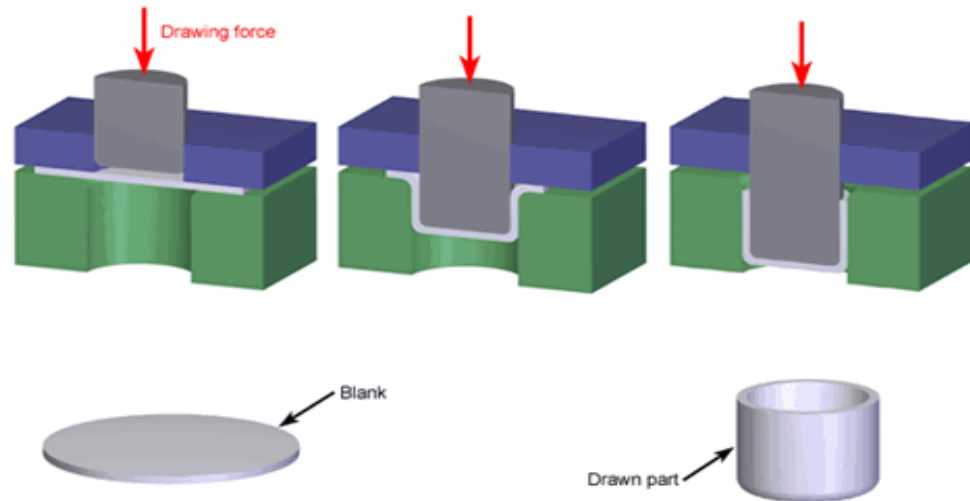


**Figure 2.3 Deep Drawing Stages**

If the inner annular zone is examined, bending and sliding effects over the die profile can be observed. This is because of the tension between the punch and the die and the bending and sliding over the punch.

At the central region, stretching and sliding is observed at the punch head. This is determined by the friction between the contacting surfaces and the developed strain depending on the punch head profile.

To summarize, the types of deformation occurs in a deep-drawing process can be listed as,

- 1- Pure radial stress between die and blank-holder,
- 2- Bending and sliding over the die profile,
- 3- Stretching between die and punch,

- 4- Bending and sliding over the punch profile radius,
- 5- Stretching and sliding over the punch head.

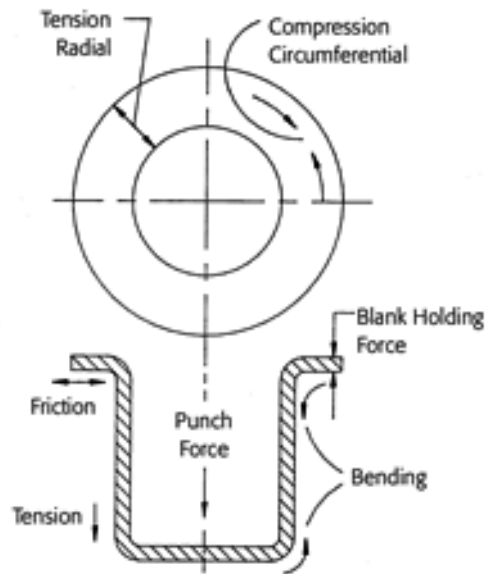


**Figure 2.4 Forces in Deep Drawing Process**

Note that, thickening occurs at the first deformation mode only. For the other four processes, thinning occurs.

Sheet metal forming processes and especially deep-drawing is highly influenced by the type of the material. Depending on the industrial needs, because of the strength, weight, formability and cost considerations, new materials are developed or tried to be integrated in production processes. Therefore, the tool design and the process parameters change in the production processes and these results advancing the research and development in these fields.

## 2.2 Stretch Drawing

Stretch forming is very similar to deep drawing, which can be defined as the forming of a sheet blank with a rigid punch, whereby the blank is rigidly clamped at the

edges. The blank can be clamped between rigid tools, corresponding to the upper and lower drawing frames of the conventional tools, or be clamped in gripping jaws.

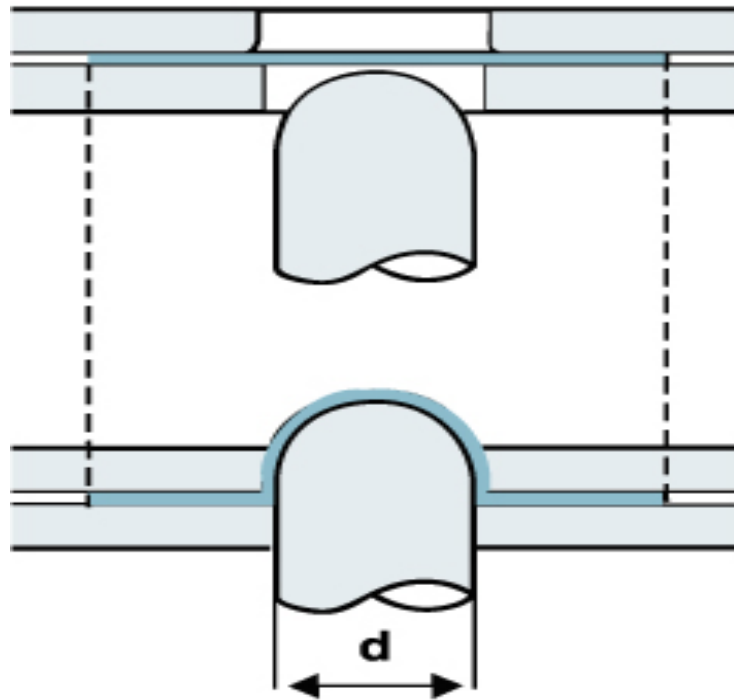


**Figure 2.5 Stretch Forming**

Stretch forming is a very accurate and precise method for forming metal shapes, economically. This process is ideally suited for the manufacture of large parts made from aluminum, but does just as well with stainless steel and commercially pure titanium. It is quick, efficient, and has a high degree of repeatability. In addition, it is a very common method that is used for the formability tests of sheet metals.

The variety of shapes and cross sections that can be stretch formed is almost unlimited. Window systems, skylights, store fronts, signs, flashings, curtain walls, walkway enclosures, and hand railings can be accurately and precisely formed to the desired profiles. Close and consistent tolerances, no surface marring, no distortion or ripples, and no surface misalignment of complex profiles are important benefits inherent in stretch forming.

### 2.3 Types of Defects

There are various types of failures that can be observed in drawing operations [3]: wrinkling, earing, surface failures and necking & tearing (Figure 2.6).

Wrinkling generally takes place in the flange region under the effect of pure radial drawing. If the radial drawing stress exceeds a certain value, compressive stresses in the circumferential direction gets too high and these stresses results in buckling, so called wrinkling, in deep-drawing process. In order to prevent wrinkling either blank-holder or draw beads can be utilized.

Earing and surface defects like traces or luders strips may occur due to the irregularities of the tools, the friction regime, material properties and the geometrical properties of the blank. In order to produce a defect-free product, the tool selection and design should be done properly and the material properties and the geometry of the blank should satisfy the process requirements.



(a)



(b)



(c)

**Figure 2.6 Failure Modes, (a): wrinkling, (b): earing, (c): tearing**

In stretching and stamping operations the main type of defect is tearing which begins with localized necking. For cup drawing or stretching a work piece with a hemispherical punch, tearing is mainly observed along the punch radius; but it could also be observed at the pole or at the bottom section of the cup depending on the friction conditions. Tearing or localized necking is a limiting factor for the manufacturing of sheet metals.

Necking prediction and material limits has a very critical role in sheet metal forming processes. First of all, the necessary tools required for the process is directly depend on that knowledge. Secondly, the final product quality is substantially increased. Furthermore, the trial and error process is decreased and the production times are highly reduced. As a result, the total cost for the process is remarkably decreased. So, the good knowledge of the necking phenomena for the designer is a must for the stretching and stamping operations.

## **2.4 Previous Studies**

In order to analyze the sheet metal instabilities and construct the FLD, various theoretical and experimental approaches exist in literature.

Keeler and Backofen [4] is first investigated the FLD phenomena by stretching the sheet metals biaxially and examining failure mechanism. They postulated that as the degree of biaxiality increases, the maximum principal strain before the occurrence of localized thinning increases too. By stretching the sheet metals with solid punches, several materials have been tested such as aluminum, steel, copper and brass. Next, Keeler [5] observed that the material properties of sheet metals have very high influence on the distribution of strains in biaxial stretching process. As the strain hardening exponent,  $n$ , increases more homogenous strain distribution is obtained, however for lower  $n$  values, sharp strain gradients develop and the strain localize in a small area and that cause premature failure on the material. Then, Keeler prepared a map which the safe and critical regions are separated in principal strain space ( $\varepsilon_1, \varepsilon_2$ ). He defined the major and minor strains,  $\varepsilon_1$  and  $\varepsilon_2$  respectively. Goodwin [16], then continued studying on the experimental techniques and for mild steel FLD is obtained. The FLDs cover different strain states form uniaxial tension to biaxial stretching cases. This is considered as a basic criterion for most sheet metal stamping processes. The obtained FLDs for carbon-steel stampings are named as Keeler-Goodwin diagrams because of the extensive and important studies of Keeler and Goodwin on the sheet metal formability.

Later, Swift and Hill [6-7] developed a theoretical modal for the instability analysis of materials. Swift developed diffuse necking theory for a biaxially loaded element, which his analysis is based on the maximum force. The right hand side of the FLD, where both major and minor strains are positive, is determined. Then, Hill proposed the localized necking phenomena, which the left hand side of the FLD is covered. According to his theory, localized neck develops along zero elongation direction. The diffuse and localized necking theories are used together in constructing FLD. In addition, both of the theories can be applied for the anisotropic materials. The mathematical formulations and more detailed description of Swift and Hill theories are given in Chapter 4.

The model of localized necking which is based on the vertex theory is developed by Storen-Rice [8]. In this model, localized necking is caused by the vertex developed

on the subsequent yield surface. The J2 deformation theory of plasticity is employed instead of the usually adopted flow theory. This method can predict the localized necking over the entire range of FLD, especially, it agrees with test data on the RHS of FLD for strain rate insensitive materials such as aluminum alloys. However, it underestimates the limit for localized necking at the LHS of FLD. Zhu, Weinmann, Chandra [9] considered the moment equilibrium in addition to the force equilibrium condition adopted by Storen-Rice. They also found that the discontinuity of shear stress inside and outside of the localized band is actually zero. Therefore, the Storen-Rice method is simplified. The modified model achieves good prediction at the LHS of FLDs. Since the Storen-Rice method relies on the deformation theory of plasticity, it is only valid under the proportional loading condition.

Sing Rao [13] proposed a method to predict FLD from FLSD which is based entirely on material properties readily measured from simple tensile tests alone. Starting from the knowledge of single limit yield stress, e.g. localized tensile stress, a continuous yield stress locus based on any one of the different cases of the generalized Hill's anisotropic criterion could be developed. Since, such an FLSC is usually elliptical in shape; they employed the linear regression technique to obtain the FLSC as a straight line. From this linear FLSC, they deduced the corresponding FLC in conjunction with the strain hardening law, normality flow rule and the selected case of the Hill's yield criterion. The obtained FLCs exhibited good correlation with the experimentally determined FLCs, in case of steel and copper alloys. They exhibited that the obtained FLCs derived from elliptical or a piecewise linear FLSC do not in a good agreement with the experiments. They also showed that the different cases of Hill's yield criterion and the values of Hill's exponent  $M$ , give wide range of FLCs. Sing-Rao model make possible to deduce different FLCs corresponding to different strain paths from single FLSC which is independent of strain path.

Kaftanoğlu [15] presented a theoretical and experimental study of the plastic deformation and an investigation of instability and fracture in the stretch forming process. In his study, he suggested more refined theoretical methods for analyzing drawing over die surface in deep drawing and for hydraulic bulging. In addition, he

developed two possible methods to determine the coefficient of friction in sheet metal deformation processes. Also, an empirical method of estimating L.D.R in deep drawing, and an experimental investigation of the factors influencing the Erichsen number, and some deep drawing experiments are presented. For the tensile instability in sheet metal deformation processes, he suggests three methods which are maximum load, maximum pressure and strain propagation. For the maximum load instability, he states that after reaching a critical load value, instability occurs along the surface of the sheet metal. Second, the maximum pressure criterion is presented and it is shown that for some materials instability takes place after a critical pressure limit. Kaftanoğlu also developed a new instability criterion which is based on the transfer of strains between 2 neighboring elements. He postulates that if the strain rate of an element increases, the neighboring elements' strain rate should also increase. If not, then instability occurs at this region of the sheet metal. In his study, for the stretch forming and deep drawing tests performed for steel, aluminum, copper and brass materials, the results show that the maximum load instability and strain propagation instability criterion give very close results to the experiment in most cases. However, the maximum pressure criterion gave much lower and unsatisfactory results.

To predict the FLD for sheet metal forming under a linear strain path, Banabic and Aretz [17] focused on a comparison between different modeling approaches. In this study, orthotropic yield criterion developed by BBC2003 [18] is used in four models, namely as Marciniak-Kuczynski model, the modified maximum force criterion (MMFC) according to Hora [19], Swifts' diffuse [6] and Hill's localized necking approach [7]. In the conducted experiment, 1mm thickness AA5182-O aluminum sheet alloy is used and the strain localization simulation is performed by the commercial finite element code ABAQUS. At the end of the analysis, M-K model and the finite element based approach agreed with each other and experimental FLD. However, the other approaches overestimated the experimental FLD.

Arrieux [20] studied on the prediction of the onset of necking in deep drawing process by using a numerical method. In the analysis, the forming limit stress surface of a sheet metal is determined based on M-K model. Then a theoretical model

showing non-linear strain paths is presented and the previously obtained stress surface is implemented in finite element software to obtain the occurrence of necking during the drawing of a square cup. The occurrence of necking is checked by looking the positions of the points on the diagram, which includes the two principle stresses and the angle of principle direction.

A rigid plastic solution to the deep drawing of a square cup based on membrane theory and finite-strain formulation is presented by Toh and Kobayashi [21]. In the analysis, Hill's yield criterion including anisotropy is studied. In the simulation of the drawing process, blank holder is used. Square cup experiments are conducted and the results are compared with the theoretical findings. A good agreement is obtained in the results. In addition, the importance of lubrication on the drawing process is observed.

Siguang Xu [22], studied on the prediction of the FLD for the production of the automotive aluminum body panels. Using Hill's 1993 yield criterion he proposed a method to develop forming limits. He compared the predicted limit strains based on both Hill's 1948 and 1993 yield criterion with experimental data. He found that localized necking in aluminum sheets can be characterized better with Hill's 1993 yield criteria than Hill's 1948. Besides, he developed a critical thickness strain criterion to represent the variation of forming limits in the negative minor strain region.

R.Mahmudi [23] studied on predicting the forming limit diagram by idealizing the three phase deformation criterion of John-Gillis into certain mathematical assumptions, together with the mathematical approximations to the material behavior and boundary conditions that lead to solvable mathematical problems. Phase 1 is homogenous deformation up to maximum load, phase 2 indicates deformation localization under constant load and phase 3 is local necking with an instantaneous drop in load. In the analysis, differential equations for the left and right hand sides of the forming limit diagram are developed during phase 2, where diffuse necking occurs. Then, a mathematical relation is obtained to find the strain rate of both sides

of the FLD by using previously calculated thinning rate for phase 3, localized necking. The predicted forming limit results obtained for different hardening laws are compared with the experimental results conducted with the two types of aluminum materials AA8011 and AA3105, respectively. The effect of anisotropy ratio and work-hardening coefficient on forming limits is also investigated.

Forming limit curve is also investigated by Wang and Lee [24]. They compared different yield criteria results by both performing numerical simulation and experiments and analyzed the effects of different yield criteria in the strain path evolution. The theoretical FLC is obtained using Swift model which considers Hill 48; Hill 90 and Hill 93 yield criteria whereas the numerical simulation is carried out by using Hill 48 and Hill 90. SPCC (JIS G3141) and Al6xxx are used as sample material types. At the end of the analysis, for both materials, Hill 90 and Hill 93 gave accurate results. For SPCC, yield values varied with different yield criteria whereas for Al6xxx, Hill 48 underestimated the yield stress values when compared with Hill 90 and Hill 93.

Influence of loading path on the plastic instability strain in anisotropic plane sheets is investigated by Chakrabarty and Chen [25]. In their study, the effect of varying stress ratio under constant loading on the onset of tensile instability is analyzed. The sheet metal is assumed to have a normal anisotropy and uniform strain ratio  $R$ . Analytical relations are derived for the effective strain and the principle surface strains at the point of instability in terms of initial and final stress ratios.

Bleck and Deng [26] achieved a comparative study of two FLD models based on the Swift and Hill instability criterion as well as on an empirical model proposed by the NADDRG and experimental FLDs has been carried out for various kinds of steels. They focused on the differences between the approaches in predicting the FLD and investigated the effects of strain hardening on the calculated FLDs. First the theoretical model is considered based on the Hill's criteria. Then the FLD models based on the Swift-Hill model is investigated and the minor and major forming limit strains are formulated. After conducting the experiments for various kind of steels

and obtaining the FLD according to NADDRG model, comparison of the results are made. It is shown that the models based on Swift-Hill instability criteria are different in their basic flow rules. In addition, FLD is affected by the thickness, the yield and tensile strength, and the strain hardening and strain rate sensitivity. Lastly, it is concluded that none of the models can predict the FLD reliably.

A comparative study to predict the FLD is also made by Slota and Spisak [27]. Three mathematical models (M-K model, Hill-Swift model and Sing-Rao model) as well as the empirical model by the NADDRG are investigated and their results are compared with the experimental results. The types of the steel materials used in the experiments are, DX 54D, DX 53D, ZStE220P and ZStE340. At the end of the study, it is observed that there is no one model that can be used for every material. Sing – Rao model seems to be in good correlation with the experimental results for some steels and Hill-Swift and M-K models gave too small  $FLD_0$  values.

Pepelnjak and Kuzman [28] presented a methodology to determine the entire range of FLD by simulating the Marciniak Test with the commercial FE software ABAQUS. Two types of deep drawing steels, an aluminum 3000 alloy and a Ti-alloy are tested to assure the validity of the test. In the applied analysis, first the thicknesses of the critical nodes are searched and the thinning values as a function of time are obtained. Then, for the critical nodes, first and second temporal derivations of thickness strains are calculated. At the necking point, there exists a sudden local change in thickness strain. To find the location of critical node and the time for the localized necking state, a signal processing algorithm is developed. The obtained results for this method seem to be parallel with the experimental findings, although for Al-3000 material the right hand side of the FLD is not predicted accurately.

Huang, Tsai and Li [29] studied on the effects of blank and fractured thickness on the forming limits of sheet metals. In the tension test, the thickness at the fractured state is considered as the fracture criterion and is integrated to a previously developed FEM code. The fracture model is based on the updated Lagrangian formulation, Prandtl-Reuss flow rule and Hill's yield criterion and it is stated that the fracture

takes place when the blank thickness becomes equal to the fractured thickness. In this study, uniaxial tension test is performed and all the material properties and fracture thickness are obtained. Furthermore, after manufacturing necessary tools for the square cup drawing and elliptical hole flanging processes, experiments are performed. To validate the theory, square cup drawing and elliptical hole flanging processes are simulated using FEM and there seems to be a good correlation between the experimental and numerical results.

The forming limits of stainless steel tailor-welded blanks (TWB) are investigated by Jie, Cheng, Chow and Chan [30]. Firstly, by using LS-Dyna, the numerical simulations of the Limit Dome Height (LDH) test are performed for various TWB orientations and blank widths. Then, experimental LDH tests are conducted accordingly. Vertex theory [8] is considered as the localized necking criterion and this criterion is implemented into a computer code and processed with the FEM outputs. The maximum drawing heights and the location of the necking are calculated and presented. Finally, the predicted results are compared with the experiments and it is observed that the failure locations and the drawing depths values of the specimens are slightly different for numerical and experimental results. The reasons are given as because of the assumption of proportional loading in the vertex theory, the choice of frictional constant between the tools and the blank, the type of the finite element (2D-shell), the stress concentration at the thickness transition area and the prediction of failure only in the base metal.

## **CHAPTER 3**

### **OBJECT OF PRESENT INVESTIGATION**

In sheet metal forming operations, forming limit prediction is a very important issue that should be analyzed carefully in order to produce higher quality products. The determination of the best forming technique and the most suitable material for a product directly depend on the extensive knowledge of the deformation limits of the material. Without knowing the deformation limits and the right forming parameters of the material, the trial and error processes continues again and again. It results in spending high amount material and producing high number of manufacturing tools. Therefore, facing with a huge amount of manufacturing costs and high wasted times are unavoidable.

For the determination of the forming limits of a material, the trial and error process in digital environment should be achieved and today FEM is the most effective and preferable tool for this purpose. As an illustrate, for a deep drawing and stretch forming operation, material flow, failure modes and required strain and stresses could be evaluated and analyzed very fast and precisely using FEM. Today, high number of commercial FE software packages exists and lots of finite element studies are published and can be found in literature.

Forming limit diagram is the tool commonly used for the determination of the forming limits of a material. It separates the region where the material will fail or not for the applied forming conditions. In FLD, two types of strains, namely major and minor, are shown. For different loading conditions, from pure shear to equibiaxial tension, forming limit curve is plotted and it is stated that the region under this curve is safe but for the above region localized necking takes place and material fails.

FLD can be obtained by several experimental, theoretical and numerical techniques. Most of the researchers preferred to use experimental techniques which are time consuming and costly but accurate FLDs are obtained. In literature, lots of experimental techniques are applied which are previously referred in chapter 1. However, in the last decade, the usage of numerical techniques, especially FEM, became more and more popular due to its accurate and faster solution abilities. Besides, theoretical approaches still valid and effectively applied for some materials with developing new solution strategies and integrating newer formulations and failure criteria.

In this work, the formability of sheet metals, especially necking failure, is predicted using FEM and theoretical methods. Nakazima testing method for the determination of FLD is simulated by applying strain propagation criteria using FE software and various theoretical methods are used to obtain the forming limit curves of SAE 1006 and AA2024-O. The obtained results are compared with the experimentally found FLDs and the validity and effectiveness of each method are discussed.

In the 1<sup>st</sup> Chapter, a brief introduction of the sheet metal forming and the importance of the metal formability limits are given.

In Chapter 2, firstly the main forming processes, deep drawing and stretch forming are described briefly. Then, the previous studies done for the prediction of sheet metal formability and FLD are summarized.

In Chapter 4, various theoretical instability models are presented. The contents and the principles of the theoretical models are given with the analytical formulations and the required assumptions for obtaining the major and minor limit strains.

In Chapter 5, a brief introduction of finite element method is given and the procedure of a finite element analysis is defined. In addition, the key facts of the FE analysis in PAM-Stamp are mentioned.

In Chapter 6, the simulative Nakazima tests using finite element method for obtaining the forming limits of sample materials are presented. Strain propagation phenomenon is used to obtain the limit strains. All of the process parameters with forming tools and specimen geometries are shown and the deformed states and necking zones are displayed for the determination of FLDs.

In Chapter 7, the comparisons of theoretical and simulative forming limit curves are done and the predicted forming limits of sample materials are discussed. Also, the effectiveness of the theoretical and the FE approaches are considered.

Finally, in Chapter 8, the conclusions of the whole work are given at the end of this thesis.

## CHAPTER 4

# INSTABILITY CRITERIA AND FORMING LIMIT DIAGRAM

Forming limit diagram (FLD), is a representation of the critical combination of the two principal surface strains major and minor above which localized necking instability is observed. Forming limit curve provides excellent guidelines for adjusting material; tooling and lubrication conditions. It is also strongly dependent on the material parameters.

Extensive studies have been conducted on the instability analysis and FLD prediction of the metallic sheets.

### **4.1 Maximum Load (ML) Instability**

This corresponds to the state of stress and strain when the net load across any section reaches a maximum in time, taking into account the variation of the dimensions [15].

In stretch forming, consider a large element as shown in Figure 4.1(a) and (b).

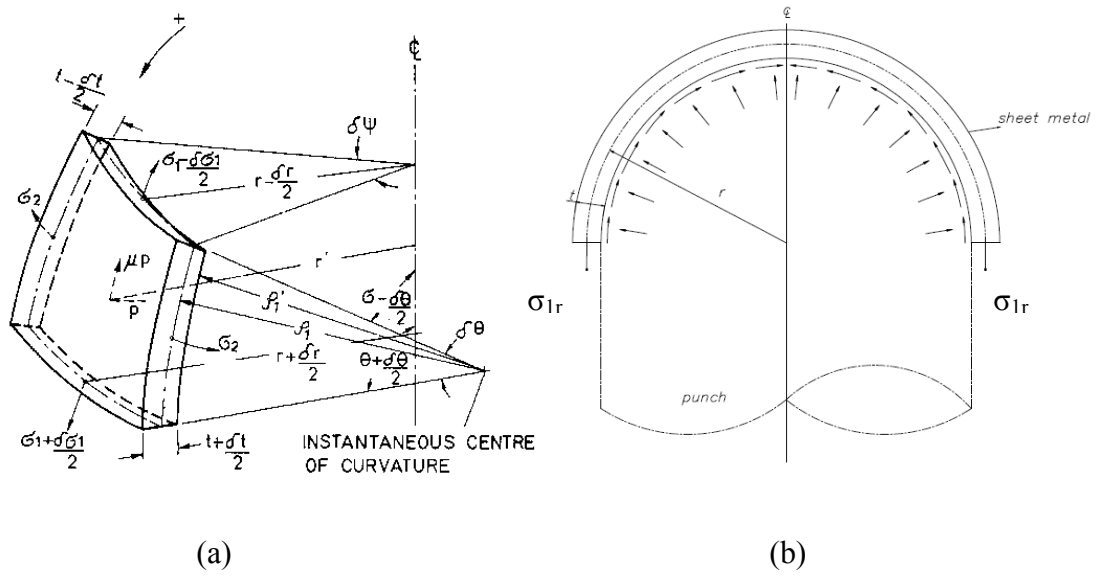


**Figure 4.1 Stretching Process, (a): stresses on element of shell wall [40], (b): hemispherical punch and sheet metal**

The load supported by any segment of angle  $\partial\psi$  in the direction of the tangent to its mean surface is:

$$Q = 2\pi\sigma_{1r}t \cdot \frac{\partial\psi}{2\pi} \quad (4.1)$$

To find the maximum load in time, the logarithms of both sides are taken and the resulting equation is differentiated:

Hence:

$$\frac{dQ}{Q} = \frac{dr}{r} + \frac{d\sigma_{1r}}{\sigma_{1r}} + \frac{dt}{t} = 0 \quad (4.2)$$

The constancy of volume:

$$d\varepsilon_{1r} + d\varepsilon_{2c} + d\varepsilon_3 = 0 \quad (4.3)$$

The principle strains in circumferential, thickness and radial directions can be written as:

$$\varepsilon_{2c} = \int_0^{\varepsilon_{2c}} d\varepsilon_{2c} = \int_{r_0}^r \frac{dr}{r} = \ln \frac{r}{r_0} \quad (4.4)$$

$$\varepsilon_3 = \int_0^{\varepsilon_3} d\varepsilon_3 = \int_{t_0}^t \frac{dt}{t} = \ln \frac{t}{t_0} \quad (4.5)$$

$$\varepsilon_{1r} = -(\varepsilon_{2c} + \varepsilon_3) \quad (4.6)$$

Substituting above equations into Eq. (4.2):

$$\frac{d\sigma_{1r}}{\sigma_{1r}} = d\varepsilon_{1r} \quad (4.7)$$

It can be shown that Eq. (4.7) applies to other triaxial, biaxial and uniaxial stress systems. It coincides with the Swift-Hill [6-7] criterion for proportional straining.

ML criteria can be applied to simple states of stress where the stress ratios remain constant, and the directions of the principal axes of stress remain fixed with respect to the element throughout the deformation.

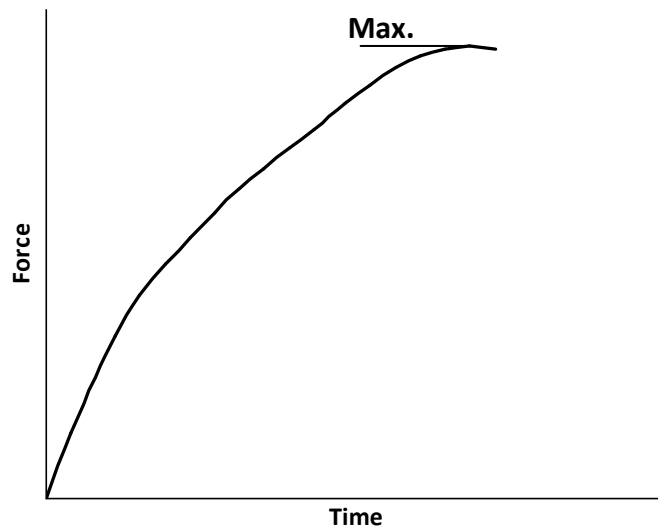


**Figure 4.2 Force vs. Time**

To obtain the limit strains using the maximum load condition, the force vs. time graph of the critical necked element in the FE solution is plotted and such a maximum of the curve is expected as in Figure 4.2. As a mathematical point of view, the maximum of the curve represents the point where the first derivative of the load equation equals to zero as given in Eq. (4.2).

The results of FE analysis are used to find the necessary unknowns for every stage of deformation in Eq. (4.1), which are  $r$ ,  $t$  and  $\sigma_r$ , to evaluate the load on the corresponding element. The radius is calculated as the mean value of the radius of the nodes of the element. Also, the thickness and radial stress values can directly be obtained for the corresponding element. Then, element load is calculated from Eq. (4.1) and the time at the maximum load point is recorded. Finally, the limit strains are obtained by recording the major and minor strains of the critical element at the instant of reaching to maximum load condition.

## 4.2 Strain Propagation Instability

According to Kaftanoğlu [15], at a point in a plastically deforming body, the state of strain and stress depends also on those at the neighboring points through the governing equations. If the material remains stable and does not fracture at such points, an increase in strains of one of the points will cause increases in the strains of the others, no matter how small or large they may be. However, there will be a limiting set of strains for each point which is generally different for each, beyond which a further increase in strains of one will cause no increase in the strains of the others. Effectively the strain propagation will cease, and at one point the rate of strain development will tend to infinity and it will soon fracture there (Figure 4.3).

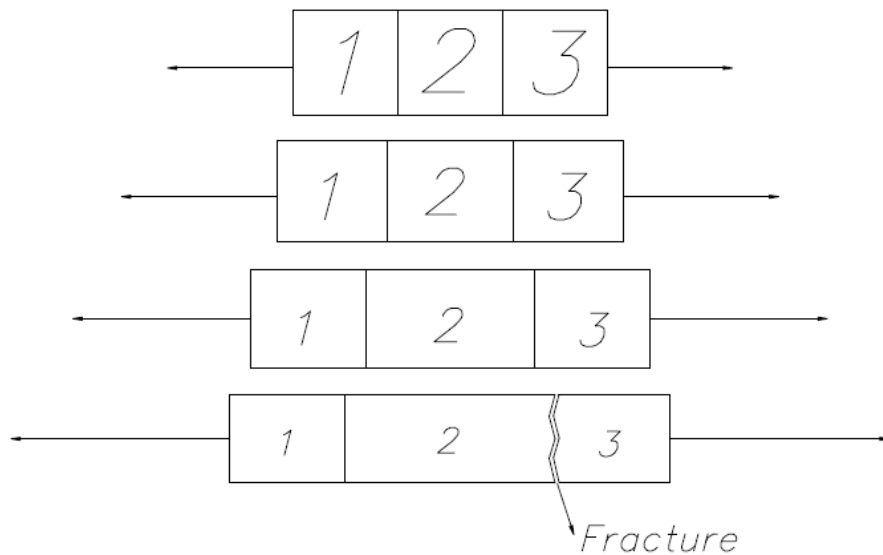


**Figure 4.3 Strain Propagation**

Strain propagation instability can in general happen anywhere along the bulge in stretch forming with a rigid punch, and is affected by friction and previous strain history. As shown in Figure 4.4, the equivalent strain increments of the elements no.2 and no.3 as seen in Figure 4.3 increases gradually up to a point; but after a point the strain increment of the necking element (element no.2) is still positive and continues growing while the equivalent strain increment of the neighboring element (element

no.3) decreases suddenly to zero. That means at zero point; no more strain transfer can be achieved due to the occurrence of fracture between elements.

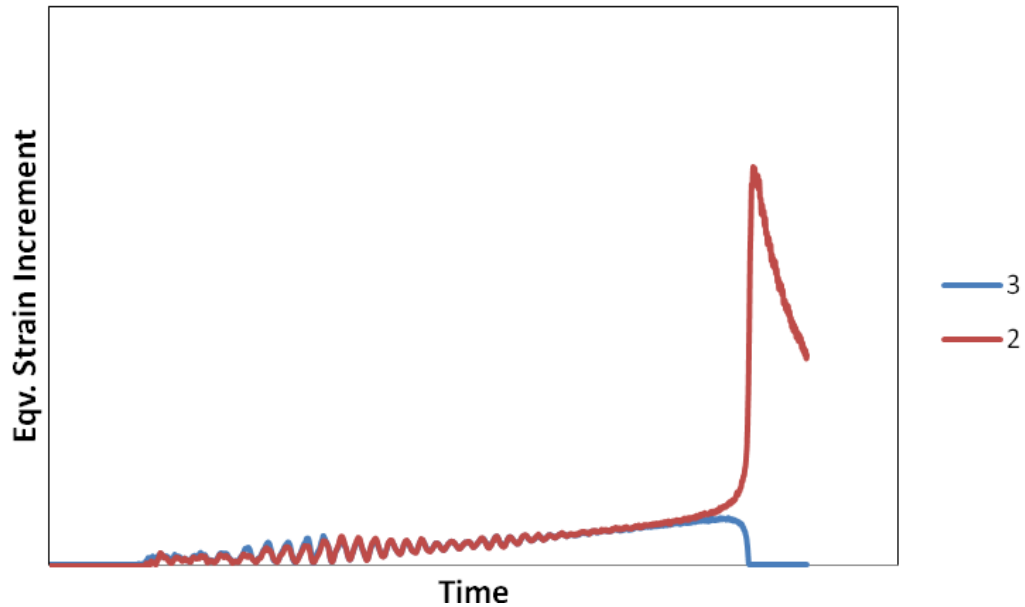


**Figure 4.4 Equivalent Strain Increment vs. Time**

It is not possible to express this criterion in simple mathematical formulae. Therefore, elemental strain histories are traced from the FE simulation and the limiting strains are predicted.

### **4.3 Swift Model**

Swift [6] developed a condition for the instability of plastic strain in the range of positive incremental strain ratios. Plastic instability takes the form of diffuse necking. He studied the diffuse necking based on the concept that instability occurs when, under certain loading condition, the increment of effective stress due to work hardening is less than the increment of the induced effective stress. Diffuse necking is accompanied by dramatic reduction of the corresponding cross-section area and drop in the load.

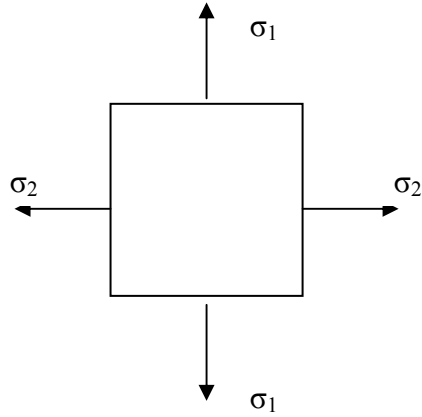


**Figure 4.5 Biaxial Stretching**

The beginning of necking corresponds to the maximum of the traction force. From the mathematical point of view, this condition can be written in the form:

$$dF = 0 \quad (4.8)$$

For deformations with a constant relationship between the principal axes of straining, the general expression of the Swift diffuse necking condition is [6]:

$$\frac{\sigma_1 \left( \frac{\partial f}{\partial \sigma_1} \right)^2 + \sigma_2 \left( \frac{\partial f}{\partial \sigma_2} \right)^2}{\frac{\partial f}{\partial \sigma_e} \left( \sigma_1 \frac{\partial f}{\partial \sigma_1} + \sigma_2 \frac{\partial f}{\partial \sigma_2} \right)} = \frac{d\sigma_e}{\sigma_e d\varepsilon_e} \quad (4.9)$$

Eq. (4.9) can be written as:

$$\frac{d\sigma_e}{\sigma_e} = \frac{d\varepsilon_e}{Z_d} \quad (4.10)$$

Then, the following relation can be written for  $Z_d$  as:

$$\frac{1}{Z_d} = \frac{\sigma_1 \left(\frac{\partial f}{\partial \sigma_1}\right)^2 + \sigma_2 \left(\frac{\partial f}{\partial \sigma_2}\right)^2}{\frac{\partial f}{\partial \sigma_e} \left( \sigma_1 \frac{\partial f}{\partial \sigma_1} + \sigma_2 \frac{\partial f}{\partial \sigma_2} \right)} \quad (4.11)$$

Assuming a Ludwik-Hollomon strain hardening law:

$$\sigma_e = K \varepsilon_e^n \quad (4.12)$$

Then Eq. (4.10) becomes:

$$\frac{d\sigma_e}{\sigma_e} = \frac{Kn \varepsilon_e^{n-1} d\varepsilon_e}{K \varepsilon_e^n} = \frac{d\varepsilon_e}{Z_d} \quad (4.13)$$

The expression for the equivalent limit strain is obtained as:

$$\varepsilon_e^* = n Z_d \quad (4.14)$$

or:

$$\varepsilon_e^* = \frac{\frac{\partial f}{\partial \sigma_e} \left( \sigma_1 \frac{\partial f}{\partial \sigma_1} + \sigma_2 \frac{\partial f}{\partial \sigma_2} \right)}{\sigma_1 \left(\frac{\partial f}{\partial \sigma_1}\right)^2 + \sigma_2 \left(\frac{\partial f}{\partial \sigma_2}\right)^2} n \quad (4.15)$$

For total strains, the Levy-Mises equations are written:

$$\frac{\varepsilon_1}{\left(\frac{\partial f}{\partial \sigma_1}\right)} = \frac{\varepsilon_2}{\left(\frac{\partial f}{\partial \sigma_2}\right)} = \frac{\varepsilon_e}{\left(\frac{\partial f}{\partial \sigma_e}\right)} \quad (4.16)$$

Hence, according to Considere's [31] criterion, a material obeying the Ludwik-Hollomon law starts to neck when the strain is equal to the strain hardening coefficient.

Swift analyzed a sheet element loaded along two perpendicular directions and applied the Considere criterion for each direction. Assuming a strain hardening law described by Eq. (4.12), he obtained the following expressions for limit strains:

$$\varepsilon_1^* = \frac{\sigma_1 \left(\frac{\partial f}{\partial \sigma_1}\right)^2 + \sigma_2 \left(\frac{\partial f}{\partial \sigma_2}\right) \left(\frac{\partial f}{\partial \sigma_1}\right)}{\sigma_1 \left(\frac{\partial f}{\partial \sigma_1}\right)^2 + \sigma_2 \left(\frac{\partial f}{\partial \sigma_2}\right)^2} n \quad (4.17)$$

$$\varepsilon_2^* = \frac{\sigma_2 \left(\frac{\partial f}{\partial \sigma_1}\right)^2 + \sigma_1 \left(\frac{\partial f}{\partial \sigma_1}\right) \left(\frac{\partial f}{\partial \sigma_2}\right)}{\sigma_1 \left(\frac{\partial f}{\partial \sigma_1}\right)^2 + \sigma_2 \left(\frac{\partial f}{\partial \sigma_2}\right)^2} n \quad (4.18)$$

where  $f$  is the yield function.

By using different yield functions, it is possible to evaluate the limit strains as functions of the loading ratio  $\alpha$  and the mathematical parameters of the material ( $n, R_0, R_{45}, R_{90}, M$ ). In the derivations, rigid plasticity, volume constancy and constant strain ratio are assumed.

As an example, the generalized form of the Hill's yield criterion is given in Eq. (A.1). If the Hill 1948 yield criterion is written as dependent of the principle stresses, the following relation is obtained:

$$\sigma_1^2 - \frac{2R_0}{1+R_0} \sigma_1 \sigma_2 + \frac{R_0(1+R_{90})}{R_{90}(1+R_0)} \sigma_2^2 = \sigma_0^2 \quad (4.19)$$

Then, for the Eqs. (4.17) and (4.18) the derivatives are written as;

$$\frac{\partial f}{\partial \sigma_1} = \left( 2 - \frac{2R_0}{1+R_0} \alpha \right) \sigma_1 \quad (4.20)$$

$$\frac{\partial f}{\partial \sigma_2} = \left( 2\alpha \frac{R_0(1+R_{90})}{R_{90}(1+R_0)} - \frac{2R_0}{1+R_0} \right) \sigma_1 \quad (4.21)$$

When the above derivatives are substituted in Eqs. (4.17) and (4.18), limit strains are obtained.

As an example, if the Hill 1948 criterion is used, the limit strains are as follows:

$$\varepsilon_1^* = \frac{(1+R_0 - R_0\alpha) \left( 1+R_0 + \alpha^2 \left( \frac{R_0}{R_{90}} \right) (1+R_{90}) - 2\alpha R_0 \right)}{(1+R_0 - R_0\alpha)^2 + \alpha \left[ \alpha \frac{R_0(1+R_{90})}{R_{90}} - R_0 \right]^2} \cdot n \quad (4.22)$$

$$\varepsilon_2^* = \frac{(1+R_0 - R_0\alpha) \left( \alpha + \alpha R_0 + \alpha^2 R_0 + \alpha \left( \frac{R_0}{R_{90}} \right) (1+R_{90}) - R_0 \right)}{(1+R_0 - R_0\alpha)^2 + \alpha \left[ \alpha \frac{R_0(1+R_{90})}{R_{90}} - R_0 \right]^2} \cdot n \quad (4.23)$$

By computing the values of  $\varepsilon_1$  and  $\varepsilon_2$  for various loading ratios  $\alpha$  and plotting them in a rectangular coordinate system  $\varepsilon_1^*, \varepsilon_2^*$ , the necking limit curve is obtained.

#### 4.4 Hill Model

Hill [7] discussed the localized necking in thin sheet by considering the discontinuity of stress and strain, and laid the foundation of localized instability analysis. His theory is based on the characteristics of governing equations in plane stress. Localized necking is possible only when the equations are hyperbolic, when the characteristic directions are those of zero extension. Therefore, local instability is

possible only when the incremental strain ratio is negative, i.e. corresponding to the strain state in the left hand side of FLD. Depending on the material and the type of loading, this type of instability can occur before or after the maximum load point. The change in cross-section dimensions associated with localized necking is negligible.

In the case of uniaxial tension, the localized necking develops along a direction, which is inclined with respect to the loading direction. Hill assumed that the necking direction is coincident with the direction of zero-elongation and thus the straining in the necking region is due only to the sheet thinning.

Hill's general expression for localized necking condition is given as [7]:

$$\frac{\left[ \frac{\partial f}{\partial \sigma_1} + \frac{\partial f}{\partial \sigma_2} \right]}{\frac{\partial f}{\partial \sigma_e}} = \frac{d\sigma_e}{\sigma_e d\varepsilon_e} \quad (4.24)$$

The governing equations to obtain the limit strains are the same as Eqs. (4.10-4.14). Now,  $Z_d$  is replaced with  $Z_L$  where diffuse and localized necking conditions are represented, respectively.

Next, equivalent limit strain is written as follows:

$$\varepsilon_e^* = \frac{\frac{\partial f}{\partial \sigma_e}}{\frac{\partial f}{\partial \sigma_1} + \frac{\partial f}{\partial \sigma_2}} n \quad (4.25)$$

Finally, the expressions of the limit strains for localized necking are obtained as follows:

$$\varepsilon_1^* = \frac{\frac{\partial f}{\partial \sigma_1}}{\frac{\partial f}{\partial \sigma_1} + \frac{\partial f}{\partial \sigma_2}} n \quad (4.26)$$

$$\varepsilon_2^* = \frac{\frac{\partial f}{\partial \sigma_2}}{\frac{\partial f}{\partial \sigma_1} + \frac{\partial f}{\partial \sigma_2}} n \quad (4.27)$$

It can be seen that:

$$\varepsilon_1^* + \varepsilon_2^* = n \quad (4.28)$$

Again, the previously defined derivatives in Eqs. (4.20) and (4.21) are substituted in Eqs. (4.26) and (4.27) and the limit strains for the LHS of the FLD can be obtained for various stress ratios.

#### 4.5 Storen and Rice Instability Model

Storen and Rice [8] also treat the plastic instability condition that localized necking takes place in initially uniform and homogeneous sheet. They predicted the localized necking over the entire range of FLD by incorporating the J2 deformation theory of plasticity into the classical bifurcation analysis, which is proposed by Hill. They used a simplified constitutive model of a pointed vertex on subsequent yield loci such that the equations of deformation theory apply for fully-active stress increments. Localized necking can be observed experimentally in biaxial stretched sheets. Their result supports the hypothesis of vertex formation on the yield locus under continued plastic flow. They indicate that with flow theories which use smooth yield loci localized necking is impossible under biaxial stretching of homogeneous sheet.

Chow and Ji [10] developed a more simplified and a generalization of a vertex theory proposed by Storen and Rice [8]. They obtained the condition for localized necking

and forming limit strains by applying Hill's quadric and Hosford's higher order yield criteria as follows:

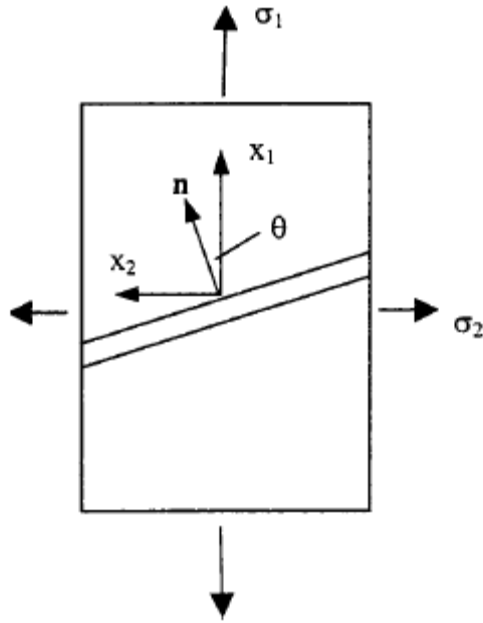


**Figure 4.6 Localized Necking Band**

Consider a sheet metal deforms biaxially as in Figure 4.6 such that at the localized band:

$$n_1 = \cos \theta \quad , \quad n_2 = \sin \theta \quad (4.29)$$

where  $\theta$  is the angle between the  $x_1$  axis and the normal.

There is a velocity discontinuity between the inside and outside of the band as:

$$\Delta v_i = v_{i,inside} - v_{i,outside} = f_i(\mathbf{n} \cdot \mathbf{x}) = f_i(n_k \cdot x_k) \quad (i, k = 1, 2) \quad (4.30)$$

The difference in rate of deformation thus,

$$\Delta(\partial v_i / \partial x_j) = \frac{\partial(\Delta v_i)}{\partial x_j} = f'_i(n_k x_k) n_j = g_i n_j \quad (4.31)$$

$$g_i = f'_i(n_k x_k) \quad (i, j, k = 1, 2) \quad (4.32)$$

Across the localized band, the equilibrium equations for the principal stress coordinate system can be written as:

$$\begin{aligned} n_1 \Delta \dot{\sigma}_{11} + n_2 \Delta \dot{\sigma}_{12} - n_1 \sigma_{11} (g_1 n_1 + g_2 n_2) &= 0 \\ n_1 \Delta \dot{\sigma}_{12} + n_2 \Delta \dot{\sigma}_{22} - n_1 \sigma_{22} (g_1 n_1 + g_2 n_2) &= 0 \end{aligned} \quad (4.33)$$

where  $\sigma_{ij}$  ( $i, j = 1, 2$ ) are components of stress tensor;  $\Delta \dot{\sigma}_{ij}$  the discontinuity of the stress tensor across the localized band.

Across the localized band, the shear stress rate is proved to be continuous by applying the moment equilibrium [9]:

$$\Delta \dot{\sigma}_{12} = 0 \quad (4.34)$$

For the left hand side (LHS) of the FLD, the equilibrium equations for the principle stress coordinates can be simplified as:

$$\begin{aligned} \Delta \dot{\sigma}_1 - \sigma_1 (g_1 n_1 + g_2 n_2) &= 0 \\ \Delta \dot{\sigma}_2 - \sigma_2 (g_1 n_1 + g_2 n_2) &= 0 \end{aligned} \quad (4.35)$$

Next, for the right hand side (RHS), the assumption is made that the direction of the localized band is perpendicular to the major strain, ( $\theta = 0$ ).

$$n_1 = 1, \quad n_2 = 0 \quad (4.36)$$

Then Eq. (4.35) becomes:

$$\Delta \dot{\sigma}_1 - \sigma_1 g_1 = 0 \quad (4.37)$$

Now let's define the governing equations of the general deformation theory of plasticity in order to evaluate the limit strains.

Assuming plane stress condition, for plastically orthotropic materials, the equivalent stress can be written in a generalized form [32] as:

$$\sigma_e = \frac{1}{[R_{90}(1+R_0)]^{1/a}} \left( R_{90} |\sigma_1|^a + R_0 |\sigma_2|^a + R_0 R_{90} |\sigma_1 - \sigma_2|^a \right)^{1/a} \quad (4.38)$$

Where  $\sigma_1$  and  $\sigma_2$  are principle stresses,  $R_0$  and  $R_{90}$  are the strain ratio under rolling and transverse direction and  $a$  is constant.

According to the plastic flow rule, the principal strain increments are:

$$d\varepsilon_1^p = d\lambda \frac{\partial \sigma_e}{\partial \sigma_1} = ad\lambda \cdot \frac{\left( \text{sgn}(\sigma_1) |\sigma_1|^{a-1} + R_0 \text{sgn}(\sigma_1 - \sigma_2) |\sigma_1 - \sigma_2|^{a-1} \right)}{(1+R_0) \sigma_e^{a-1}} \quad (4.39)$$

$$d\varepsilon_2^p = d\lambda \frac{\partial \sigma_e}{\partial \sigma_2} = ad\lambda \cdot \frac{R_0 \left( \text{sgn}(\sigma_2) |\sigma_2|^{a-1} - R_{90} \text{sgn}(\sigma_1 - \sigma_2) |\sigma_1 - \sigma_2|^{a-1} \right)}{R_{90} (1+R_0) \sigma_e^{a-1}} \quad (4.40)$$

The strain energy principle:

$$\sigma_1 d\varepsilon_1 + \sigma_2 d\varepsilon_2 = \sigma_e d\varepsilon_e \quad (4.41)$$

Now, substitute Eqs. (4.38), (4.39), (4.40) into Eq. (4.41):

$$d\lambda = \frac{d\varepsilon_e}{a} \quad \text{or} \quad \lambda = \frac{\varepsilon_e}{a} \quad (4.42)$$

Then,

$$\frac{\sigma_e}{\sigma_1} = \frac{\text{sgn}(\sigma_1)}{[R_{90}(1+R_0)]^{1/a}} \left[ R_{90} + R_0 |\alpha|^a + R_0 R_{90} |1-\alpha|^a \right]^{1/a} = f(\alpha) \quad (4.43)$$

where  $\alpha = \frac{\sigma_2}{\sigma_1}$  is the constant stress ratio under proportional loading.

Now, integrating Eqs.(4.39), (4.40) with Eq.(4.42), the generalized deformation theory of plasticity is obtained as:

$$\varepsilon_1 = \varepsilon_e \cdot \frac{(\text{sgn}(\sigma_1) |\sigma_1|^{a-1} + R_0 \text{sgn}(\sigma_1 - \sigma_2) |\sigma_1 - \sigma_2|^{a-1})}{(1+R_0) \sigma_e^{a-1}} \quad (4.44)$$

$$\varepsilon_2 = \varepsilon_e \cdot \frac{R_0 (\text{sgn}(\sigma_2) |\sigma_2|^{a-1} - R_{90} \text{sgn}(\sigma_1 - \sigma_2) |\sigma_1 - \sigma_2|^{a-1})}{R_{90} (1+R_0) \sigma_e^{a-1}} \quad (4.45)$$

where  $\varepsilon_1$  and  $\varepsilon_2$  are the major and minor strains, respectively.

For sheet metal forming operations  $\sigma_1 \geq 0$ ,  $\sigma_2 \geq 0$  and  $\sigma_1 - \sigma_2 \geq 0$ . Now differentiating Eqs.(4.44) and (4.45) becomes:

$$(1+R_0) \sigma_e^a \dot{\varepsilon}_1 = [\sigma_e - (a-1)h\varepsilon_e] [\sigma_1^{a-1} + R_0 (\sigma_1 - \sigma_2)^{a-1}] \dot{\varepsilon}_e + (a-1) \sigma_e \varepsilon_e \left\{ (\sigma_1^{a-2} + R_0 (\sigma_1 - \sigma_2)^{a-2}) \dot{\sigma}_1 - R_0 (\sigma_1 - \sigma_2)^{a-2} \dot{\sigma}_2 \right\} \quad (4.46)$$

$$\frac{R_{90}(1+R_0)}{R_0} \sigma_e^a \dot{\varepsilon}_2 = [\sigma_e - (a-1)h\varepsilon_e] [\sigma_2^{a-1} + R_{90} (\sigma_1 - \sigma_2)^{a-1}] \dot{\varepsilon}_e + (a-1) \sigma_e \varepsilon_e \left\{ (\sigma_2^{a-2} + R_{90} (\sigma_1 - \sigma_2)^{a-2}) \dot{\sigma}_2 - R_{90} (\sigma_1 - \sigma_2)^{a-2} \dot{\sigma}_1 \right\} \quad (4.47)$$

where  $h = \partial \sigma_e / \partial \varepsilon_e$  is the tangential modulus.

From the above relation one can obtain:

$$\dot{\sigma}_1 = \frac{1}{(a-1)\sigma_e \varepsilon_e} \times \quad (4.48)$$

$$\left\{ \frac{[\sigma_2^{a-2} + R_{90}(\sigma_1 - \sigma_2)^{a-2}] \dot{\varepsilon}_1 + R_{90}(\sigma_1 - \sigma_2)^{a-2} \dot{\varepsilon}_2}{\sigma_1^{a-2} - \sigma_2^{a-2} + (R_{90}\sigma_1^{a-2} + R_0\sigma_2^{a-2})(\sigma_1 - \sigma_2)^{a-2}} (1 + R_0)\sigma_e^a - [\sigma_e - (a-1)h\varepsilon_e] \sigma_1 \dot{\varepsilon}_e \right\}$$

From Eqs. (4.31) and (4.32), the discontinuity of strain rate across the band can be deduced both for the LHS and RHS of the FLD. As previously mentioned, the localized band at RHS is normal to the major strain and therefore  $\Delta \dot{\varepsilon}_2 = 0$ .

$$\Delta \dot{\varepsilon}_1 = g_1 n_1 \quad \text{and} \quad \Delta \dot{\varepsilon}_2 = g_2 n_2 = \rho g_1 n_1 \quad \text{at LHS} \quad (4.49a,b)$$

where  $\rho = \frac{\varepsilon_2}{\varepsilon_1}$ .

Remember that, to satisfy the equilibrium and consistency equations across the localized band the stress and strain are continuous but the stress and strain rates are discontinuous.

Then, integrate Eq. (4.41) with Eq. (4.43):

$$\varepsilon_{eq} = (1 + \alpha\rho) \frac{\sigma_1 \varepsilon_1}{\sigma_e} = (1 + \alpha\rho) \frac{\varepsilon_1}{f(\alpha)} \quad (4.50)$$

Under proportional loading:

$$\rho = \frac{d\varepsilon_2}{d\varepsilon_1} = \frac{R_0}{R_{90}} \cdot \frac{\alpha^{a-1} - R_{90}(1-\alpha)^{a-1}}{1 + R_0(1-\alpha)^{a-1}} \quad (4.51)$$

Now, substitute Eqs. (4.35), (4.36), (4.49a, b) and (4.50) into Eq. (4.48), the tangent modulus at the LHS of FLD is obtained:

$$h = \frac{\sigma_e}{(a-1)\varepsilon_e} \left( 1 - \frac{1}{1+\alpha\rho} \times \left\{ \frac{(1+R_0)[\alpha^{a-2} + R_{90}(1+\rho)(1-\alpha)^{a-2}]f^a(\alpha)}{\alpha^{a-2} + (R_{90} + R_0\alpha^{a-2})(1-\alpha)^{a-2}} \right. \right. \\ \left. \left. - (a-1)(1+\rho)\varepsilon_e f(\alpha) \right\} \right) \quad (4.52)$$

At the RHS of FLD:

$$h = \frac{\sigma_e}{(a-1)\varepsilon_e} \left( 1 - \left\{ \frac{(1+R_0)[\alpha^{a-2} + R_{90}(1-\alpha)^{a-2}]f^a(\alpha)}{\alpha^{a-2} + (R_{90} + R_0\alpha^{a-2})(1-\alpha)^{a-2}} - (a-1)\varepsilon_e f(\alpha) \right\} \right) \quad (4.53)$$

Using power law as hardening equation:

$$\sigma_e = K\varepsilon_e^n \quad (4.54)$$

Then,

$$h = Kn\varepsilon_e^{n-1} \quad (4.55)$$

Finally, substituting Eq. (4.55) into Eqs. (4.52) and (4.53), the limit strains at the LHS and RHS are derived.

At the LHS (negative strain ratio region):

$$\varepsilon_1^* = \frac{(1+R_0)(\alpha^{a-2} + R_{90}(1+\rho)(1-\alpha)^{a-2})f^a(\alpha)}{(a-1)(1+\rho)(1+\alpha\rho)(\alpha^{a-2} + (R_{90} + R_0\alpha^{a-2})(1-\alpha)^{a-2})} + \frac{(a-1)n-1}{(a-1)(1+\rho)} \quad (4.56)$$

At the RHS (positive strain ratio region):

$$\varepsilon_1^* = \frac{(1 + R_0)(\alpha^{a-2} + R_{90}(1 - \alpha)^{a-2})f^a(\alpha)}{(a - 1)(1 + \alpha\rho)(\alpha^{a-2} + (R_{90} + R_0\alpha^{a-2})(1 - \alpha)^{a-2})} + \frac{(a - 1)n - 1}{(a - 1)(1 + \alpha\rho)} \quad (4.57)$$

#### 4.6 Keeler and Goodwin Model

The maximum values of the principal strains  $\varepsilon_1$  and  $\varepsilon_2$  can be determined by measuring the strains at fracture on sheet components covered with grids of circles. The research in this field is pioneered by Keeler [33], based on the observations of Geasamer [34] that instead of using global indices the local deformations have to be considered. During forming the initial circles of the grid become ellipses. Keeler plotted the maximum principal strain against the minimum principal strain obtained from such ellipses at fracture of parts after biaxial stretching ( $\varepsilon_1 > 0$ ;  $\varepsilon_2 > 0$ ). This way he obtained a curve limiting the tolerable range. (Figure 4.7)

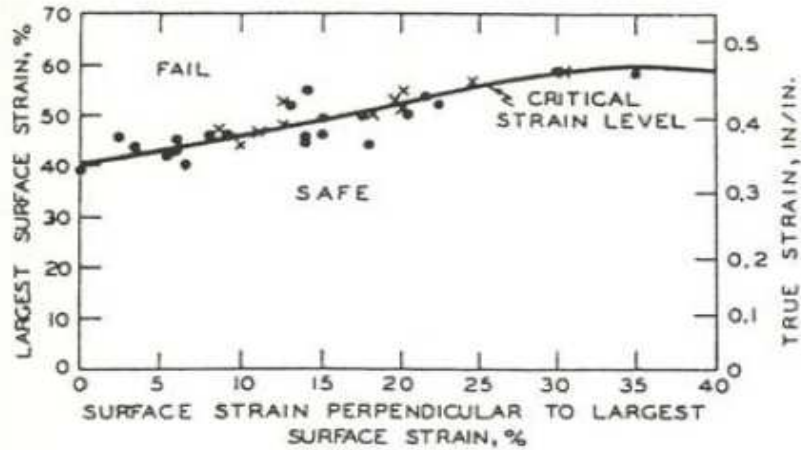
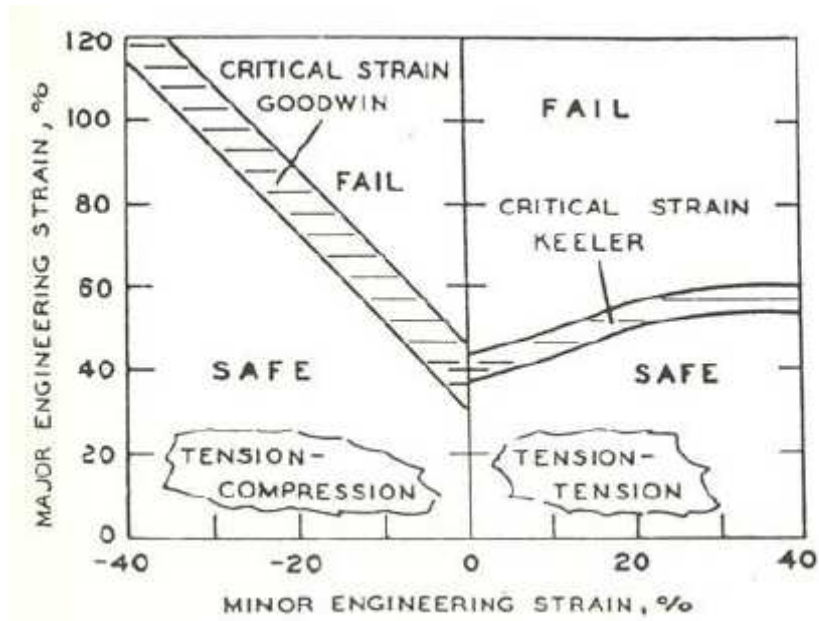


Figure 4.7 FLD Defined by Keeler [33]

Later, Goodwin [16] plotted the curve for the tension/compression domain ( $\varepsilon_1 > 0$ ;  $\varepsilon_2 < 0$ ) by using different mechanical tests. In this case, transverse compression allows for obtaining high values of tensile strains like in rolling or wire drawing. The

diagrams of Keeler and Goodwin together give the values of  $\varepsilon_1$  and  $\varepsilon_2$  at fracture. This is currently called the forming limit diagram (FLD).



**Figure 4.8 FLD Defined by Keeler and Goodwin [16]**

Later, Keeler and Brazier [35] proposed an empirical relationship for calculating the limit strains corresponding to plane strain:

$$\varepsilon_{10}(\%) = (23.3 + 14.13 \cdot t) \frac{n}{0.21} \quad (4.68)$$

where  $t$  is the sheet thickness in millimeters.  $\varepsilon_{10}$  is the engineering strain and  $n$  is the strain hardening coefficient.

According to this model, the FLD is composed of two lines through the point  $\varepsilon_{10}$  in the plain-strain state. The slopes of the lines located respectively on the left and right hand side of the FLD is  $45^\circ$  and  $20^\circ$ .

The above relation is also introduced by the North American Deep Drawing Research Group (NADDRG) [36] to predict the FLD more easily in the press workshop by simplifying the experimental and theoretical determination.

## **CHAPTER 5**

### **FINITE ELEMENT METHOD**

#### **5.1 Review of Finite Element Analysis**

The development of the finite element method as an analysis tool essentially began with the invention of the digital computers. In order to obtain a numerical solution for a structural or continuum problem, it is necessary to construct and solve algebraic equations that govern the response of the system. Digital computers enabled us to use finite element method effectively in establishing and solving the equations of the complex engineering problems.

First, FEM was developed on a physical basis for the analysis of the problems in structural mechanics; later it became a very effective tool in the solution of many other classes of problems. Since then, research and development on this field continued very fast and today high number of publications and extensive studies are available in literature.

In FEM, the body is discretized by a finite number of simple shape regions of finite size. Each of these simple regions is called a “finite element”. The finite elements are connected to each other at finite number of points. Each connection points are called a “node”.

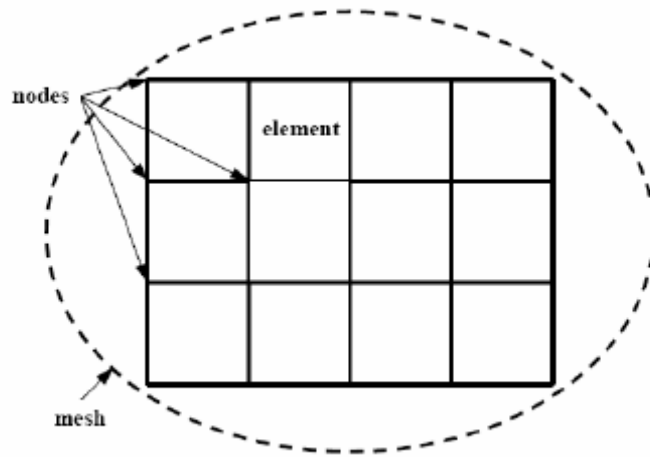


**Figure 5.1 Finite Element**

In FE, the most important formulation, which is widely used for the solution of practical problems, is the displacement based finite element method. Today all general purpose analysis codes have been developed using this formulation due to its generality, simplicity and good numerical properties.

Today, there are a lot of commercial and non-commercial FEM codes which are used for implementation of FEM. In this project, Pam-Stamp 2G is used as the commercial FEM package due to its effectiveness in stretching and drawing operations.

The basic steps for a FE analysis can be listed as pre-processing, solution and post-processing. These steps can be briefly described as follows:

### **5.1.1 Pre-processing**

In pre-processing step the following parameters are defined:

- The geometry of the problem.
- The finite element type to be used.
- The material properties of the elements.

- The element connectivities (meshing).
- The physical constraints (boundary conditions).
- The loadings (force, pressure...).

### **5.1.2 Solution**

In the solution step, the governing finite element algebraic equations are assembled in matrix form and the unknown variables are computed. Then, the computed variables are substituted into the equations to obtain the reaction forces, elemental stresses and etc...

### **5.1.3 Post-processing**

The post-processing step includes the analysis and evaluation of the results of the solution step. Sorting, printing and plotting of the selected results of the FE solution are achieved. By using an appropriate FE software, the elemental stresses-strains, the deformed shape of the model and the animation of the process can be evaluated at this step and finally the engineering judgment of the solution is done whether the results are reasonable or not.

## **5.2 Modeling of Stretch Forming for Pam-Stamp**

### **5.2.1 Mesh Generation**

For a FE simulation, the analysis process starts with the modeling of the required tools, then meshing them appropriately.

In general, to create geometries of the tools, a 3D modeling software like Pro-Engineer, Ideas, Catia, Solidworks etc. is used. After constructing the models of each tool in the 3-D software, each model is saved with an appropriate file format as IGES, VDA, STL etc. which the FEA software can read. Some FE software's are not very efficient and user-friendly in the pre-processing or post-processing phases.

Therefore, instead of trying to use only one FE software to achieve pre-processing, solution and post-processing stages, different software's can be used to progress faster and more efficient. Today, several software's are available that are specialized for only pre-processing, solving and post-processing stages. After, deciding which software to use, the models are opened and meshed in the FE software as previously mentioned in section 5.1. Then, the analysis is done.

In this study, the geometries of the tools and blank are modeled in a well known commercial FE code MSC. Marc. In Marc, the geometries of the tools are drawn in 2-D then converted to 3-D by rotation and symmetry modules. After constructing the surfaces, meshing is done. For blank, the geometry is prepared in 2-D and 2-D planar meshing is used. 4 node quadrilateral elements are selected for meshing the tools and blanks. After completing with meshing, they are saved as BDF file format. To import the meshed surfaces into Pam-Stamp, .NAS file format is required [37-38]. Therefore, previously saved BDF file format is changed with the Nastran format .NAS. Now, the meshes of the required tools (punch, die, blank holder) and blank are ready to be imported in Pam-Stamp.

### **5.2.2 Analysis in Pam-Stamp**

In Pam-Stamp, the meshes are imported first and the positions of the tools are adjusted for the stamping process. The distance between the punch, blank holder and die with respect to the blank are half of the thickness of the blank in the vertical direction such that the blank holder and the punch are located above the blank whereas die is placed below the blank as shown in Figure 5.2.

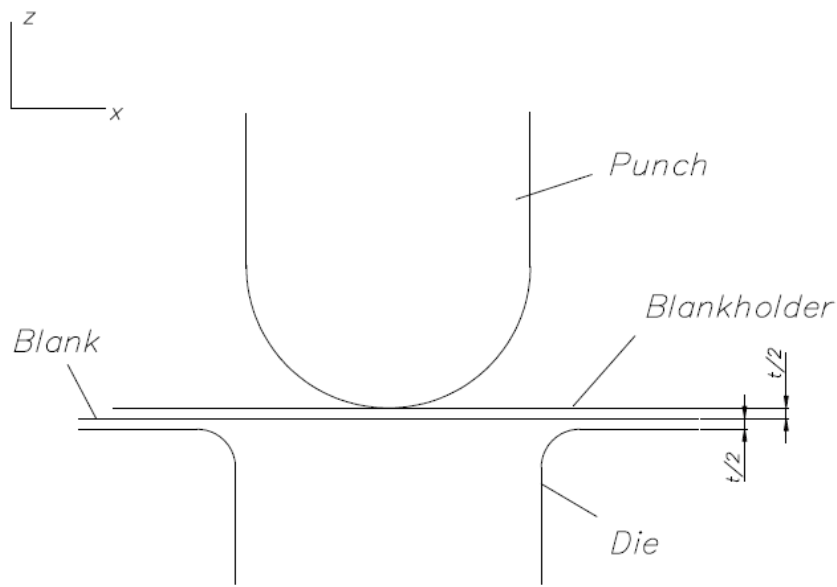


**Figure 5.2 Initial Tool Positions**

After importing and placing the meshes, the initial and boundary conditions of the tools, the process parameters are defined. First, the blank is defined as the deformable body where as the other tools are rigid bodies. Then the material is assigned to the blank. Pam-Stamp has various materials in its database. However, new user-defined materials can be added to the database. In current study, the new material properties are defined. Then, the other process parameters, such as coefficient of friction, punch velocity, blank holder force are defined. Furthermore, mesh refinement option exists in the software. However, it is not used in the current analysis in order to trace the deformation of each element. Finally, the start-stop criteria and contents of the output file are determined and pre-processing stage is completed.

After finishing the analysis, post-processing modules of Pam-Stamp are used. For all elements and nodes, the stress, strain, position, velocity, energy values can be evaluated for each deformation step. Finally, critical and safe zones of the deformable tool are evaluated and the success of the process is discussed.

## CHAPTER 6

### PREDICTION OF FLD BY SIMULATIVE TESTS

#### 6.1 Nakazima Test

Nakazima test is one of the commonly used experimental techniques that is applied to obtain the FLD of sheet metal materials. The various major and minor strain pairs are collected to obtain a strain domain as wide as possible. To achieve different strain combinations, various test samples are stretched for varying widths.

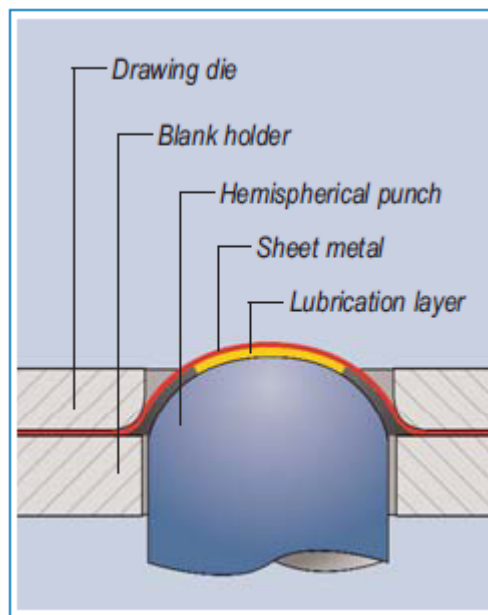


**Figure 6.1 Nakazima Test**

Nakazima test is achieved by drawing specimens using hemispherical punch and a circular die (Figure 6.1). To conduct the experiment, sheet metal testing machine is used as shown in Figure 6.2.



**Figure 6.2 Zwick-Roell Sheet Metal Testing Machine**

In general, before starting the test, circles and lines are drawn to the surface of undeformed blank to measure the strains after deformation. The shape of the circles become ellipses and the major and minor axes are used to measure the major and minor strains accordingly. Magnifying glasses, microscopes or flexible measuring strips are used as measuring tools. However, these techniques have some disadvantages such as high measuring times, low resolution and possibility of misreading the measured values.

Today's technology enables more precise and faster measuring tools for the determination of the strains. By using optical measurement system such as GOM/Aramis System as shown in Figure 6.3, the preparation of specimens, forming processes and the determination of deformations could be achieved very effectively.



**Figure 6.3 GOM Optical Measuring System**

In Nakazima test, 7 test samples are stretched from uniaxial tension to equibiaxial tension state. For each sample, the test is continued up to the occurrence of visible neck. At that state, the principle strains near the failure region are measured. From each sample, one data point (minor strain, major strain) for the FLD is obtained. After repeating the procedure for 7 samples, the full range of FLD is determined. The tested experimental test samples are shown in Figure 6.4.

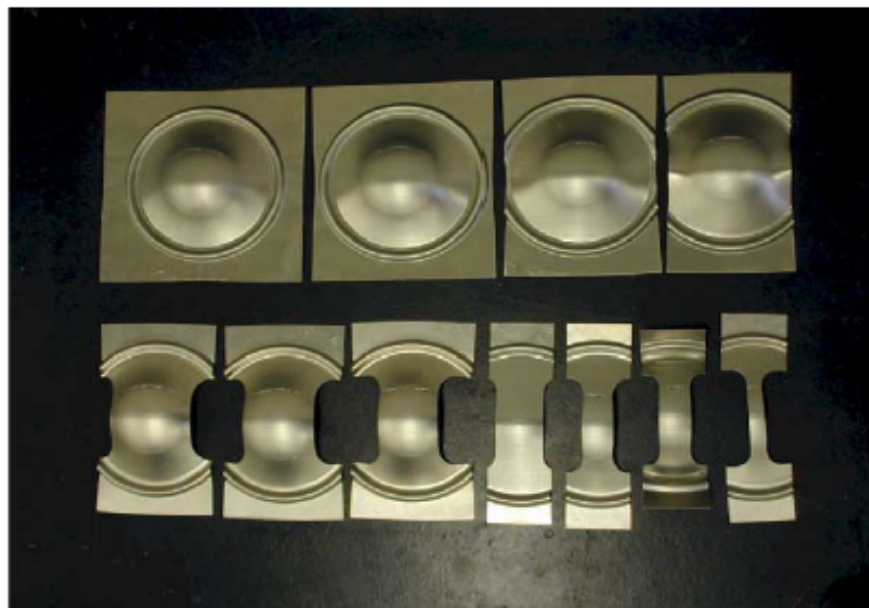


**Figure 6.4 Nakazima Test Samples**

This experimental technique is commonly preferred in industry to evaluate the forming limits of the materials due to its simple tools and test sample geometries. In addition, covering the entire range of FLD is the other important fact of the test. However, using finite element procedure to simulate the test could save a lot of time and be very powerful in practical use.

## 6.2 FE Simulations

It is a well known fact that strain localization can be captured in finite element simulations of sheet forming processes using shell elements. In this study we have been interested in finding out how the predicted limit strains in the FE models are related to the ones predicted in the various theoretical models previously discussed.

In this study, commercial dynamic-explicit FE code PAM-Stamp has been used. The geometries of the tools are shown in Figure 6.5.

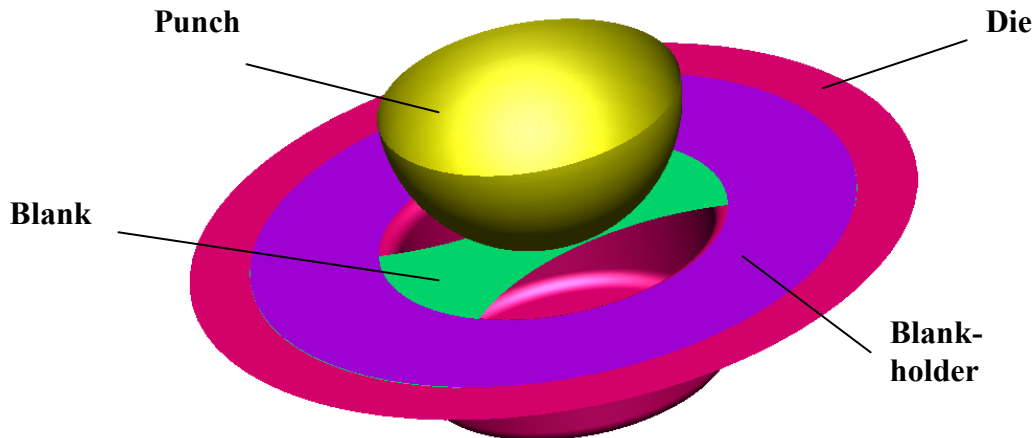


**Figure 6.5 Nakazima Tools**

In the present study, for all of the analysis including AA2024-O and SAE 1006, the geometries of punch, die and blank holder are the same. The parameters used for Nakazima test are according to the standard ISO-DIS 12004-2 [39]. In addition, the friction value is taken according to the studies of Kaftanoğlu [40]. The parameters of the Nakazima test are shown in Table 6.1.

**Table 6.1 Process Parameters**

Hemispherical punch radius:	50mm
Die profile radius:	5mm
Die inner radius:	105mm
Punch Speed:	4mm/s
Blank holder force:	100kN
Friction coefficient:	0.08
# of integration points:	9
Element type:	Belytschko-Tsay
Element size of blank:	2mm

For the finite element models, punch, die and blank holder are considered as the rigid tools whereas blank is the only deformable tool. In meshing the geometries, rectangular shell elements are used with an element size of 2mm. No mesh refinement is used in order to trace the elemental stresses and strains. In addition, 9 integration points through the thickness are used to ensure enough calculation precision.

### **6.2.1 Selection of Measuring Elements in FE Simulations**

In Nakazima test simulations that are shown in the following sections, strain propagation criterion by Kaftanoğlu [15] is utilized to obtain the limit strains of the specimens. The measuring elements are selected as follows:

- (a) The neighboring elements of the necking region are chosen arbitrarily as the measuring elements.
- (b) The equivalent strain increments of the neighboring measuring elements should become zero after the occurrence of localized necking state while the equivalent strain increments of the necked elements are positive.

## 6.2.2 Analysis of SAE 1006

The thickness of the SAE 1006 sheet simulated is 0.58mm. The chemical composition and the material properties of SAE 1006 are given in Table 6.2 and Table 6.3, respectively.

**Table 6.2 Chemical Composition of SAE 1006 [42]**

C%	Mn%	P%	S%	Fe%
<=0.08	<=0.45	<=0.25	<=0.15	remaining

**Table 6.3 Material Properties of SAE 1006 [43]**

R <sub>0</sub>	R <sub>45</sub>	R <sub>90</sub>	n	E(GPa)	K(MPa)	UTS (MPa)	$\sigma_y$ (MPa)	$\nu$	$\rho$ (g/mm <sup>3</sup> )
1.80	1.88	2.74	0.2609	69.1	580.86	315.51	189.73	0.3	7.8e-6

Totally, 7 different specimens are tested from uniaxial tension to biaxial tension states. The geometries of the specimens are shown in Figure 6.6.

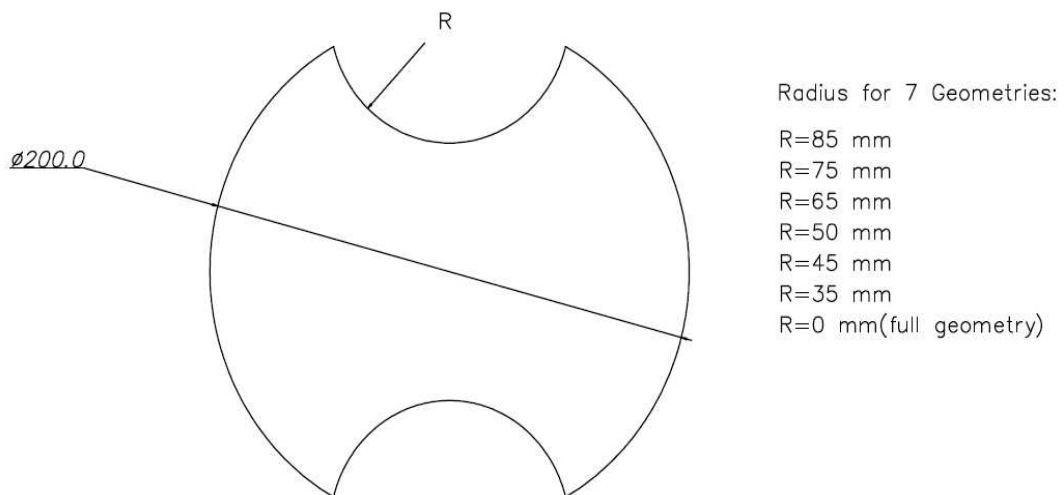


**Figure 6.6 Nakazima Geometry of SAE 1006**

The deformed states of all geometries are shown in Figure 6.7.

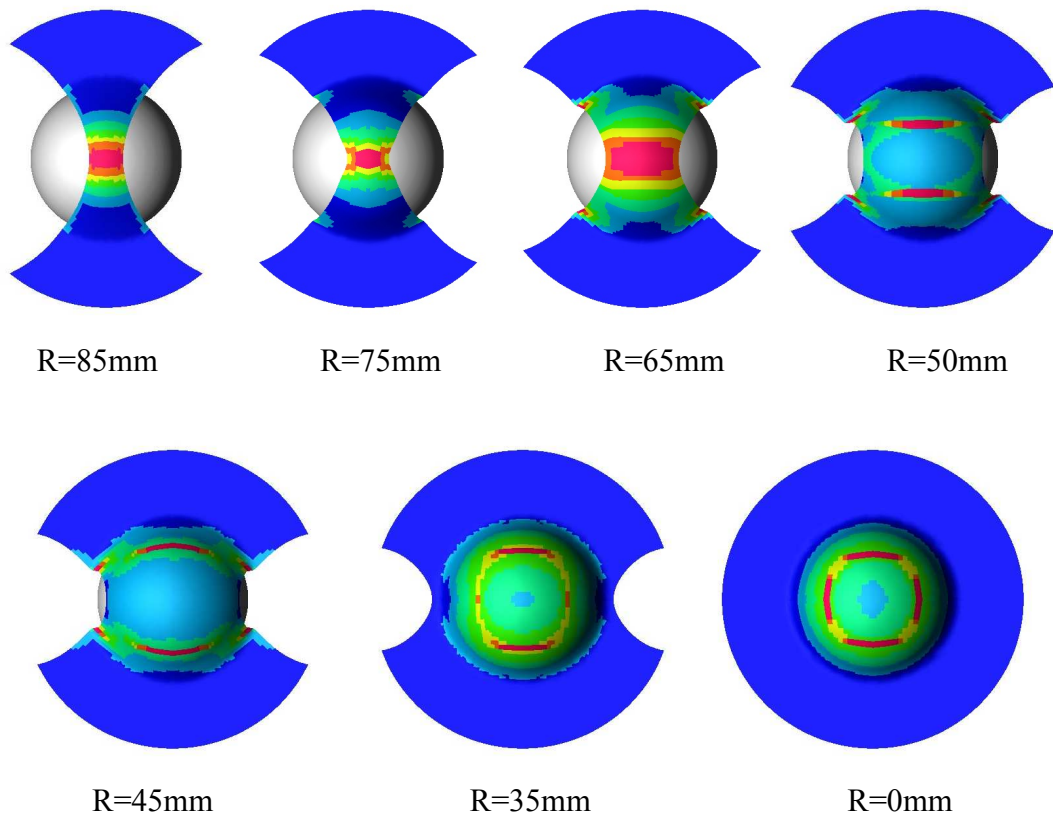


**Figure 6.7 Deformed States of the SAE 1006 Specimens**

As shown in Figure 6.7, the localization is observed at the pole for the R=85mm, R=75mm and R=65mm specimens. However, for the remaining specimens localized necking occurred at some distance from the pole, in other words on the side walls of the blank.

The total number of finite elements and nodes of the each specimen are tabulated in Table 6.3.

**Table 6.4 SAE 1006 Blank Finite Elements**

Blank radius(mm):	R=85	R=75	R=65	R=50	R=45	R=35	R=0
Number of finite elements:	2208	3464	4220	5528	5232	5428	6080
Number of nodes:	2315	3591	4357	5679	5365	5549	6181

### 6.2.2.1 Radius=85mm

The deformed geometry of the sheet is shown below:

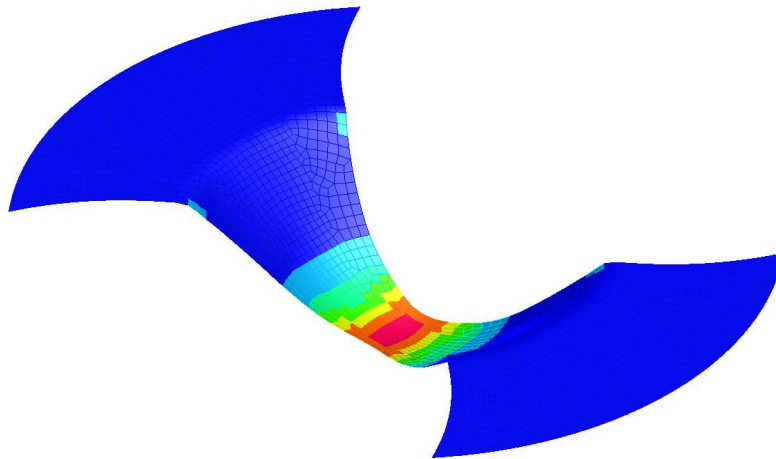


**Figure 6.8 Deformed Geometry of R=85mm**

This is the case of uniaxial tension test. The necked elements are located at the pole as seen in Figure 6.8.

The necking area of the specimen is shown in Figure 6.9. Totally six reference elements are analyzed in 2 groups which are, no.19913-no.19361-no.19419 and no.21019-no.20467-no.20576.

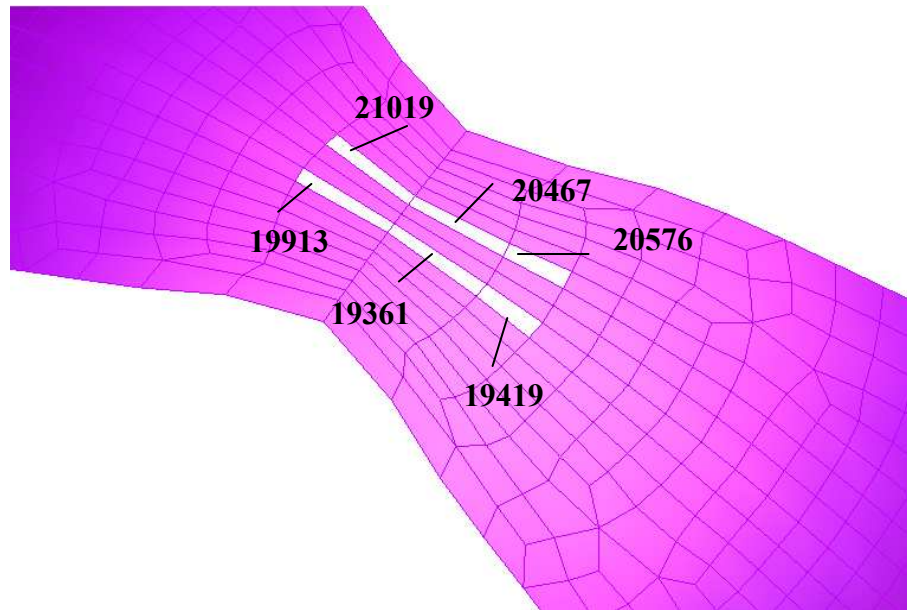


**Figure 6.9 Location of the Measuring Elements for R=85mm**

As the deformation proceeds, the equivalent strain increments of all the reference elements are traced and the time of instability is found. In strain propagation phenomena, 0 strain increment represents the instability instant since no more strain transfer can be achieved between the neighboring elements. In Figures 6.10 and 6.11, equivalent strain increments of the 2 groups of elements are shown with respect to time.

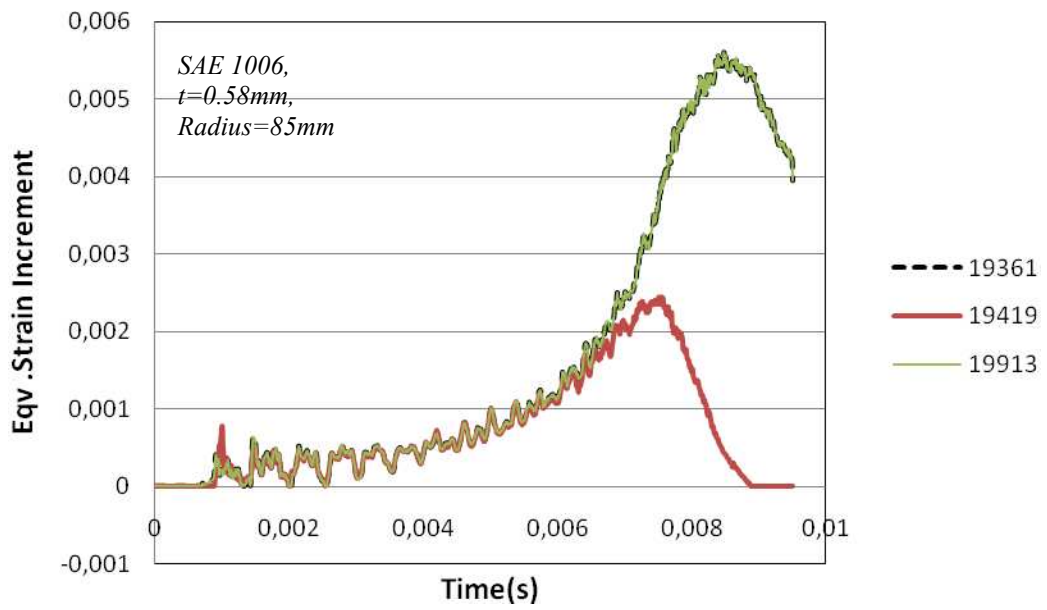


**Figure 6.10 Eqv. Strain Increments for the 1<sup>st</sup> Group Elements of R=85mm**

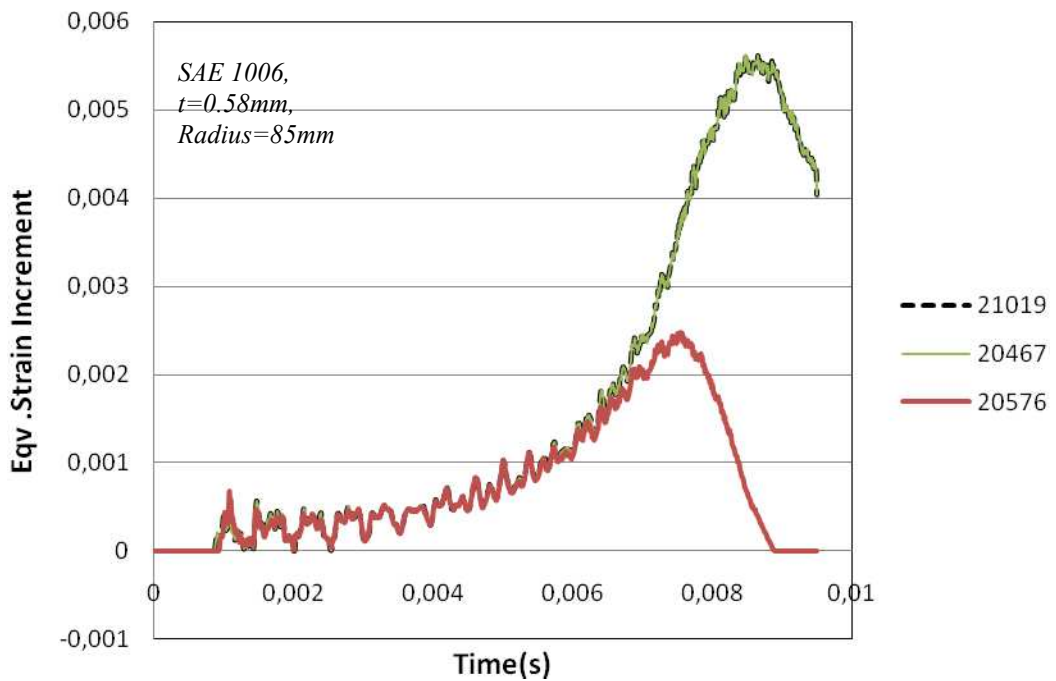


**Figure 6.11 Eqv. Strain Increments for the 2<sup>nd</sup> Group Elements of R=85mm**

As can be observed from Figure 6.10, at the beginning of the stretching period the equivalent strains for all the elements are increasing because the equivalent strain increments are positive for the 1<sup>st</sup> group. But after  $t=0.0075s$ , the strain increment of the element no.19419 starts decreasing and at  $t= 0.0088s$  it drops to 0. However, the equivalent strain increments of the elements no.19361 and no.19913 are still positive. At zero equivalent strain increment instant, major and minor strains of the element no.19419 are recorded and it constitutes the 1<sup>st</sup> limit strain point for the specimen  $R=85mm$  for the construction of the FLD.

If Figure 6.11 is analyzed, at the beginning of the stretching period, equivalent strains for all the elements are increasing because the equivalent strain increments are positive for the 2<sup>nd</sup> group. But after  $t=0.0076s$ , equivalent strain increment of the element no.20576 starts decreasing and at  $t= 0.0089s$  it drops to zero. However, the equivalent strain increments of the elements no.21019 and no.20467 are still positive. At zero equivalent strain increment instant, major and minor strains of the element no.20576 are recorded and it constitutes the 2<sup>nd</sup> limit strain point for the specimen  $R=85mm$  for the construction of the FLD.

#### **6.2.2.2 Radius=75mm**

The deformed geometry of the sheet is shown in Figure 6.12. It is observed that the necked elements are located at the pole.

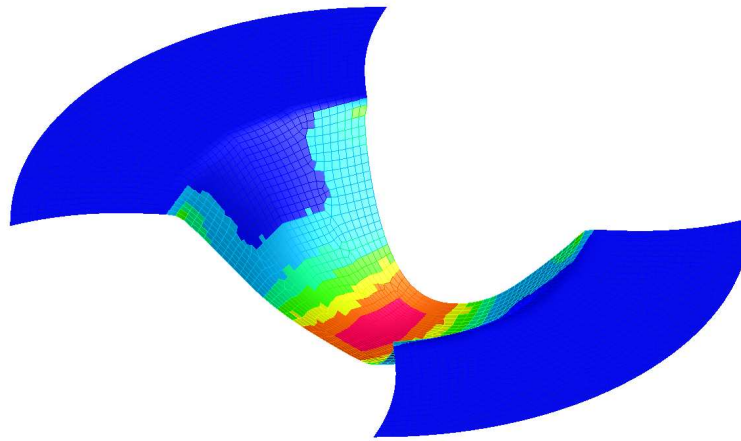


**Figure 6.12 Deformed Geometry of R=75mm**

The necking area of the specimen is shown in Figure 6.13. Totally six reference elements are analyzed in 2 groups which are, no.24204-no.22472-no.22578 and no.23335-no.21603-no.21670.

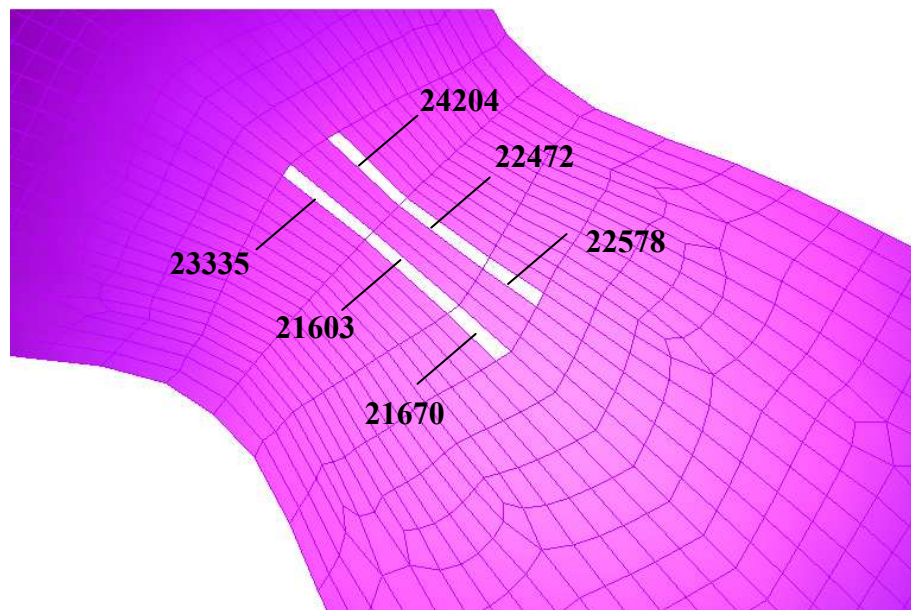


**Figure 6.13 Location of the Measuring Elements for R=75mm**

In Figures 6.14 and 6.15, equivalent strain increments of the 2 groups of elements are shown with respect to time.

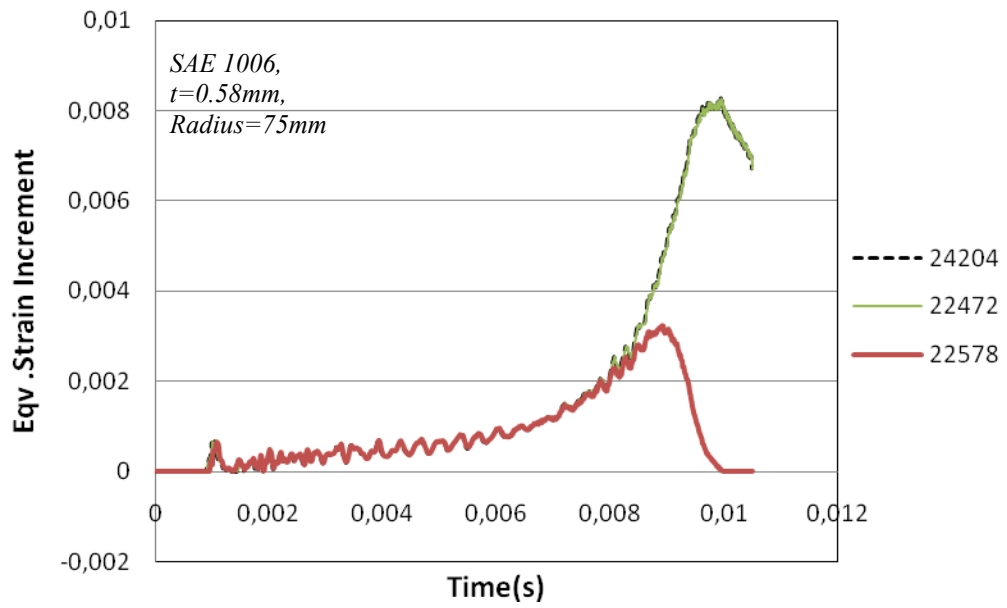


**Figure 6.14 Eqv. Strain Increments for the 1<sup>st</sup> Group Elements of R=75mm**

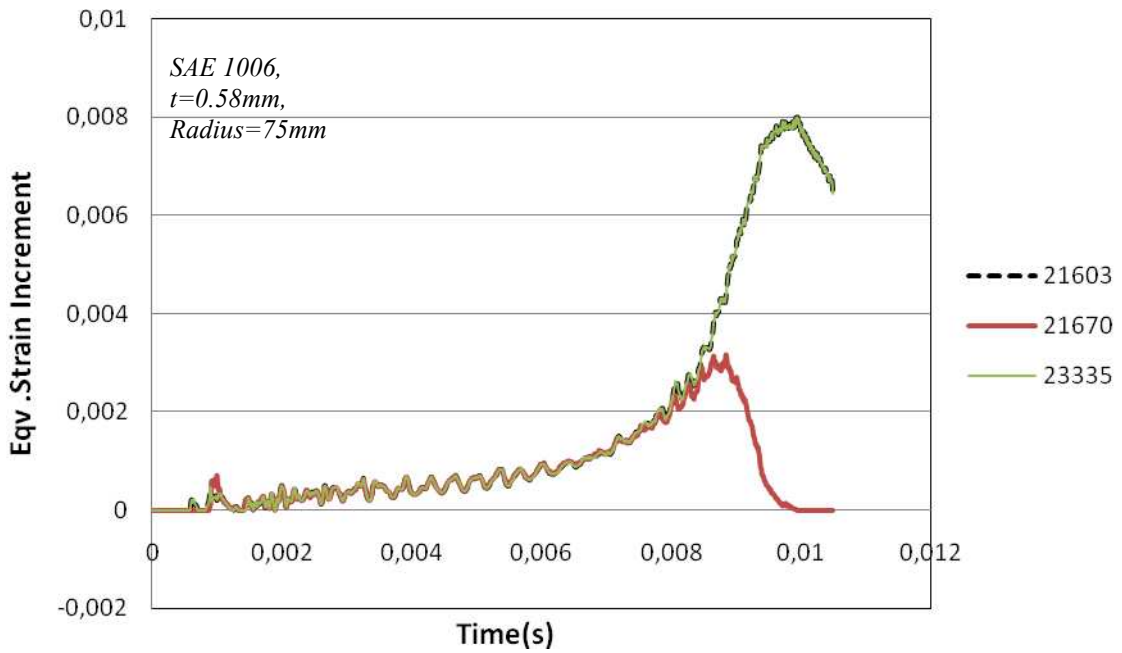


**Figure 6.15 Eqv. Strain Increments for the 2<sup>nd</sup> Group Elements of R=75mm**

As can be observed from Figure 6.14, at the beginning of the stretching period, the equivalent strains for all the elements are increasing because the equivalent strain increments are positive for the 1<sup>st</sup> group. But after  $t=0.0086s$ , the equivalent strain

increment of the element no.22578 starts decreasing and at  $t= 0.0099s$  it drops to 0. However, the equivalent strain increments of the elements no.24204 and no.22472 are still positive. At zero equivalent strain increment instant, major and minor strains of the element no.22578 are recorded and it constitutes the 1<sup>st</sup> limit strain point for the specimen  $R=75mm$  for the construction of the FLD.

If Figure 6.15 is analyzed, at the beginning of the stretching period, the equivalent strains for all the elements are increasing because the equivalent strain increments are positive for the 2<sup>nd</sup> group. After  $t=0.0086s$ , the equivalent strain increment of the element no.21670 starts decreasing and at  $t= 0.0099s$  it drops to 0. However, the equivalent strain increments of the elements no.21603 and no.23335 are still positive. At zero equivalent strain increment instant, major and minor strains of the element no.21670 are recorded and it constitutes the 2<sup>nd</sup> limit strain point for the specimen  $R=75mm$  for the construction of the FLD.

### 6.2.2.3 Radius=65mm

The deformed geometry of the sheet is shown in Figure 6.16. It can be seen that, the necked elements are located at the pole like  $R=85mm$  and  $R=75mm$  specimens.

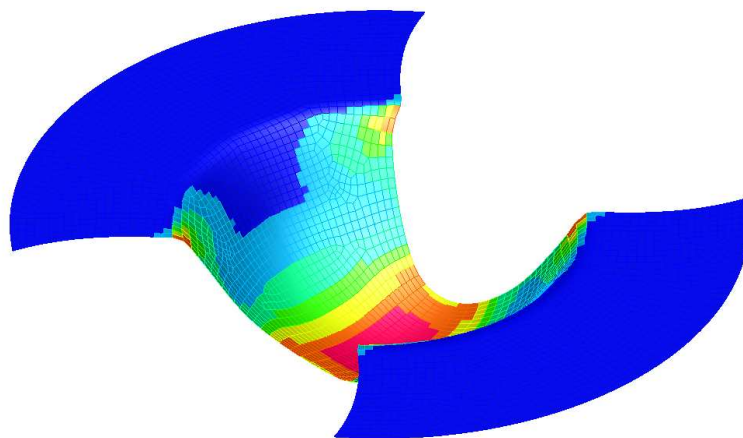


**Figure 6.16 Deformed Geometry of  $R=65mm$**

The necking area of the specimen is shown in Figure 6.17. Totally six reference elements are analyzed in 2 groups which are, no.22670-no.21615-no.21616 and no.24777-no.23722-no.23872.

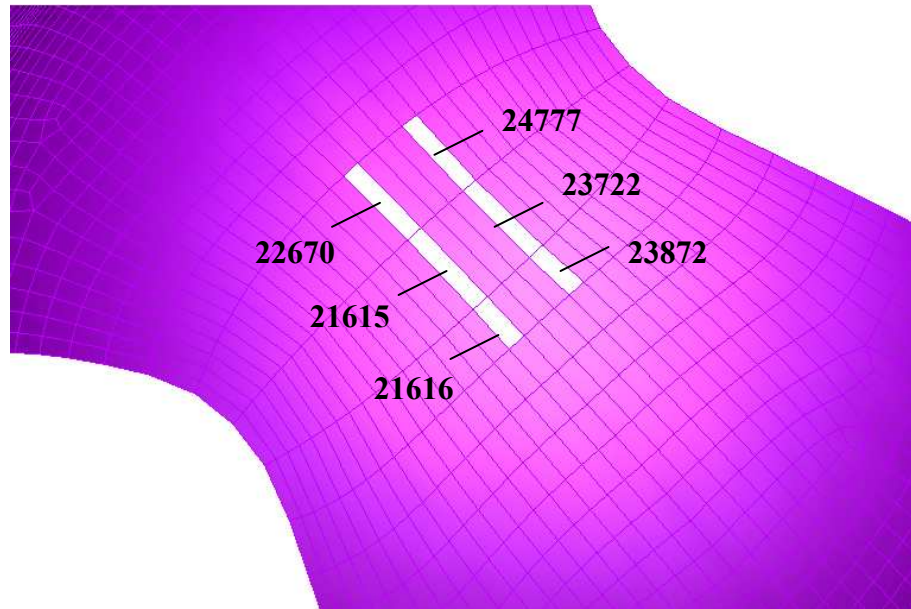


**Figure 6.17 Location of the Measuring Elements for R=65mm**

In Figures 6.18 and 6.19, equivalent strain increments of the 2 groups of elements are shown with respect to time.

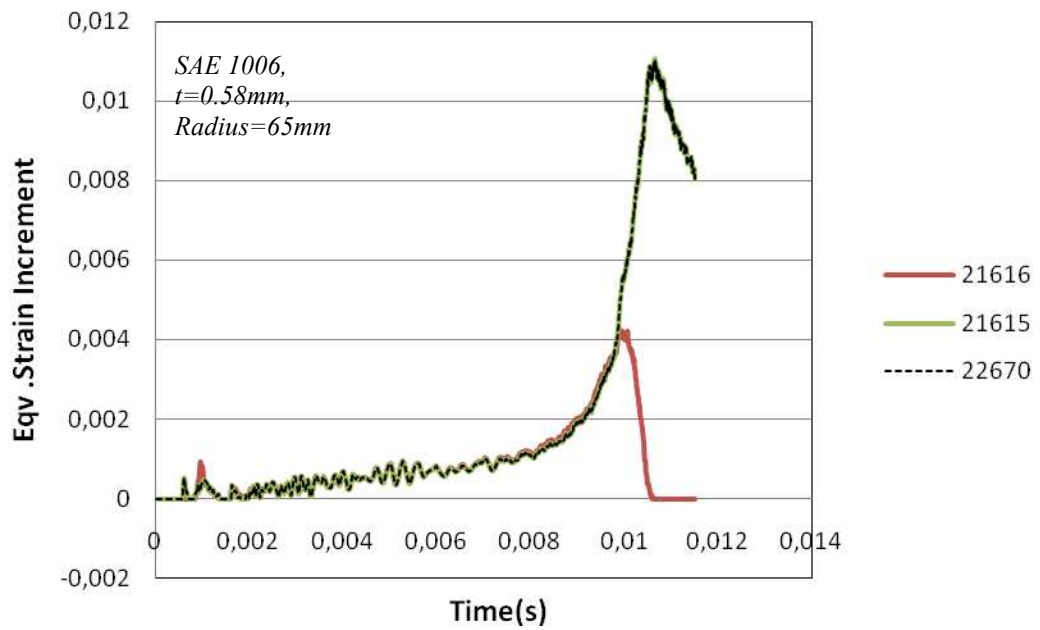


**Figure 6.18 Eqv. Strain Increments for the 1<sup>st</sup> Group Elements of R=65mm**

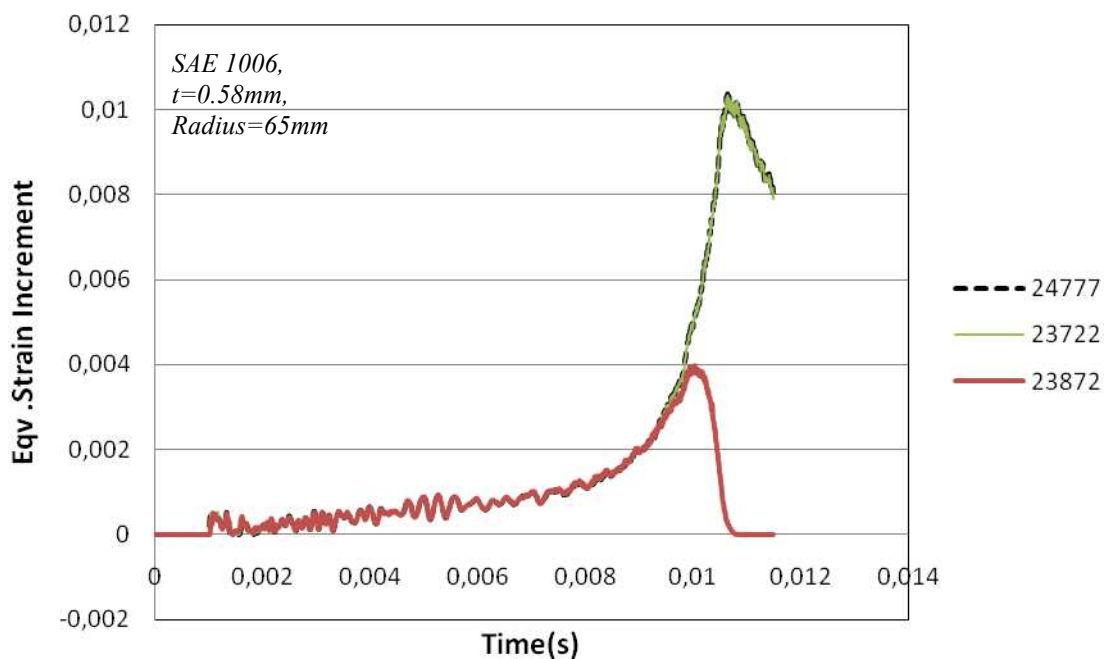


**Figure 6.19 Eqv. Strain Increments for the 2<sup>nd</sup> Group Elements of R=65mm**

As can be observed from Figure 6.18, at the beginning of the stretching period, the equivalent strains for all the elements are increasing because the equivalent strain

increments are positive for the 1<sup>st</sup> group. But after  $t=0.01s$ , equivalent strain increment of the element no.21616 starts decreasing and at  $t= 0.0106s$  it drops to 0. However, the equivalent strain increments of the elements no.21615 and no.22670 are still positive. At zero equivalent strain increment instant, major and minor strains of the element no.21616 are recorded and it constitutes the 1<sup>st</sup> limit strain point for the specimen  $R=65mm$  for the construction of the FLD.

If Figure 6.19 is analyzed, at the beginning of the stretching period, the equivalent strains for all the elements are increasing because the equivalent strain increments are positive for the 2<sup>nd</sup> group. But after  $t=0.0101s$ , equivalent strain increment of the element no.23872 starts decreasing and at  $t= 0.0108s$  it drops to 0. However, the equivalent strain increments of the elements no.21615 and no.22670 are still positive. At zero equivalent strain increment instant, major and minor strains of the element no.23872 are recorded and it constitutes a limit strain point for the specimen  $R=65mm$  for the construction of the FLD.

#### **6.2.2.4 Radius=50mm**

The deformed geometry of the sheet is shown in Figure 6.20. It can be observed that the necked elements are located at the wall of the blank (punch radius).

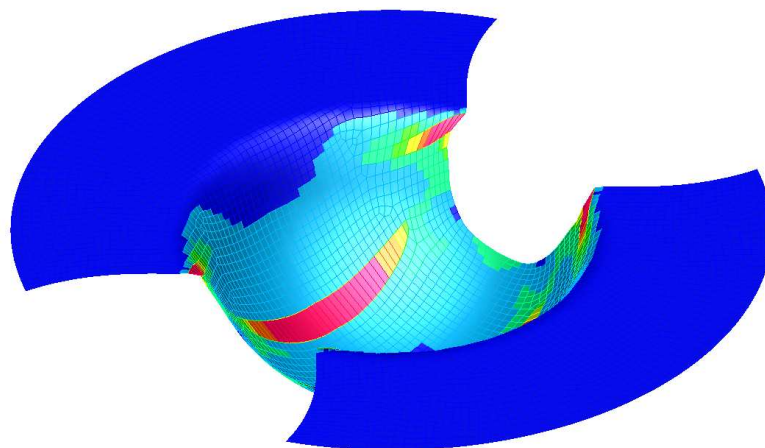


**Figure 6.20 Deformed Geometry of  $R=50mm$**

The necking area of the specimen is shown in Figure 6.21. Totally six reference elements are analyzed in 2 groups which are, no.25788-no.25789-no.25790 and no.24935-no.24936-no.24937.

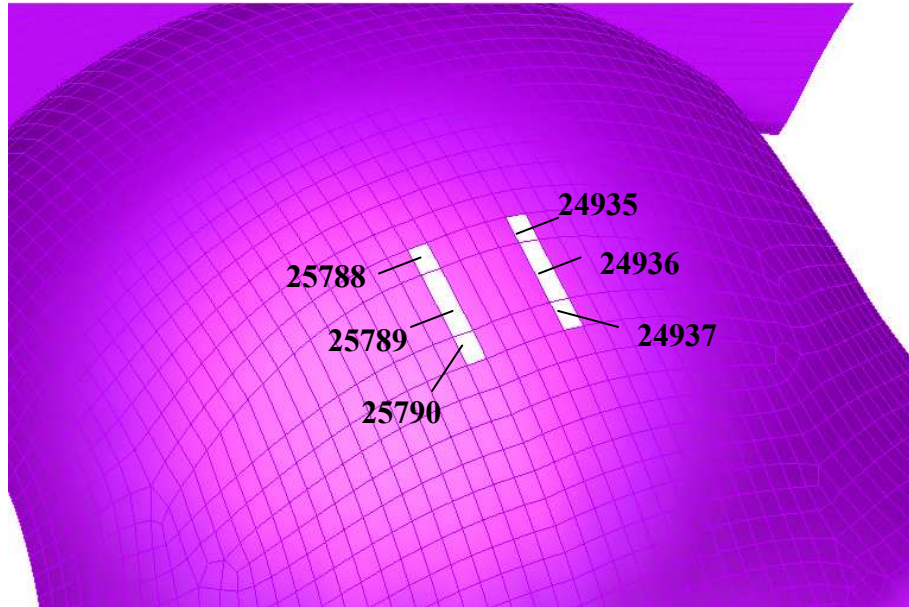


**Figure 6.21 Location of the Measuring Elements for R=50mm**

In Figures 6.22 and 6.23, equivalent strain increments of the 2 groups of elements are shown with respect to time.

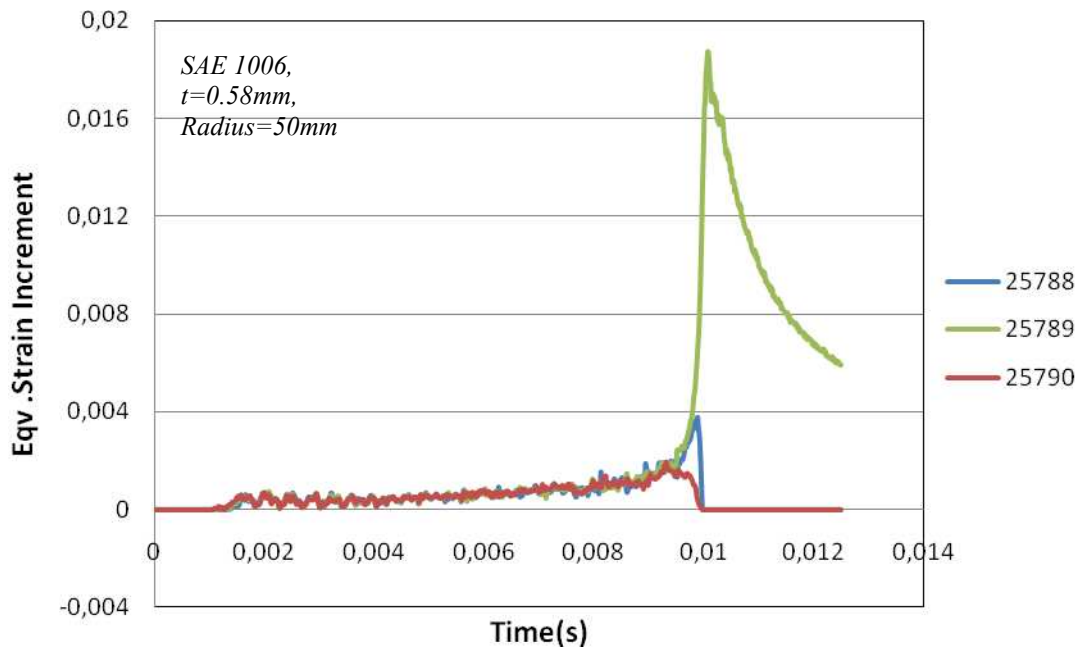


**Figure 6.22 Eqv. Strain Increments for the 1<sup>st</sup> Group Elements of R=50mm**

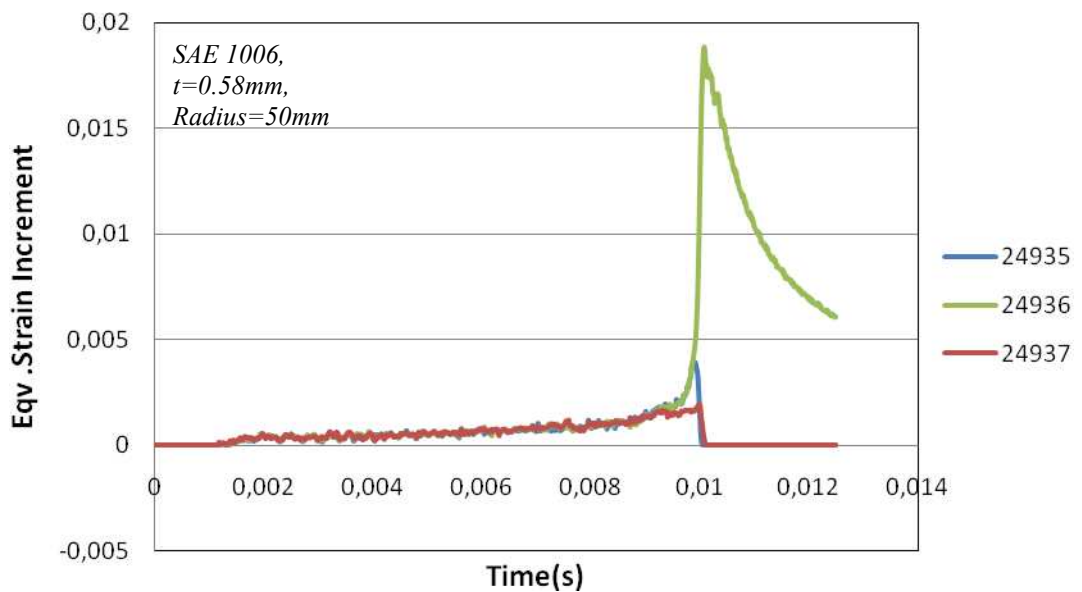


**Figure 6.23 Eqv. Strain Increments for the 2<sup>nd</sup> Group Elements of R=50mm**

As can be observed from Figure 6.22, at the beginning of the stretching period, the equivalent strains for all the elements are increasing because the equivalent strain

increments are positive for the 1<sup>st</sup> group. But after  $t=0.0093s$ , equivalent strain increment of the element no.25790 starts decreasing. The strain increment of the element no.25788 also starts decreasing at  $t= 0.0098s$ . At  $t=0.0099s$  both of the equivalent strain increments of the elements reach to zero. However, the equivalent strain increment of the element no.25789 is still positive. At zero equivalent strain increment instant, major and minor strains of the element no.25788 are recorded and it constitutes the 1<sup>st</sup> limit strain point for the specimen  $R=50mm$  for the construction of the FLD.

If Figure 6.23 is analyzed, at the beginning of the stretching period, the equivalent strains for all the elements are increasing because the equivalent strain increments are positive for the 2<sup>nd</sup> group. But after  $t=0.0099s$ , equivalent strain increment of the element no.24935 starts decreasing. The equivalent strain increment of the element no.24937 also starts decreasing at  $t= 0.00995s$ . At  $t= 0.01s$  both of the strain increments of the elements reach to zero. However, the equivalent strain increment of the element no.24936 is still positive. At zero equivalent strain increment instant, major and minor strains of the element no.24935 are recorded and it constitutes the 2<sup>nd</sup> limit strain point for the specimen  $R=50mm$  for the construction of the FLD.

#### **6.2.2.5 Radius=45mm**

The deformed geometry of the sheet is shown in Figure 6.24. The necked elements are located at the blank wall (punch radius) as the specimen  $R=50mm$ .

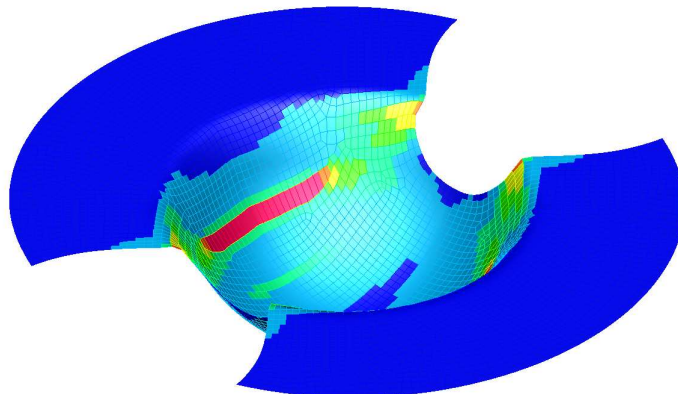


**Figure 6.24 Deformed Geometry of  $R=45mm$**

The necking area of the specimen is shown in Figure 6.25. Totally six reference elements are analyzed in 2 groups which are, no.22938-no.22939-no.22940 and no.23423-no.23424-no.23425.

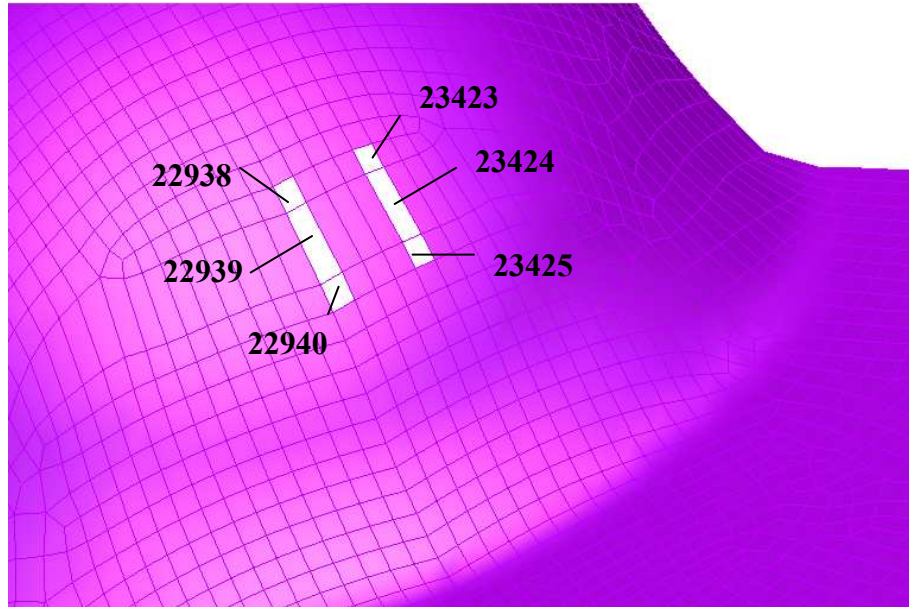


**Figure 6.25 Location of the Measuring Elements for R=45mm**

In Figures 6.26 and 6.27, equivalent strain increments of the 2 groups of elements are shown with respect to time.

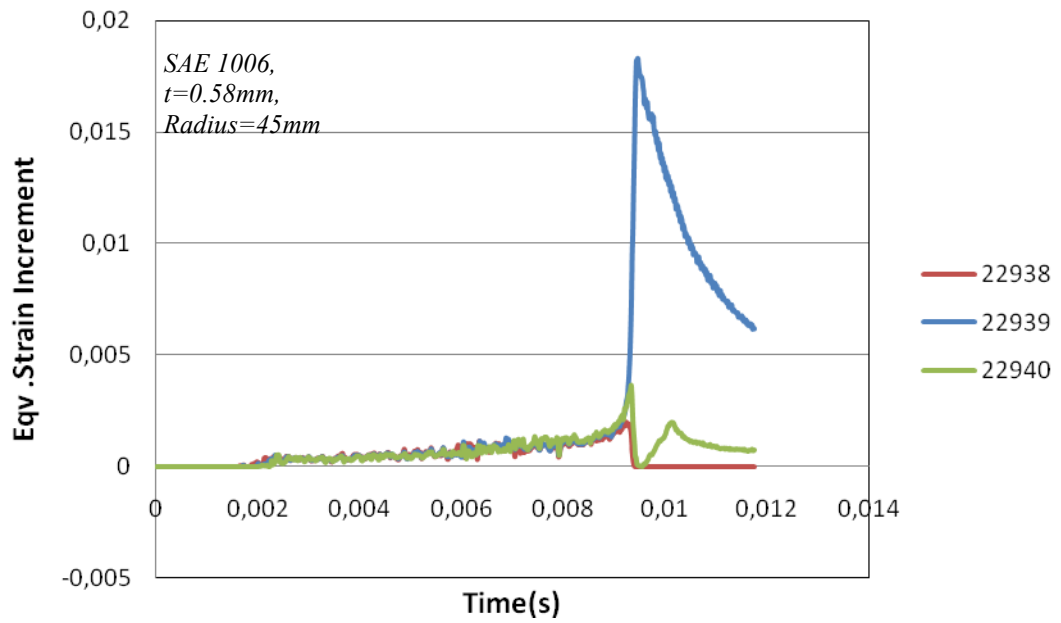


**Figure 6.26 Eqv. Strain Increments for the 1<sup>st</sup> Group Elements of R=45mm**

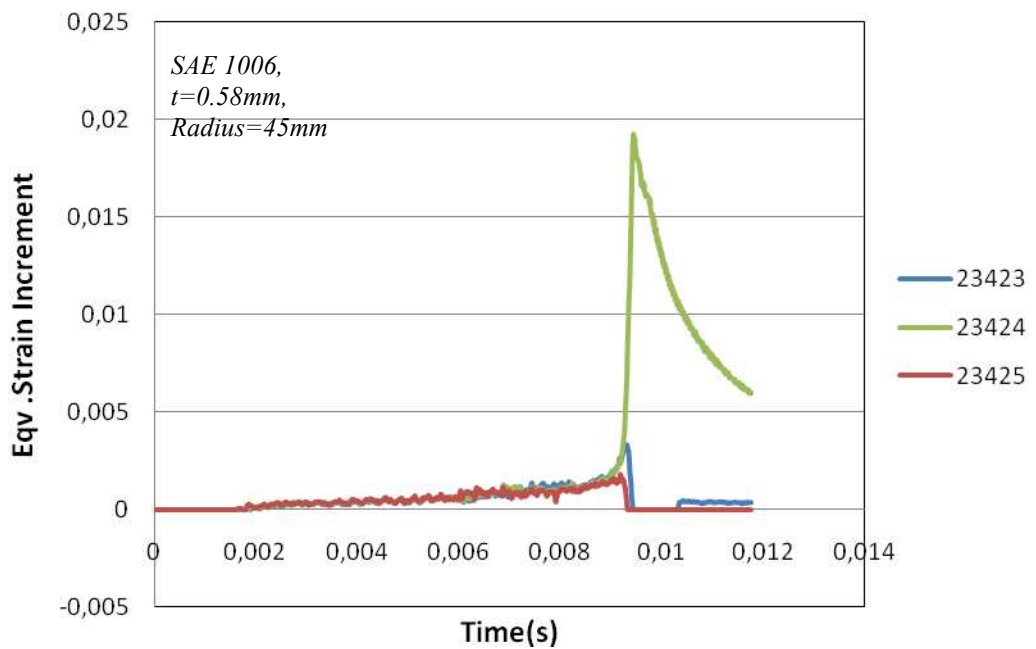


**Figure 6.27 Eqv. Strain Increments for the 2<sup>nd</sup> Group Elements of R=45mm**

As can be observed from Figure 6.26, at the beginning of the stretching period, the equivalent strains for all the elements are increasing because the equivalent strain increments are positive for the 1<sup>st</sup> group. But after  $t=0.0092s$ , equivalent strain

increment of the element no.22938 starts decreasing. Then, equivalent strain increment of the element no.22940 starts decreasing at  $t= 0.0098s$ . Finally, at  $t= 0.0094s$ , the strain increment of the element no.22938 reach to zero. The equivalent strain increment of the element no.22940 drops to zero at  $t= 0.0099s$  and then it suddenly increases and decreases again. However, the equivalent strain increment of the element no.22939 is still positive. At zero equivalent strain increment instant, major and minor strains of the element no.22938 are recorded and it constitutes the 1<sup>st</sup> limit strain point for the specimen  $R=45mm$  for the construction of the FLD.

If Figure 6.26 is analyzed, at the beginning of the stretching period, the equivalent strains for all the elements are increasing because the equivalent strain increments are positive for the 2<sup>nd</sup> group. But after  $t=0.0091s$ , the equivalent strain increment of the element no.23425 starts decreasing and at  $t= 0.0093s$  it drops to 0. Then, the strain increment of the element no.23423 drops to zero at  $t=0.0094$ . However, the equivalent strain increment of the element no.23424 is still positive. At zero equivalent strain increment instant, major and minor strains of the element no.23425 are recorded and it constitutes the 2<sup>nd</sup> limit strain point for the specimen  $R=45mm$  for the construction of the FLD.

#### **6.2.2.6 Radius=35mm**

The deformed geometry of the sheet is shown in Figure 6.24. The necked elements are located at the blank wall (punch radius) as expected.

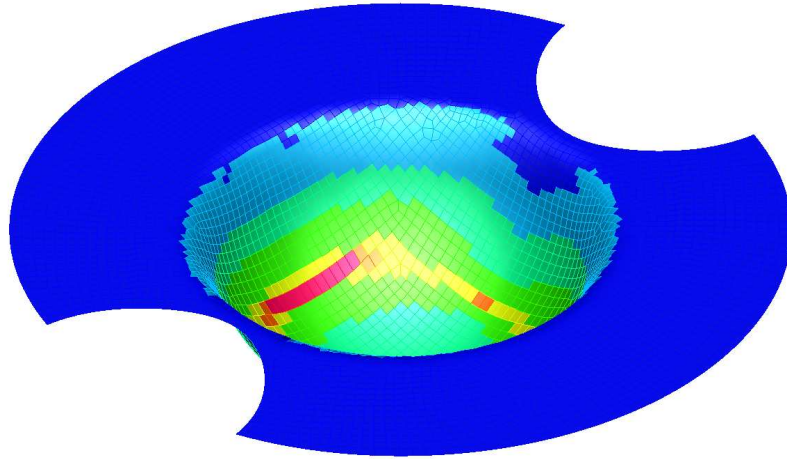


**Figure 6.28 Deformed Geometry of R=35mm**

The necking area of the specimen is shown in Figure 6.29. Totally six reference elements are analyzed in 2 groups which are, no.22939-no.22940-no.22941 and no.23471-no.23472-no.23473.

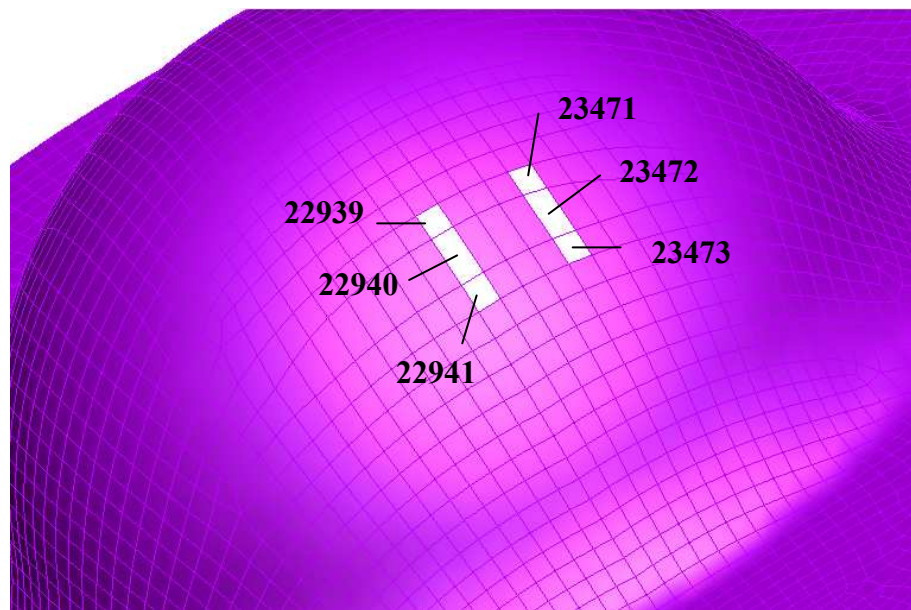


**Figure 6.29 Location of the Measuring Elements for R=35mm**

In Figures 6.30 and 6.31, equivalent strain increments of the 2 groups of elements are shown with respect to time.

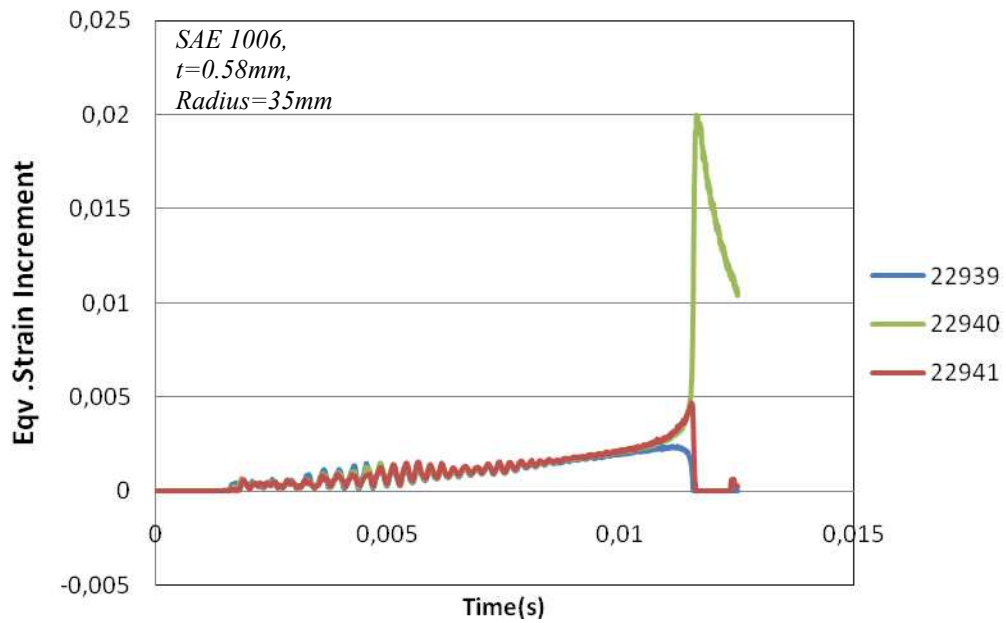


**Figure 6.30 Eqv. Strain Increments for the 1<sup>st</sup> Group Elements of R=35mm**

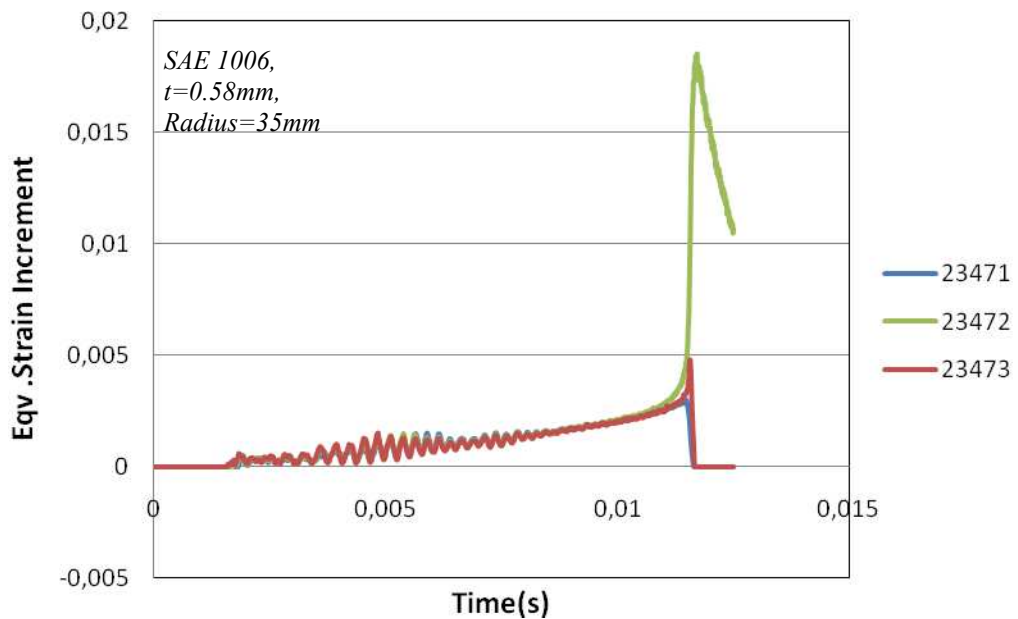


**Figure 6.31 Eqv. Strain Increments for the 2<sup>nd</sup> Group Elements of R=35mm**

As can be observed from Figure 6.30, at the beginning of the stretching period, the equivalent strains for all the elements are increasing because the equivalent strain increments are positive for the 1<sup>st</sup> group. But after  $t=0.0101s$ , the equivalent strain

increment of the element no.22939 starts decreasing. Also, the strain increment of the element no.22941 starts decreasing at  $t= 0.0114s$ . At  $t= 0.0115s$ , the strain increment of the element no.22939 reach to zero. Then, the strain increment of element no.22941 drops to zero suddenly at  $t= 0.0116s$ . However, the equivalent strain increment of the element no.22940 is still positive. At zero equivalent strain increment instant, major and minor strains of the element no.22939 are recorded and it constitutes the 1<sup>st</sup> limit strain point for the specimen  $R=35mm$  for the construction of the FLD.

If Figure 6.31 is analyzed, at the beginning of the stretching period the equivalent strains for all the elements are increasing because the equivalent strain increments are positive for the 2<sup>nd</sup> group. But after  $t=0.0114s$ , the rate of equivalent strain of the element no.23471 starts decreasing and at  $t= 0.0116s$  it drops to 0. In addition, the strain rate of element no.23473 drops to zero at  $t=0.0115$ . However, the equivalent strain rate of the element no.23472 continues increasing. At zero equivalent strain rate instant, major and minor strains of the element no.23471 are recorded and it constitutes the 2<sup>nd</sup> limit strain point for the specimen  $R=35mm$  for the construction of the FLD.

#### **6.2.2.7 Radius=0mm**

Radius=0mm geometry represents the condition of biaxial stretching. The deformed state of the specimen is shown in Figure 6.32. The necked elements are located at the wall of the blank.

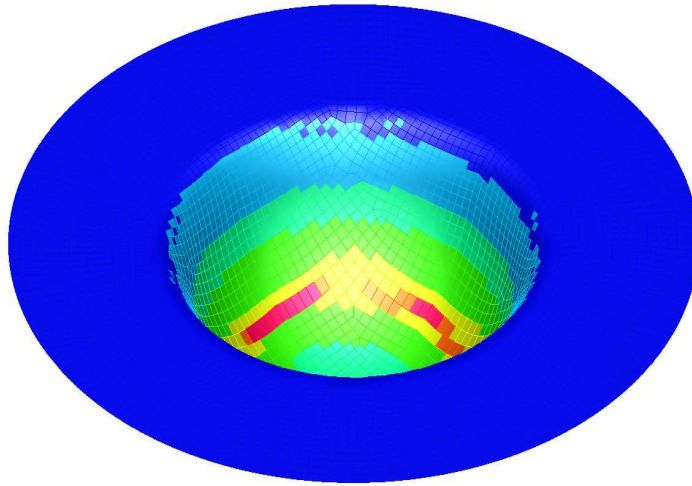


**Figure 6.32 Deformed Geometry of R=0mm**

The necking area of the specimen is shown in Figure 6.33. Totally six reference elements are analyzed in 2 groups which are, no.23139-no.23140-no.23150 and no.23139-no.23140-no.23141.

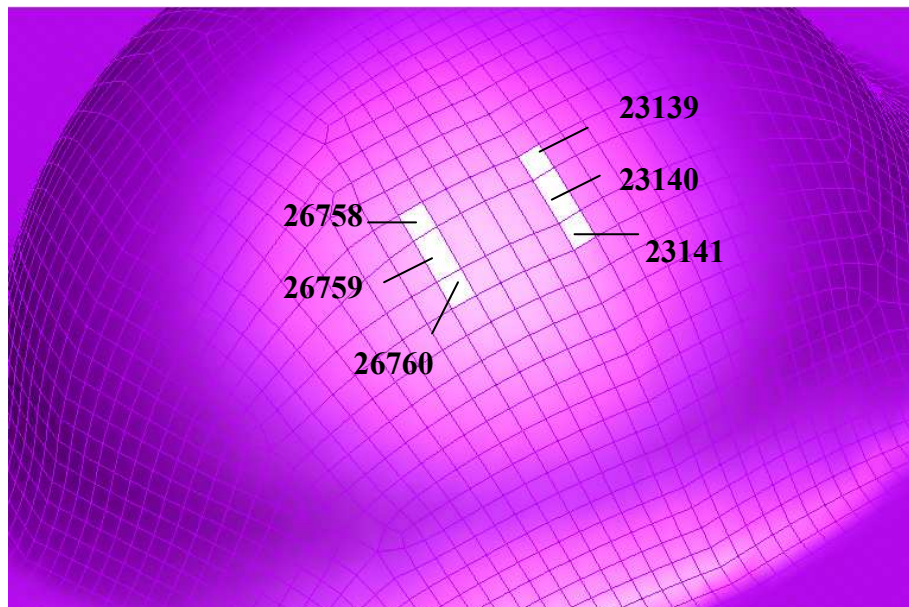


**Figure 6.33 Location of the Measuring Elements for R=0mm**

In Figures 6.34 and 6.35, equivalent strain increments of the 2 groups of elements are shown with respect to time.

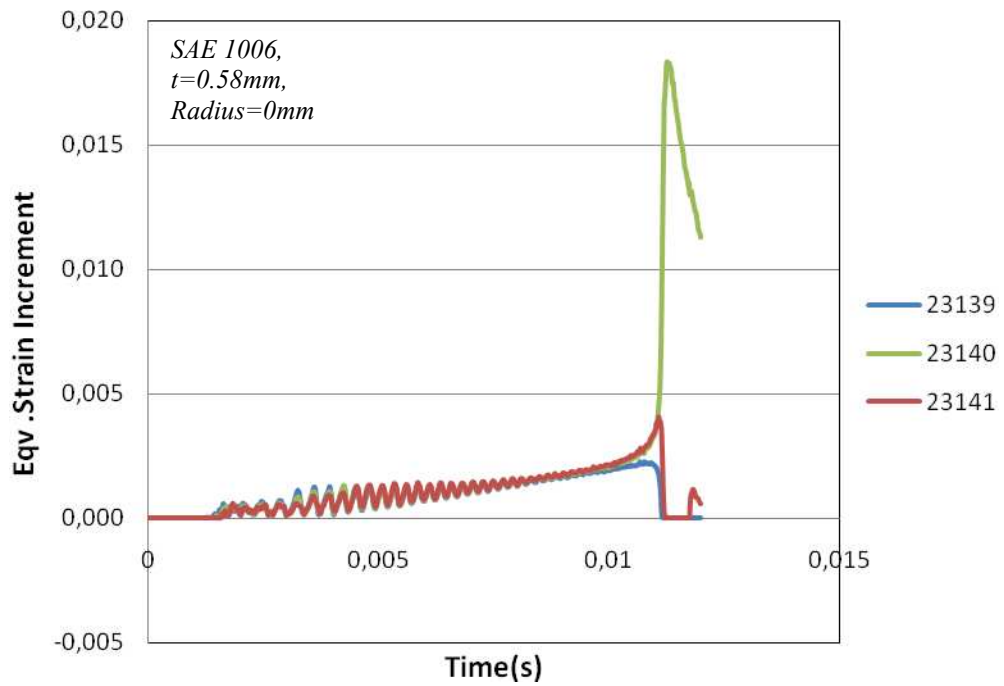


Figure 6.34 Eqv. Strain Increments for the 1<sup>st</sup> Group Elements of R=0mm

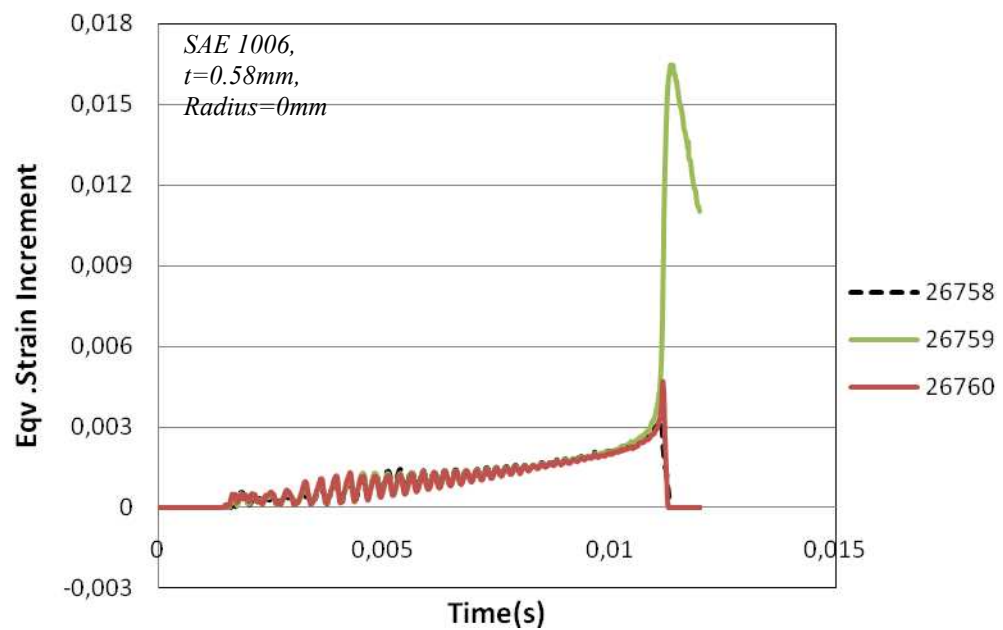


Figure 6.35 Eqv. Strain Increments for the 2<sup>nd</sup> Group Elements of R=0mm

As can be observed from Figure 6.34, at the beginning of the stretching period, the equivalent strains for all the elements are increasing because the equivalent strain increments are positive for the 1<sup>st</sup> group. But after  $t=0.0107s$ , the equivalent strain increment of the element no.23139 starts decreasing. Also, the strain increment of the element no.22141 starts decreasing at  $t= 0.0114s$ . Then, at  $t= 0.0111s$ , the strain increment of the element no.22939 reach to zero. However, the equivalent strain increment of the element no.23140 is still positive. At zero equivalent strain increment instant, major and minor strains of the element no.23139 are recorded and it constitutes the 1<sup>st</sup> limit strain point for the specimen  $R=0mm$  for the construction of the FLD.

If Figure 6.35 is analyzed, at the beginning of the stretching period, the equivalent strains for all the elements are increasing because the equivalent strain increments are positive for the 2<sup>nd</sup> group. But after  $t=0.0111s$ , the equivalent strain increment of the element no.26760 starts decreasing. The strain increment curve of the element no.26758 shows very similar behavior with element no.26760. At  $t= 0.0113s$  the strain increment of the element no.26760 drops to 0. However, the equivalent strain increment of the element no.26759 is still positive. At zero equivalent strain increment instant, major and minor strains of the element no.26760 are recorded and it constitutes the 2<sup>nd</sup> limit strain point for the specimen  $R=0mm$  for the construction of the FLD.

### **6.2.3 Analysis of AA2024-O**

The thickness of the aluminum AA2024-O sheet simulated is 0.81mm. The chemical composition and the material properties are given in Table 6.4 and Table 6.5, respectively.

**Table 6.5 Chemical Composition of AA2024-O [41]**

Si%	Fe%	Cu%	Mn%	Mg%	Cr%	Zn%	Ti%	Unspecified other elements %	Al%
0.5	0.5	3.8-4.9	0.3-0.9	1.2-1.8	0.1	0.25	0.15	0.15	remaining

**Table 6.6 Material Properties of AA2024-O [43]**

R <sub>0</sub>	R <sub>45</sub>	R <sub>90</sub>	n	E(GPa)	K(MPa)	UTS (MPa)	$\sigma_y$ (MPa)	$\nu$	$\rho$ (g/mm <sup>3</sup> )
0.59	0.8	0.73	0.2528	59.4	344.37	176.81	69.59	0.33	2.73e-6

Totally, 7 different specimens are tested from uniaxial tension to biaxial tension states as performed for SAE 1006 in the previous section. The geometries of the specimens are shown in Figure 6.36.

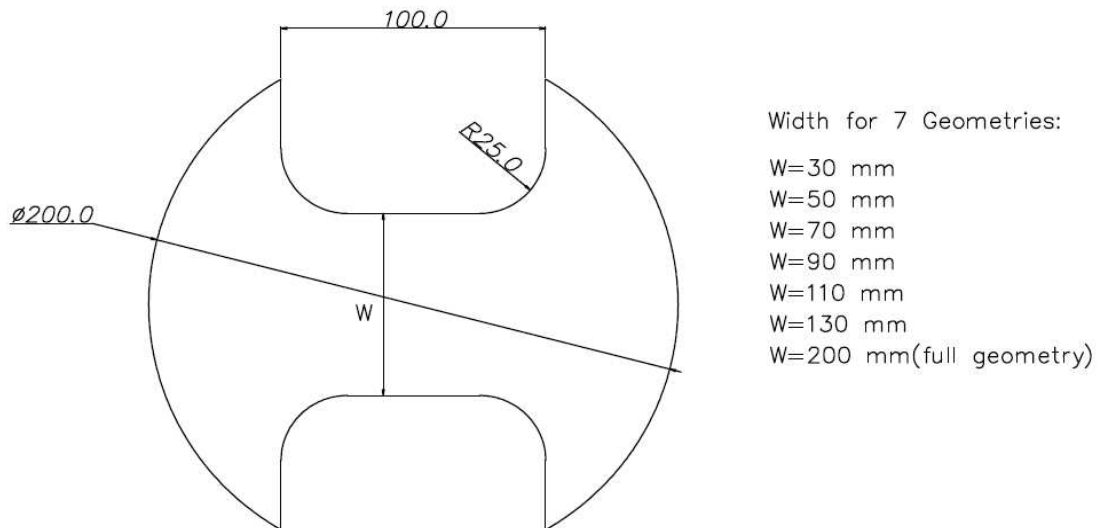


**Figure 6.36 Nakazima Geometry of Aluminum**

The deformed states of all geometries are shown in Figure 6.37.

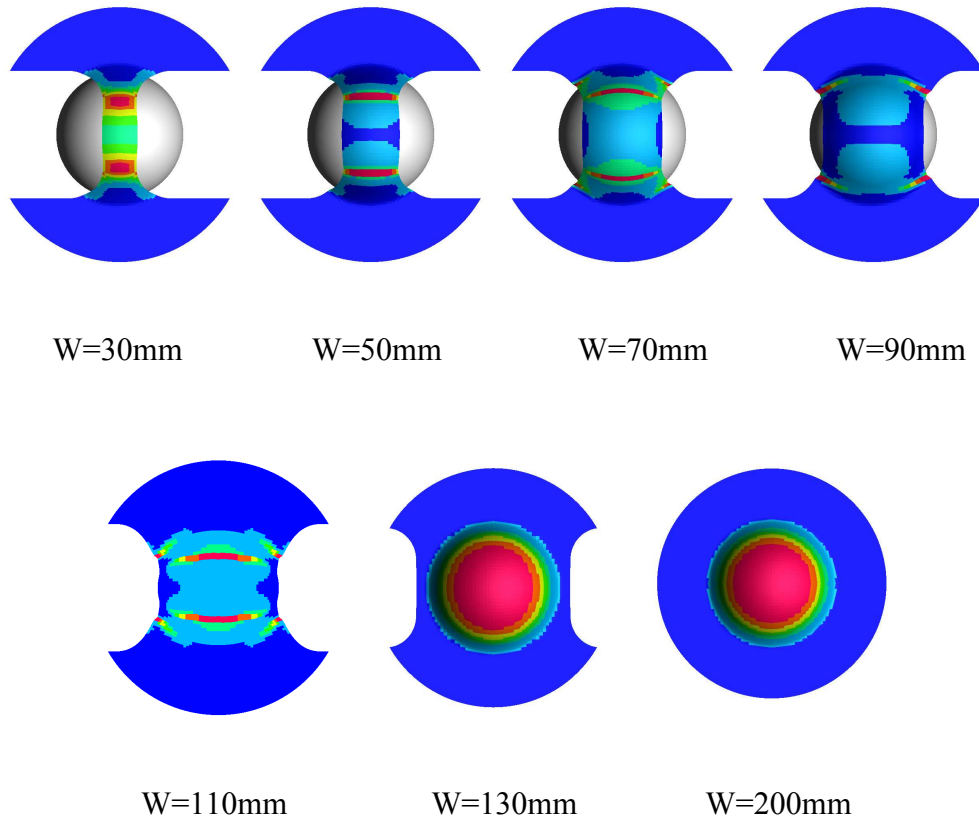


**Figure 6.37 Deformed States of the AA2024-O Specimens**

As shown in Figure 6.37, the localization observed along the punch radius for the W=30mm, W=50mm, W=70mm and W=110mm specimens. However, for the remaining specimens localized necking did not occurred on a specific location except for W=90mm. For W=90mm localization occurred on the die radius.

The total number of finite elements and nodes of the each specimen are tabulated in Table 6.6 below.

**Table 6.7 AA2024-O Blank Finite Elements**

Blank radius(mm):	W=30	W=50	W=70	W=90	W=110	W=130	W=200
Number of finite elements:	3160	3808	4040	4340	4552	4588	6080
Number of nodes:	3337	3993	4205	4493	4691	4699	6181

### 6.2.3.1 Width=30mm

The deformed geometry of the sheet is shown below:

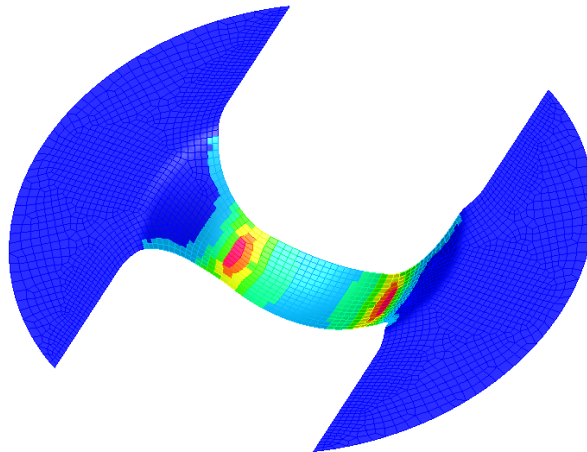


**Figure 6.38 Deformed Geometry of W=30mm**

This is the case of uniaxial tension test. The necked elements are located at the blank wall (punch radius) as seen in Figure 6.38.

The necking area of the specimen is shown in Figure 6.39. Totally six reference elements are analyzed in 2 groups which are, no.57572-no.57573-no.57574 and no.59263-no.59264-no.59265.

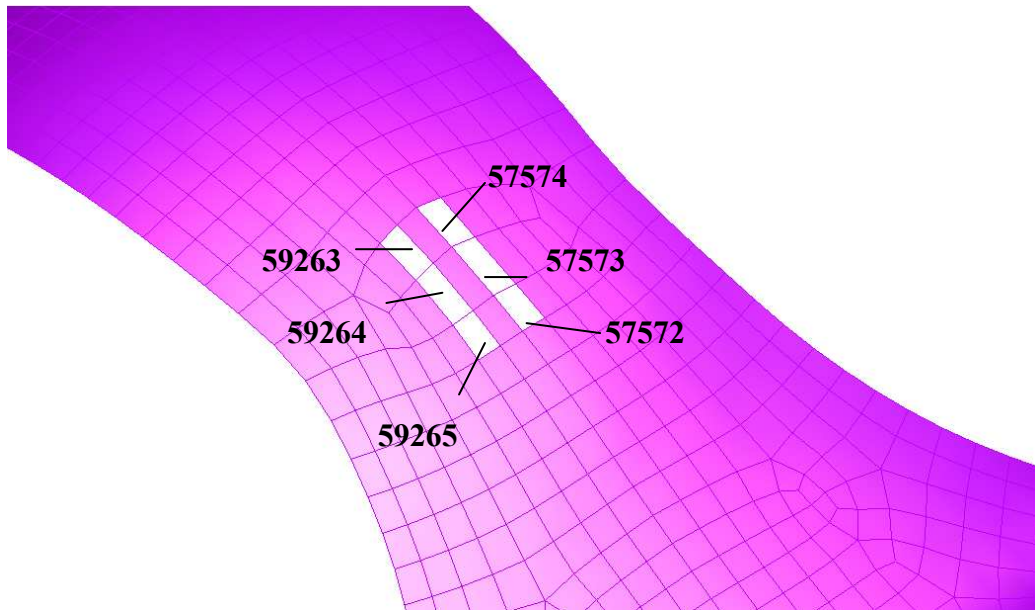


**Figure 6.39 Location of the Measuring Elements for W=30mm**

In Figures 6.40 and 6.41, equivalent strain increments of the 2 groups of elements are shown with respect to time.

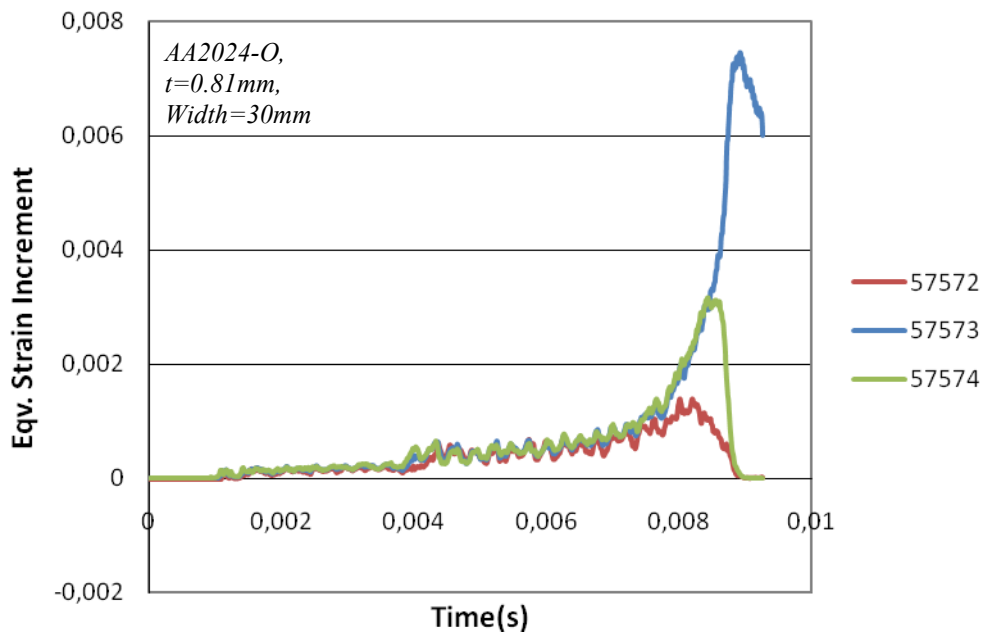


**Figure 6.40 Eqv. Strain Increments for the 1<sup>st</sup> Group Elements of W=30mm**

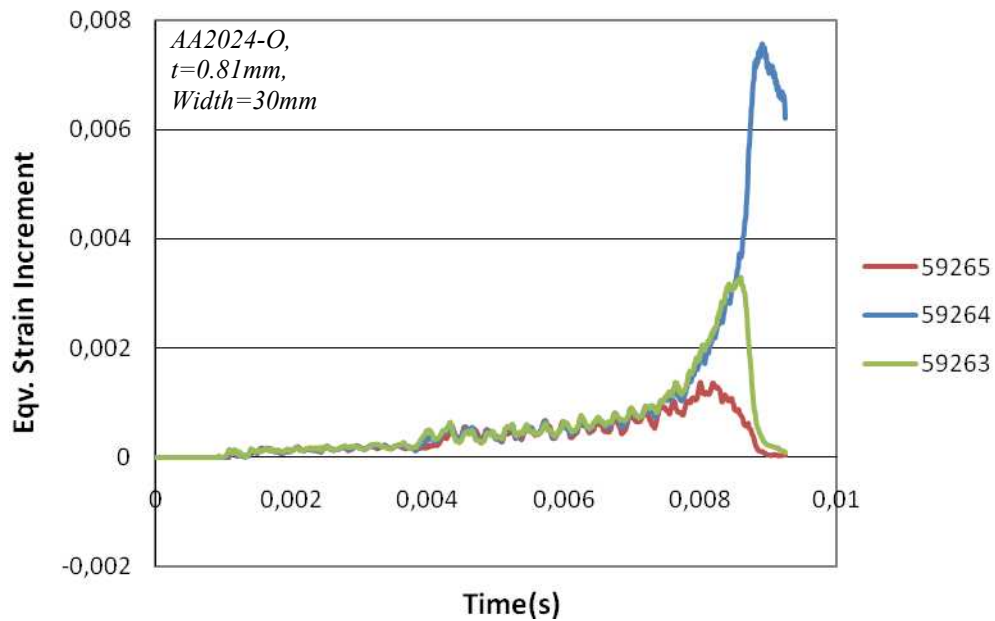


**Figure 6.41 Eqv. Strain Increments for the 2<sup>nd</sup> Group Elements of W=30mm**

As can be observed from Figure 6.40, at the beginning of the stretching period, the equivalent strains for all the elements are increasing because the equivalent strain increments are positive for the 1<sup>st</sup> group. But after  $t=0.0082s$ , the equivalent strain increment of the element no.57572 starts decreasing. Also, equivalent strain increment of the element no.57574 starts decreasing suddenly at  $t= 0.0084s$ . At  $t=0.0090s$  the strain increment of the element no.57574 reach to zero. However, the equivalent strain increment of the element no.57573 is still positive. At zero equivalent strain increment instant, major and minor strains of the element no.57574 are recorded and it constitutes the 1<sup>st</sup> limit strain point for the specimen W=30mm for the construction of the FLD.

If Figure 6.41 is analyzed, at the beginning of the stretching period, the equivalent strains for all the elements are increasing because the equivalent strain increments are positive for the 2<sup>nd</sup> group. But after  $t=0.0080s$ , the equivalent strain increment of the element no.59265 starts decreasing. Also, the strain increment of the element no.59263 starts decreasing at  $t= 0.0085s$ . Finally, at  $t= 0.0092s$ , the equivalent strain increments of the element no.59265 reach to zero. However, the equivalent strain increment of the element no.59264 is still positive. At zero equivalent strain

increment instant, major and minor strains of the element no.59265 are recorded and it constitutes the 2<sup>nd</sup> limit strain point for the specimen W=30mm for the construction of the FLD.

### 6.2.3.2 Width=50mm

The deformed geometry of the sheet is shown in Figure 6.42. It can be observed that the necked elements are located at the wall of the blank (punch radius).

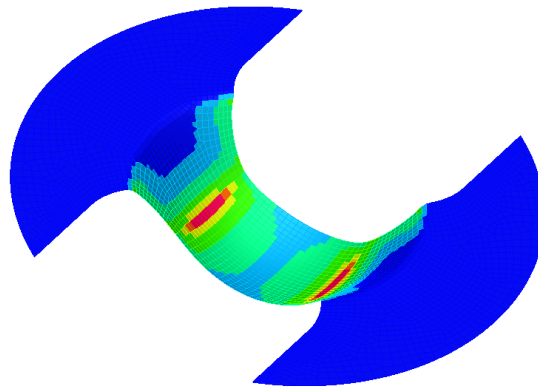


**Figure 6.42 Deformed Geometry of W=50mm**

The necking area of the specimen is shown in Figure 6.43. Totally six reference elements are analyzed in 2 groups which are, no.61198-no.61199-no.61200 and no.59950-no.59951-no.59952.

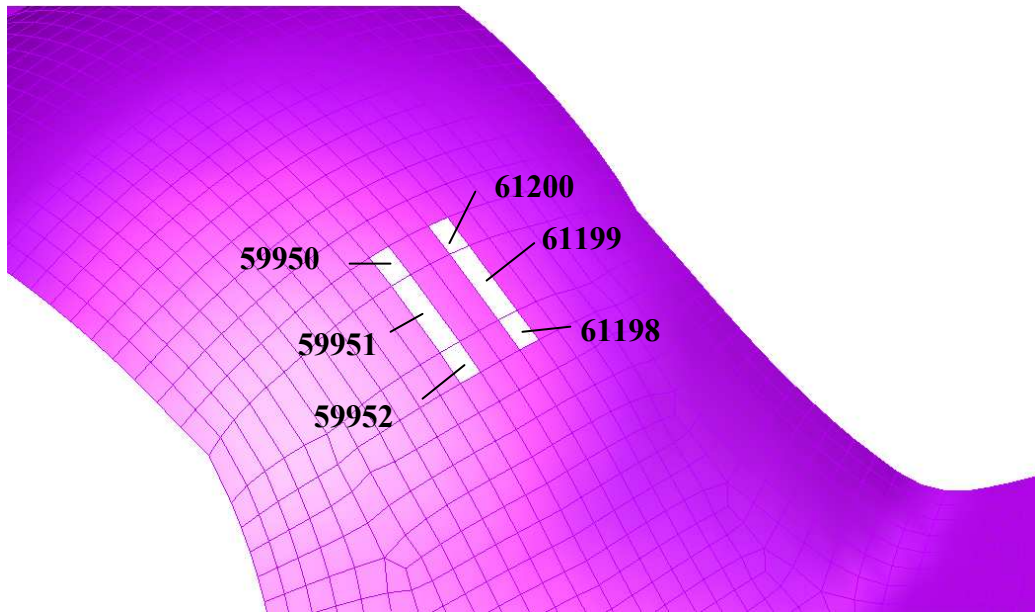


**Figure 6.43 Location of the Measuring Elements for W=50mm**

In Figures 6.44 and 6.45, equivalent strain increments of the 2 groups of elements are shown with respect to time.

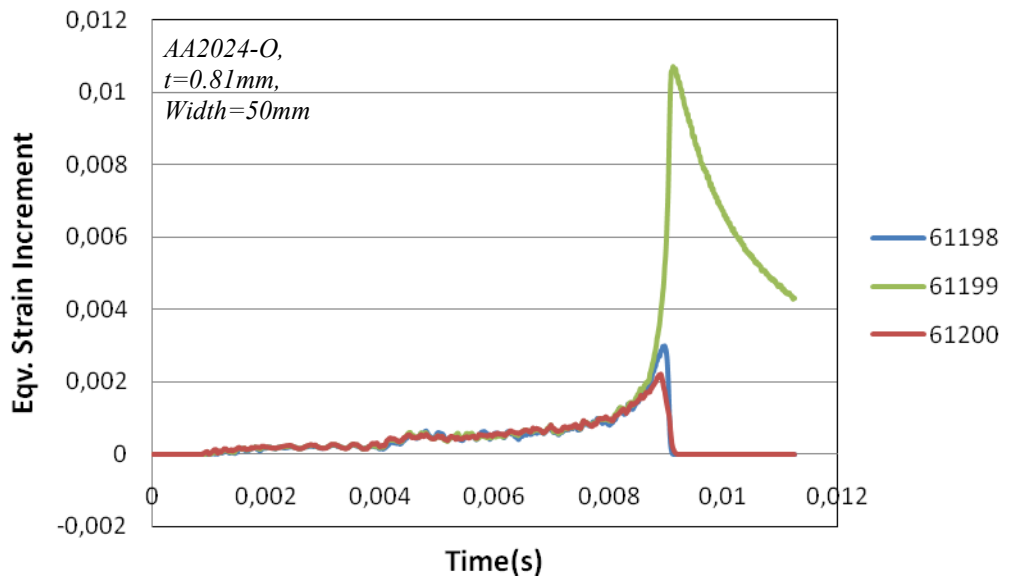


**Figure 6.44 Eqv. Strain Increments for the 1<sup>st</sup> Group Elements of W=50mm**

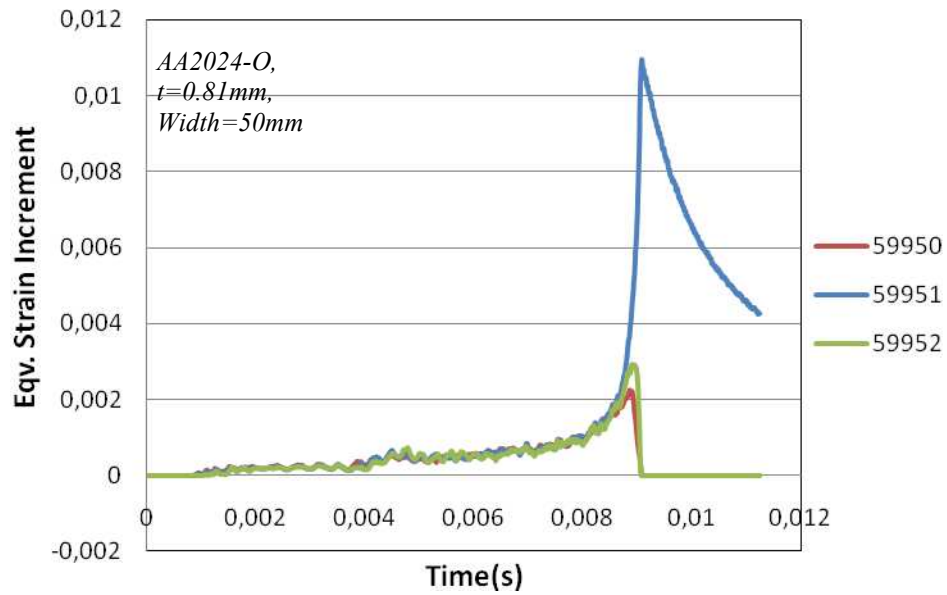


**Figure 6.45 Eqv. Strain Increments for the 2<sup>nd</sup> Group Elements of W=50mm**

As can be observed from Figure 6.44, at the beginning of the stretching period, the equivalent strains for all the elements are increasing because the equivalent strain increments are positive for the 1<sup>st</sup> group. But after  $t=0.0089\text{s}$ , the equivalent strain increments of the elements no.61200 and element no.61198 start decreasing. At  $t=0.0091\text{s}$ , the equivalent strain increment of the element no.61198 drops to zero. However, the equivalent strain increment of the element no.61199 is still positive and increasing. At zero equivalent strain increment instant, major and minor strains of the element no.61198 are recorded and it constitutes the 1<sup>st</sup> limit strain point for the specimen W=50mm for the construction of the FLD.

If Figure 6.45 is analyzed, at the beginning of the stretching period, the equivalent strains for all the elements are increasing because the equivalent strain increments are positive for the 2<sup>nd</sup> group. But after  $t=0.0079\text{s}$ , the equivalent strain increments of the elements no.59950 and element no.59952 start decreasing. At  $t=0.0091\text{s}$ , the strain increment of the element no.59952 reaches to zero. However, the equivalent strain increment of the element no.59951 is still positive and increasing. At zero equivalent strain increment instant, major and minor strains of the element no.59952 are recorded and it constitutes the 2<sup>nd</sup> limit strain point for the specimen W=50mm for the construction of the FLD.

### 6.2.3.3 Width=70mm

The deformed geometry of the sheet is shown in Figure 6.46. It can be observed that the necked elements are located at the wall of the blank (punch radius).

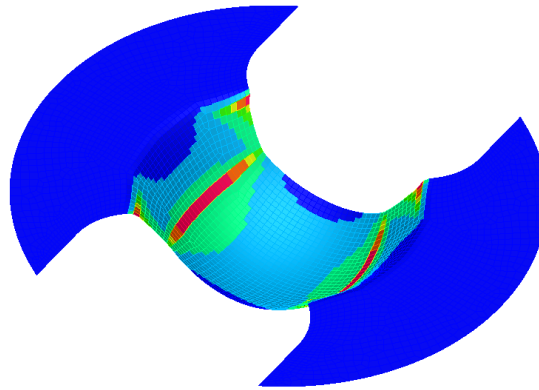


**Figure 6.46 Deformed Geometry of W=70mm**

The necking area of the specimen is shown in Figure 6.47. Totally six reference elements are analyzed in 2 groups which are, no.62339-no.62340-no.62341 and no.59949-no.59950-no.59951.

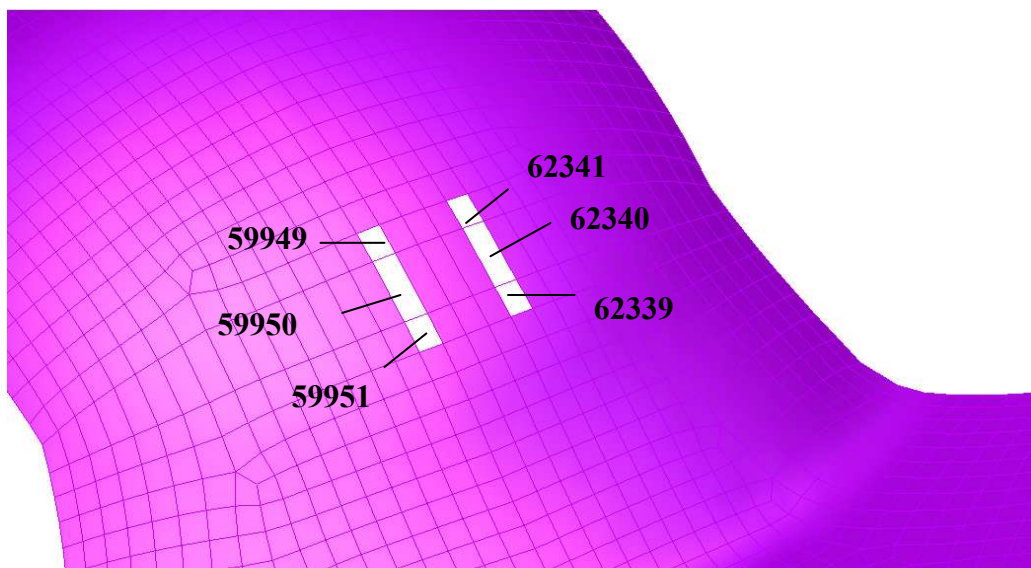


**Figure 6.47 Location of the Measuring Elements for W=70mm**

In Figures 6.48 and 6.49, equivalent strain increments of the 2 groups of elements are shown with respect to time.

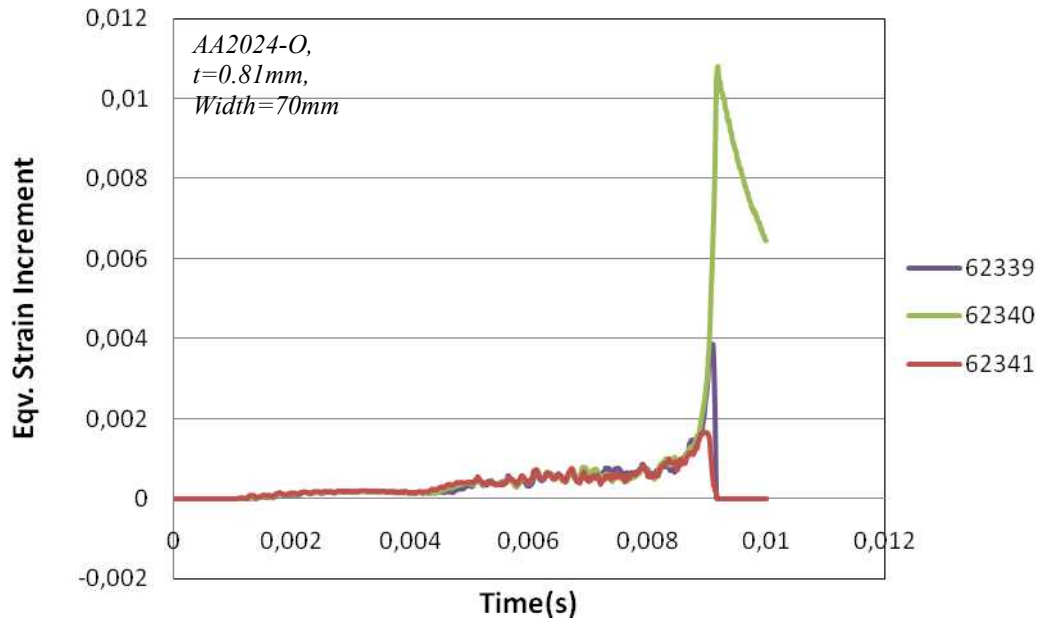


**Figure 6.48 Eqv. Strain Increments for the 1<sup>st</sup> Group Elements of W=70mm**

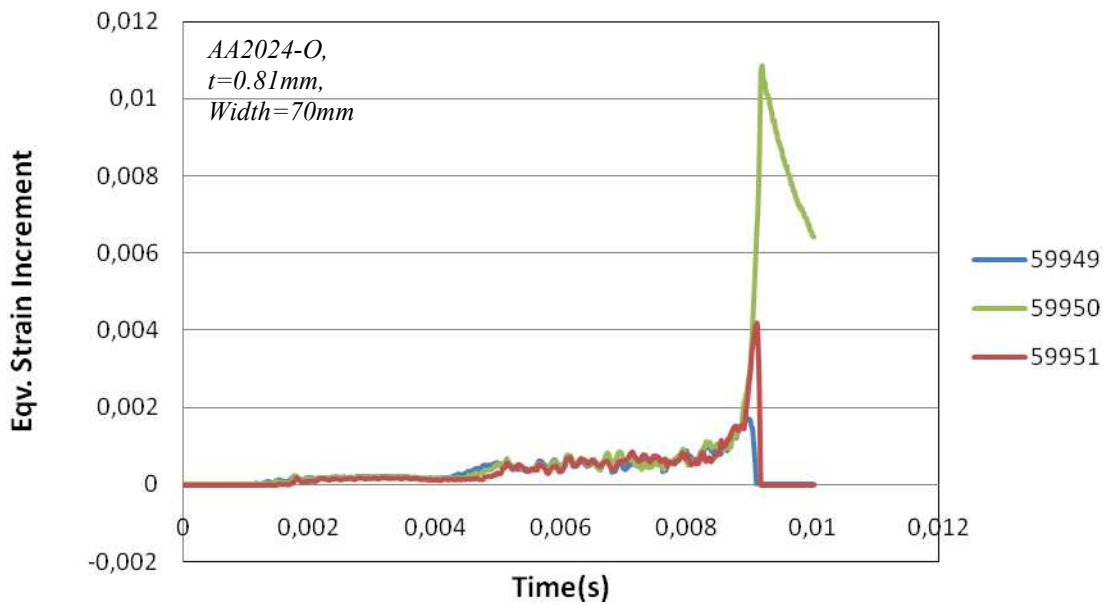


**Figure 6.49 Eqv. Strain Increments for the 2<sup>nd</sup> Group Elements of W=70mm**

As can be observed from Figure 6.48, at the beginning of the stretching period, the equivalent strains for all the elements are increasing because the equivalent strain increments are positive for the 1<sup>st</sup> group. But after  $t=0.0091s$ , both the equivalent strain increments of the element no.62339 and no.62341 start decreasing. At  $t=0.0092s$ , the strain increment of the element no.62339 reaches to zero first. However, the equivalent strain increment of the element no.62340 is still positive and increasing. At zero equivalent strain increment instant, major and minor strains of the element no.62339 are recorded and it constitutes the 1<sup>st</sup> limit strain point for the specimen  $W=70mm$  for the construction of the FLD.

If Figure 6.49 is analyzed, at the beginning of the stretching period the equivalent strains for all the elements are increasing because the equivalent strain increments are positive for the 2<sup>nd</sup> group. But after  $t=0.0089s$ , the equivalent strain increment of the element no.59949 starts decreasing. Then, the strain increment of the element no.59951 also starts decreasing at  $t= 0.0091s$ . At  $t= 0.0092s$ , the strain increment of the element no.59949 reaches to zero. However, the equivalent strain increment of the element no.59950 is still positive and increases. At zero equivalent strain increment instant, major and minor strains of the element no.59949 are recorded and it constitutes the 2<sup>nd</sup> limit strain point for the specimen  $W=70mm$  for the construction of the FLD.

#### **6.2.3.4 Width=90mm**

The deformed geometry of the sheet is shown in Figure 6.50. It can be observed that the elements located at the die radius are the necking elements.

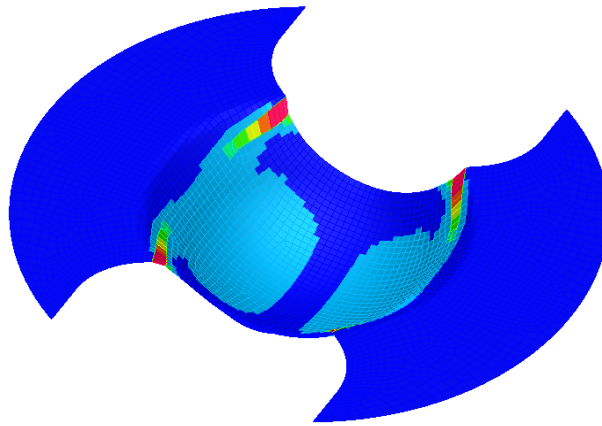


**Figure 6.50 Deformed Geometry of W=90mm**

For the specimen having 90mm width, the localization is observed on the elements near the die radius instead of along the punch radius for the cases W=30mm, W=50mm and W=70mm. This is an unexpected result and might be occurred because of the friction conditions of the process.

Since the necking elements are not obvious at the die radius and the strain values at the necking region are varied, no limit strain data points could be recorded using strain hardening phenomenon to construct the FLD for W=90mm specimen.

#### **6.2.3.5 Width=110mm**

The deformed geometry of the sheet is shown in Figure 6.51. It can be observed that the necked elements are located at the wall of the blank (punch radius).

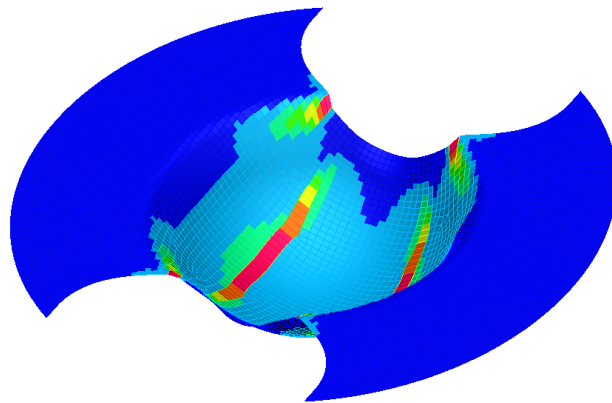


**Figure 6.51 Deformed Geometry of W=110mm**

The necking area of the specimen is shown in Figure 6.52. Totally six reference elements are analyzed in 2 groups which are, no.61565-no.61566-no.61567 and no.61079-no.61080-no.61081.

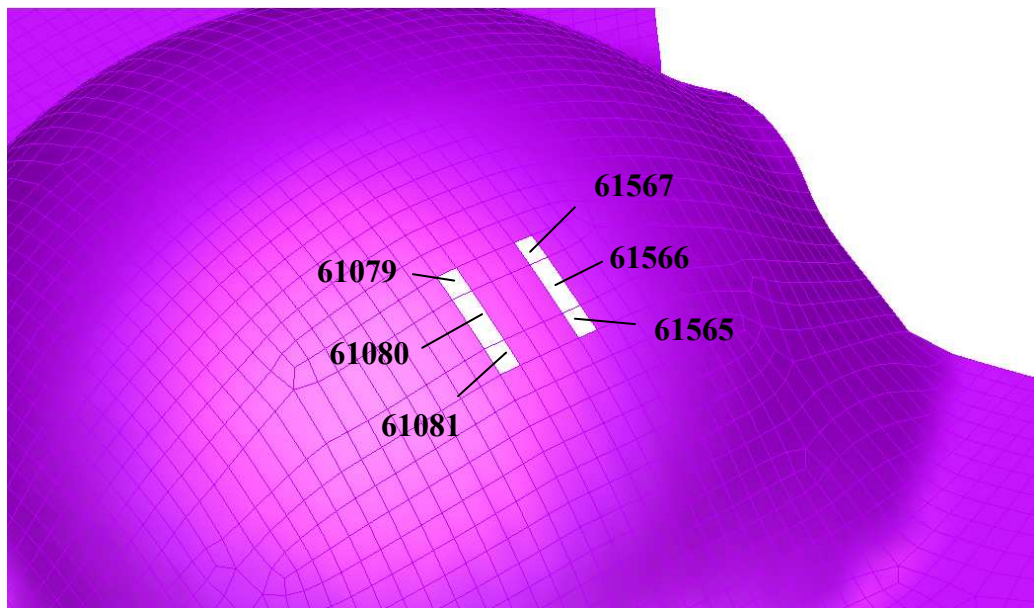


**Figure 6.52 Location of the Measuring Elements for W=110mm**

In Figures 6.53 and 6.54, equivalent strain increments of the 2 groups of elements are shown with respect to time.

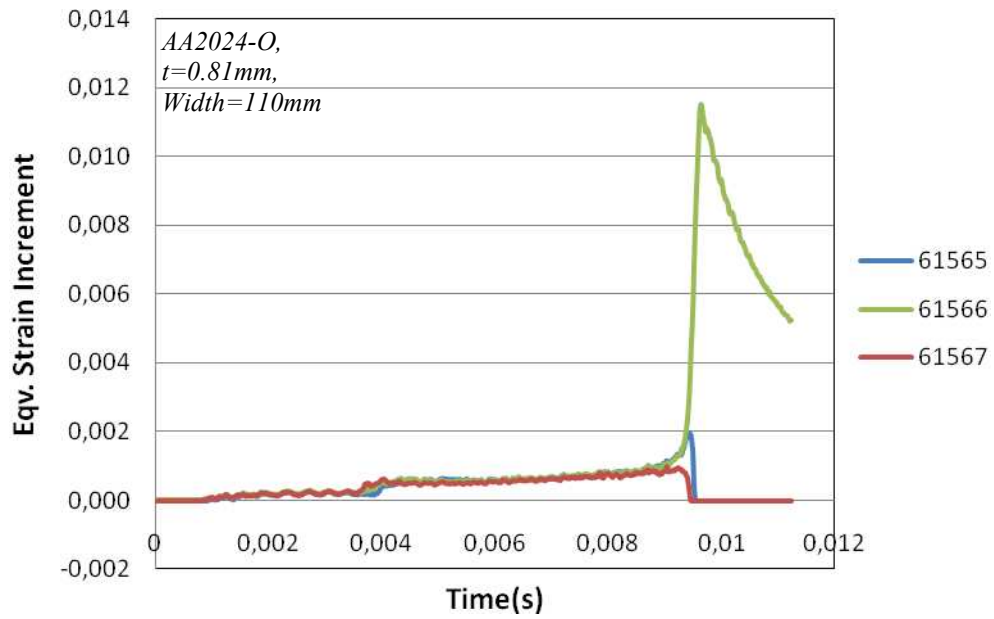


**Figure 6.53 Eqv. Strain Increments for the 1<sup>st</sup> Group Elements of W=110mm**

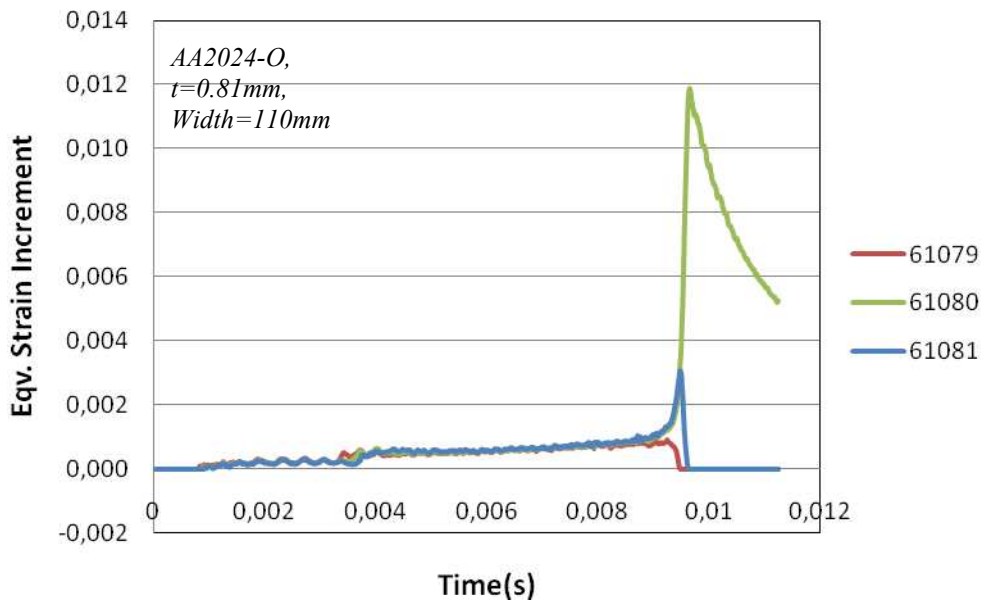


**Figure 6.54 Eqv. Strain Increments for the 2<sup>nd</sup> Group Elements of W=110mm**

As can be observed from Figure 6.53, at the beginning of the stretching period, the equivalent strains for all the elements are increasing because the equivalent strain increments are positive for the 1<sup>st</sup> group. But after  $t=0.0092s$ , the equivalent strain

increment of the element no.61567 starts decreasing. Then, strain increment of the element no.61565 starts decreasing at  $t= 0.0094s$ . At  $t=0.0095s$ , the strain increments of the element no.61567 reaches to zero. However, the equivalent strain increment of the element no.61566 is still positive and increasing. At zero equivalent strain increment instant, major and minor strains of the element no.61567 are recorded and it constitutes the 1<sup>st</sup> limit strain point for the specimen  $W=110mm$  for the construction of the FLD.

If Figure 6.54 is analyzed, at the beginning of the stretching the equivalent strains for all the elements are increasing because the equivalent strain increments are positive for the 2<sup>nd</sup> group. But after  $t=0.0087s$ , the equivalent strain increment of the element no.61079 starts decreasing. Then, strain increment of the element no.61081 also starts decreasing at  $t= 0.0094s$ . At  $t= 0.0094s$ , the equivalent strain increment of the element no.61079 reaches to zero. However, the equivalent strain increment of the element no.61080 is still positive and continues increasing. At zero equivalent strain increment instant, major and minor strains of the element no.61079 are recorded and it constitutes the 2<sup>nd</sup> limit strain point for the specimen  $W=110mm$  for the construction of the FLD.

### 6.2.3.6 Width=130mm

The deformed geometry of the sheet is shown below.

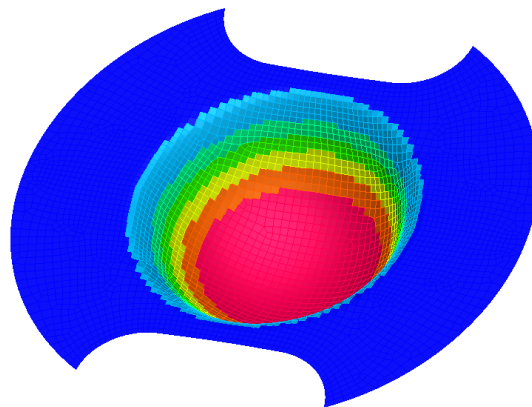


**Figure 6.55 Deformed Geometry of  $W=130mm$**

As seen from the Figure 6.55, a localized necking region cannot be seen for the specimen having a width 130mm. For the other specimens, the necked area could be clearly observed. It can be concluded that similar stretching behavior has taken place on the elements that are in contact with punch and therefore no special localized necking region is formed for  $W=130\text{mm}$ . The reason could be the material properties and especially the anisotropy ratio constants  $R_0$ ,  $R_{45}$  and  $R_{90}$  of the AA2024-O.

Since localized necking could not be achieved from the FE simulation, no limit strain data points are recorded using strain hardening phenomenon to construct the FLD for  $W=130\text{mm}$  specimen.

#### **6.2.3.7 Width=200mm**

This is the biaxial stretching state of the Nakazima test. The deformed geometry of the sheet is shown below in Figure 6.56.

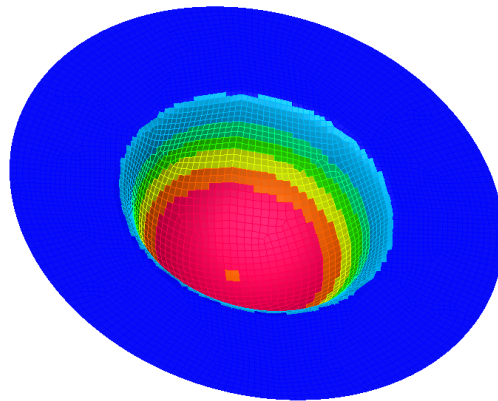


**Figure 6.56 Deformed Geometry of  $W=200\text{mm}$**

As seen from the Figure 6.56, a localized necking region cannot be seen for the specimen having a width 200mm such as the specimen with width 130mm. For the other specimens, the necked area could be clearly observed. It can be concluded that similar stretching behavior has taken place on the elements that are in contact with punch and therefore no special localized necking region is formed for  $W=200\text{mm}$ .

Since localized necking could not be achieved from the FE simulation, no limit strain data points are recorded using strain hardening phenomenon to construct the FLD for W=200mm specimen.

#### **6.2.4 Finite Element Predicted FLD**

From the above simulations, 14 limit strain reference points from uniaxial tension to biaxial tension states are recorded for the material SAE 1006. However, for the material AA2024-O 8 limit strain reference points could be obtained. Based on these reference points, the FLD of the SAE 1006 and AA2024-O has been predicted. The FLC is obtained by plotting a curve to these reference points for SAE 1006 and AA2024-O. The obtained FLDs are shown and compared with the experimental and theoretical results in Chapter 7.

# CHAPTER 7

## DISCUSSION OF RESULTS

### 7.1 Predicted Forming Limit Curves

In this section, all the predicted forming limit curves using theoretical and numerical procedures that are mentioned so far are presented.

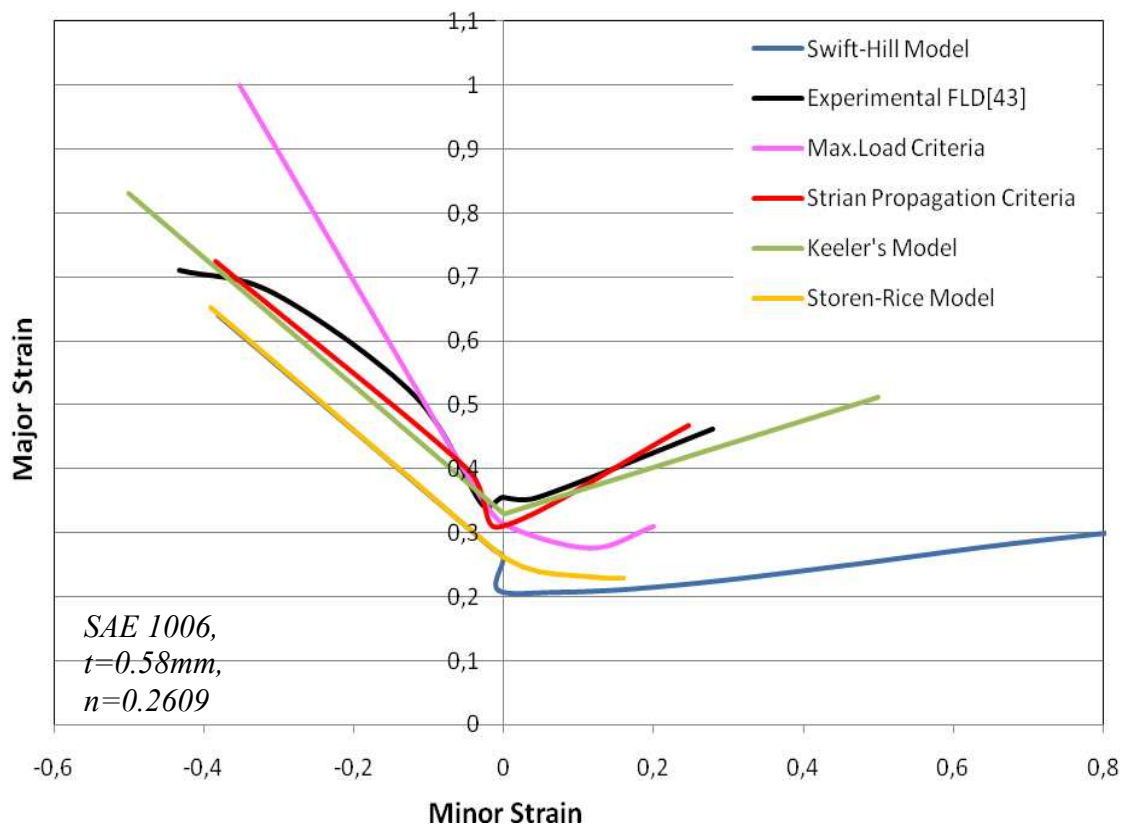


Figure 7.1 Predicted FLC's of SAE 1006

In Figure 7.1, the predicted forming limit curves for the material SAE 1006 are shown. The simple empirical Keeler's model gives very good prediction especially for the right hand side of the FLD for SAE 1006. Although, the empirical formula is only depend on the material thickness and the strain hardening coefficient, the result is remarkably good.

The prediction by the Swift-Hill model based on the Hollomon's hardening equation underestimates the forming limits when compared to the experimental curve for SAE 1006. On the left hand side, the discrepancy is lower but on the right hand side it is substantially high such that nearly the Swift-Hill curve predicts half of the major limit strains of the experimental curve.

Storen-Rice model also do not display a good agreement with the experimental results. Generally, FLC shows increasing trend when passing from negative minor strain region to the positive minor strain region, in other words after passing plain strain state. However, the forming curve of Storen-Rice model continues decreasing after passing plain strain condition and the right hand side of the FLD is coincident with the Swift-Hill curve and underestimates the forming limits.

The FLC predicted for the maximum load criteria, show similar behavior with the experimental curve near the plain strain state. From uniaxial tension to plain strain state, the major strain decreases very sharply. This is because of the limit strains obtained for the specimen with  $R=65\text{mm}$ . The major limit strain obtained for  $R=65\text{mm}$  is 0.999 and for  $R=50\text{mm}$  0.375. Therefore, a rapid decrease on the left hand side of the FLD is obtained. In addition, the limit strain points for  $R=75$  is not included to the curve, because very high limit strains are obtained for  $R=75\text{mm}$ . Finally, no limit strains has been found for the uniaxial tension state at  $R=85\text{mm}$  because no load maximum has been achieved as shown in Figure 7.20.

The FLC predicted by strain propagation criteria can be stated as the best prediction through all of the FLCs. As seen in Figure 7.1, the right hand side of the FLD is nearly coincident with the experimental curve. At the left hand side, as moving from

plain strain state to uniaxial tension state, predicted FLC approaches to the experimentally obtained FLC and shows very similar trend in general. One can conclude that applying strain propagation criteria to the FE simulation may give very accurate results for the materials having similar properties with SAE 1006.

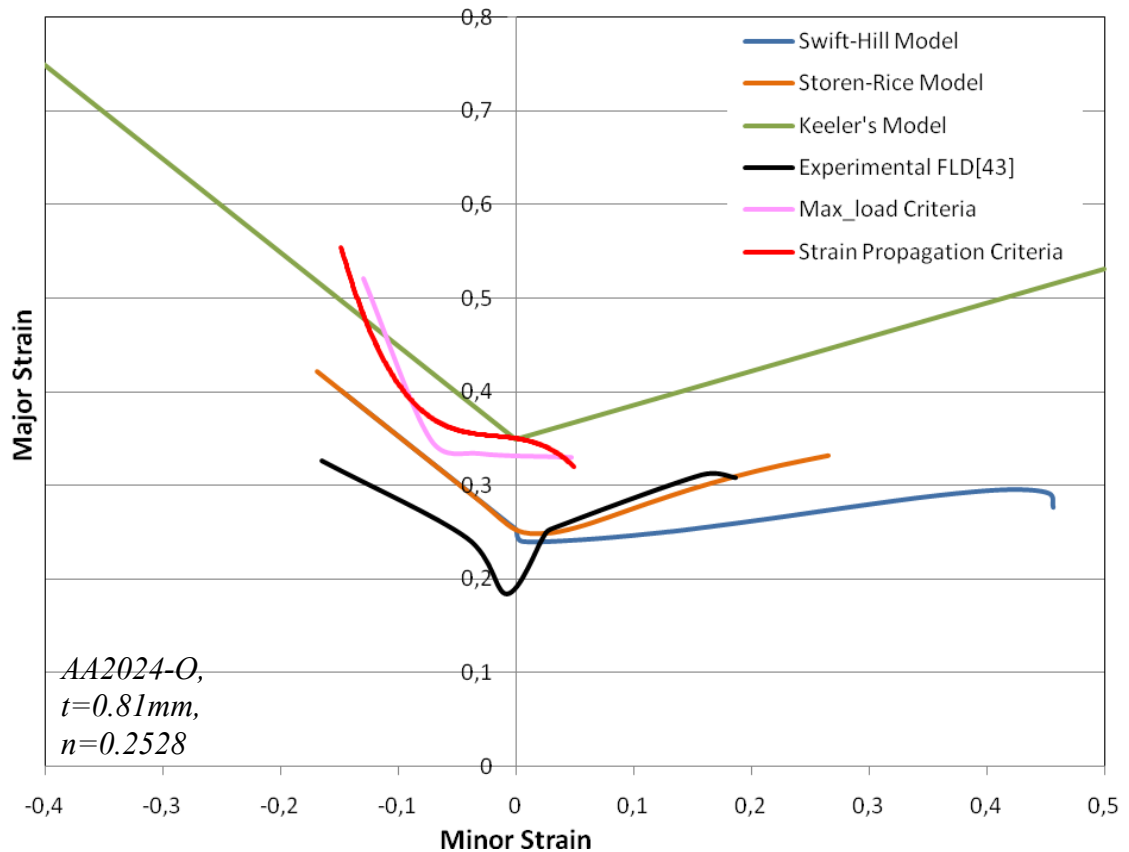


**Figure 7.2 Predicted FLC's of AA2024-O**

If the predicted forming limit curves for the material AA2024-O are analyzed, it can be concluded that all of the prediction methods overestimates the forming limits as shown in Figure 7.2.

The Keeler's model nearly predicts twice of the major limit strains of the experimental curve. For SAE 1006, good agreement has been obtained; however for AA2024-O it overestimates the forming limits and cannot be used as a trusted prediction method.

The prediction by the Swift-Hill model based on the Hollomon's hardening equation also overestimates the forming limits when compared to the experimental curve for AA2024-O. However, the obtained FLD is closer to the experiment curve when compared with Keeler's model. On the right hand side, two curves intersect when the major strain is approximately equal to 0.23 and after the intersection point Swift-Hill curve lies under the experimental curve. Therefore, one may conclude that Swift-Hill prediction underestimates the forming limits on the left hand side; however it overestimates on the left hand side.

If the Storen-Rice model is analyzed, it can be seen that the predicted FLD is very similar to the Swift-Hill prediction. The obtained FLC also predicts high forming limits on the left hand side and is coincident with Swift-Hill model prediction. However, it is very close to the experimental curve on the right hand side. For SAE 1006, after plain strain state the curve continued decreasing, however this not the case for AA2024-O. The major strain increases at the stretching region.

The FLC predicted for the maximum load criteria, show also over predicted forming limits when compared with the experimental curve. For AA2024-O, no prediction has been done for the specimens with width 90mm, 130mm and 200mm since necking is not observed. Necking has only observed only for specimens having width 30mm, 50mm, 70mm and 110mm and the maximum load curves are shown section 7.5. For  $W=110\text{mm}$  and  $W=70\text{mm}$  specimens, nearly same major limit strains are obtained, therefore the FLC is parallel to minor strain axis between these points. An increase is also observed when approaching to uniaxial tension state on the left hand side of the FLD. For, all of the regions maximum load criteria overestimates the forming limits of the AA2024-O, therefore no satisfactory results are obtained.

The FLC predicted by strain propagation criteria cannot predict the forming limits of AA2024-O well as the other theoretical approaches. As for FLD of the maximum load criteria, only from 4 specimens the limit strain values are recorded. For both left and right hand sides of the FLD, the forming limits are overestimated and satisfactory results cannot be obtained. Applying strain propagation criteria to the FE

simulation may not give very accurate results for the materials having similar properties with AA2024-O.

## 7.2 Limit Strains of the Strain Propagation Analysis for SAE 1006

In Section 6.2.2, the equivalent strain increments of the measuring elements for SAE 1006 are determined. Below in Figures (7.3)-(7.9), the principal limit strain histories of the reference elements are displayed for 7 specimen geometries of SAE 1006. In these figures, after the occurrence of localized necking, no further increase observed at the major and minor strain of the referenced necked elements. This shows that strain transfer can no longer be achieved between the elements.

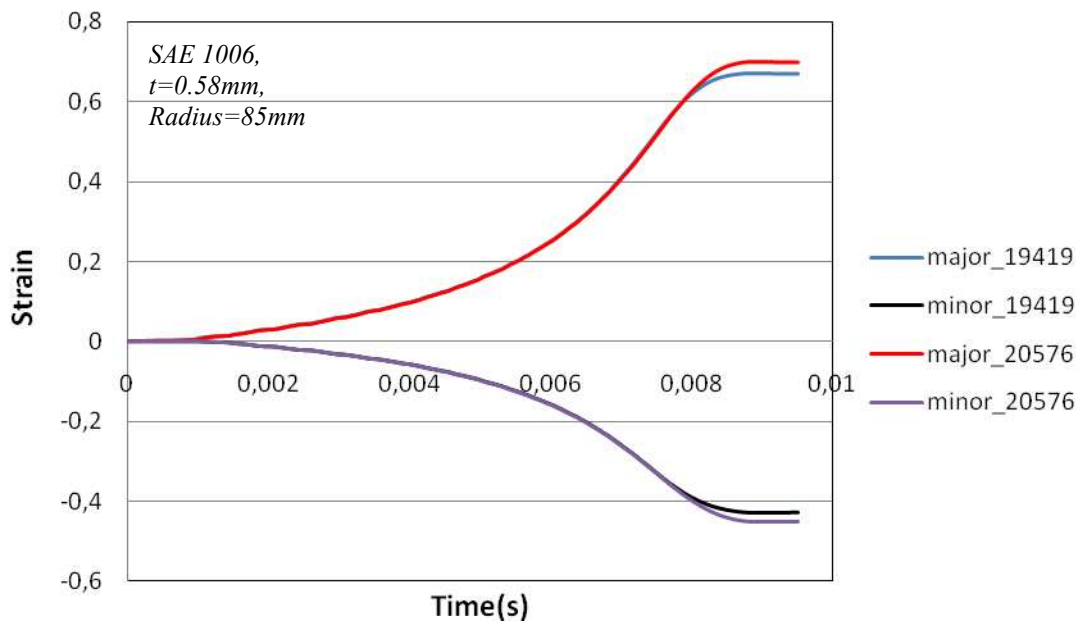
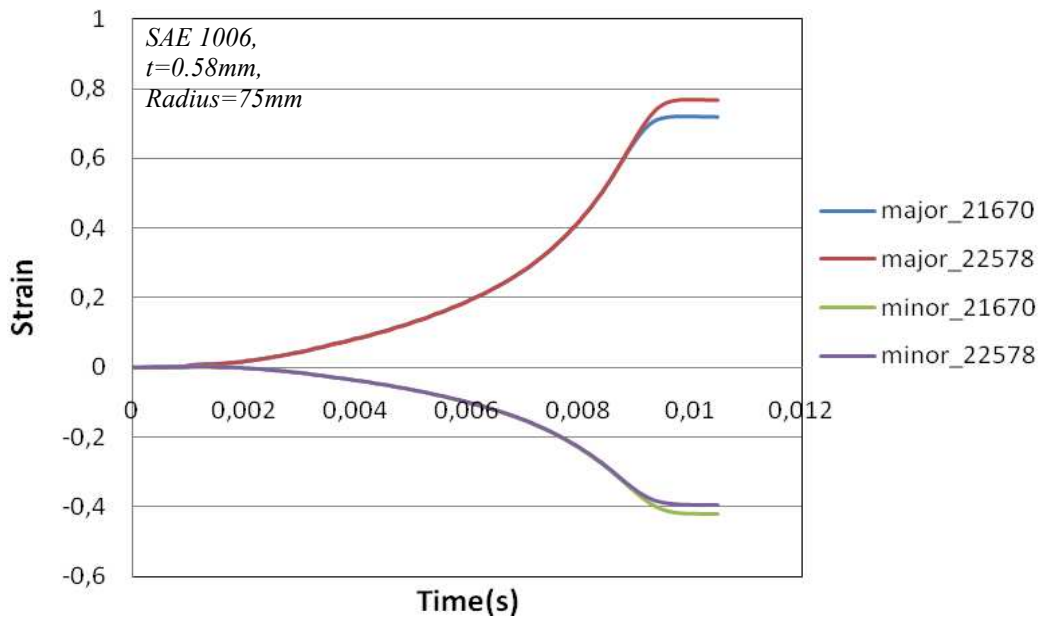
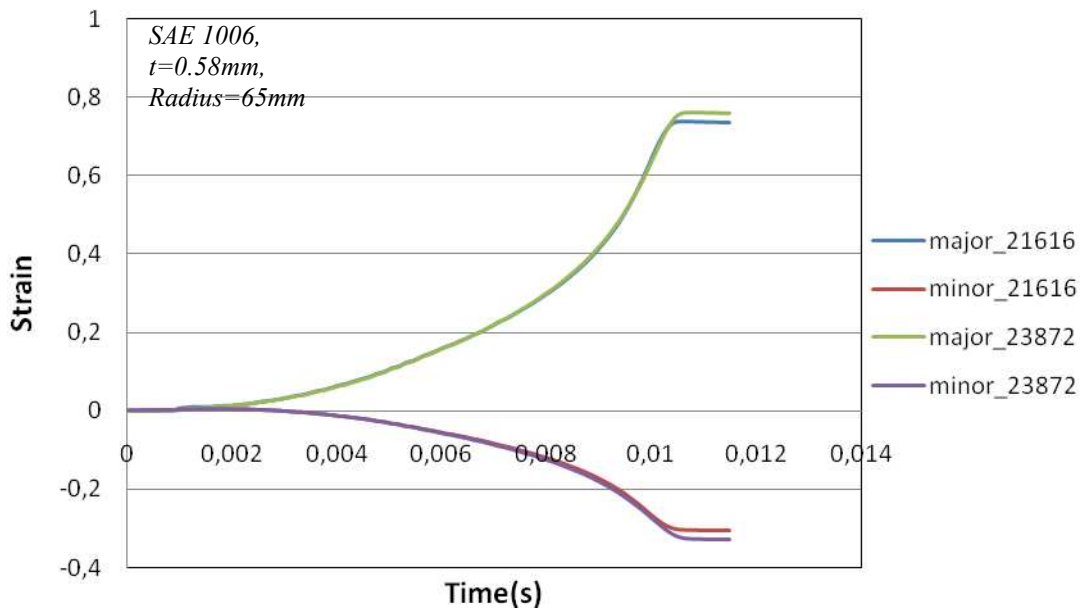


Figure 7.3 Minor and Major Strains of the Reference Elements for R=85mm



**Figure 7.4 Minor and Major Strains of the Reference Elements for R=75mm**



**Figure 7.5 Minor and Major Strains of the Reference Elements for R=65mm**

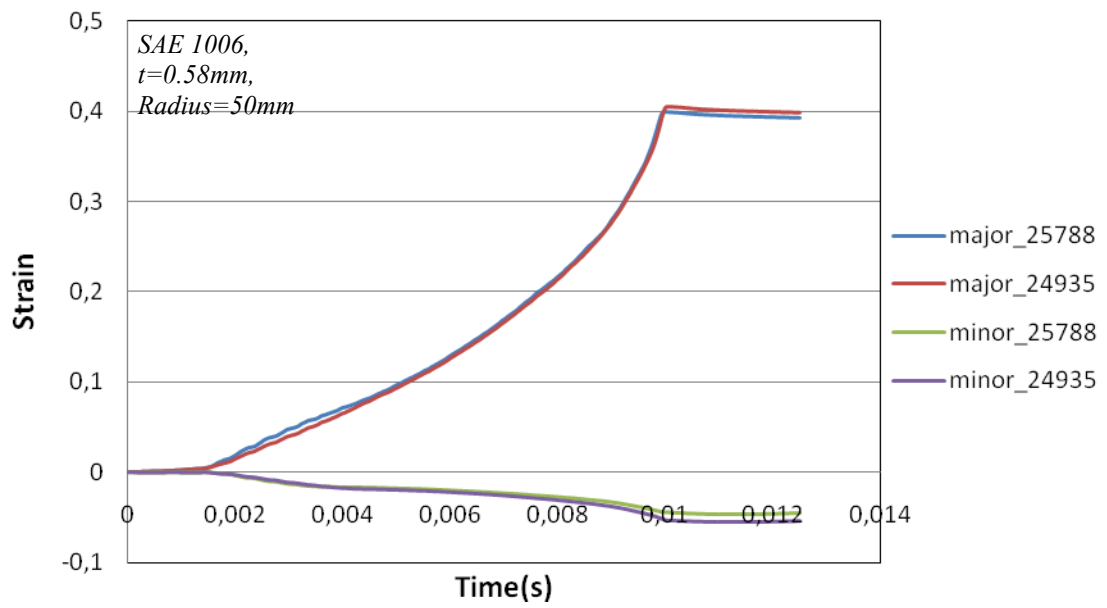


**Figure 7.6 Minor and Major Strains of the Reference Elements for R=50mm**

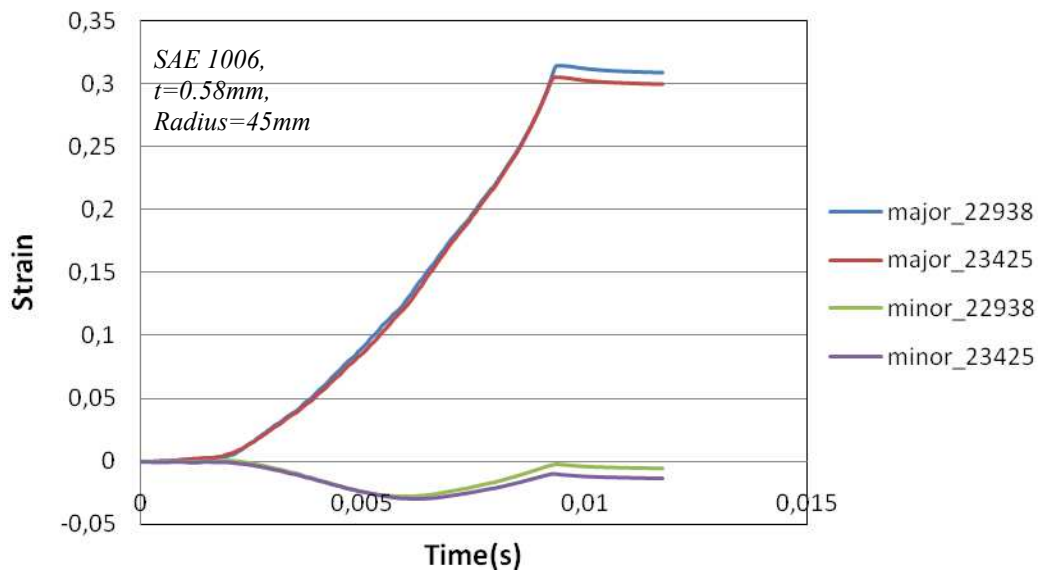


**Figure 7.7 Minor and Major Strains of the Reference Elements for R=45mm**

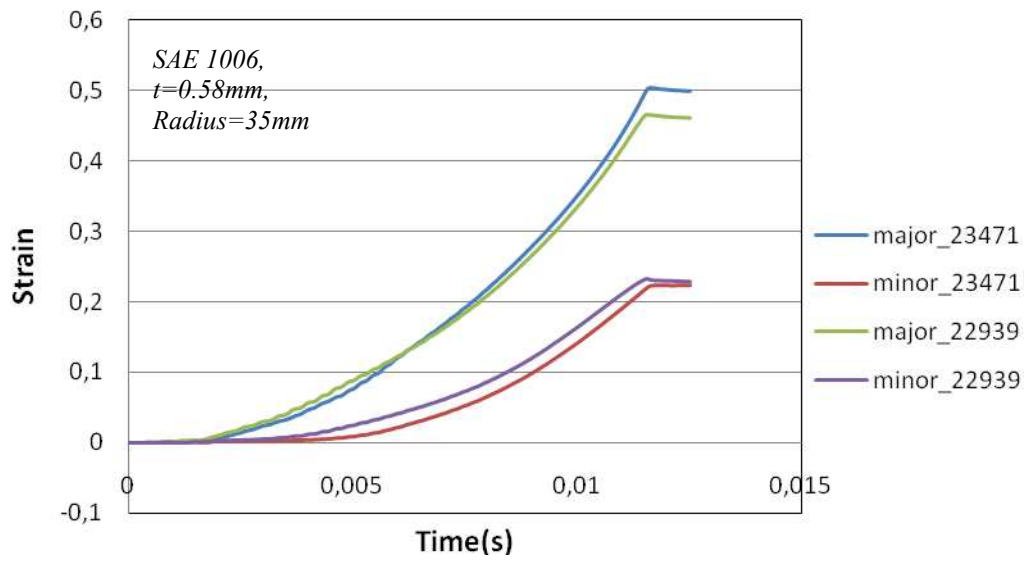


**Figure 7.8 Minor and Major Strains of the Reference Elements for R=35mm**

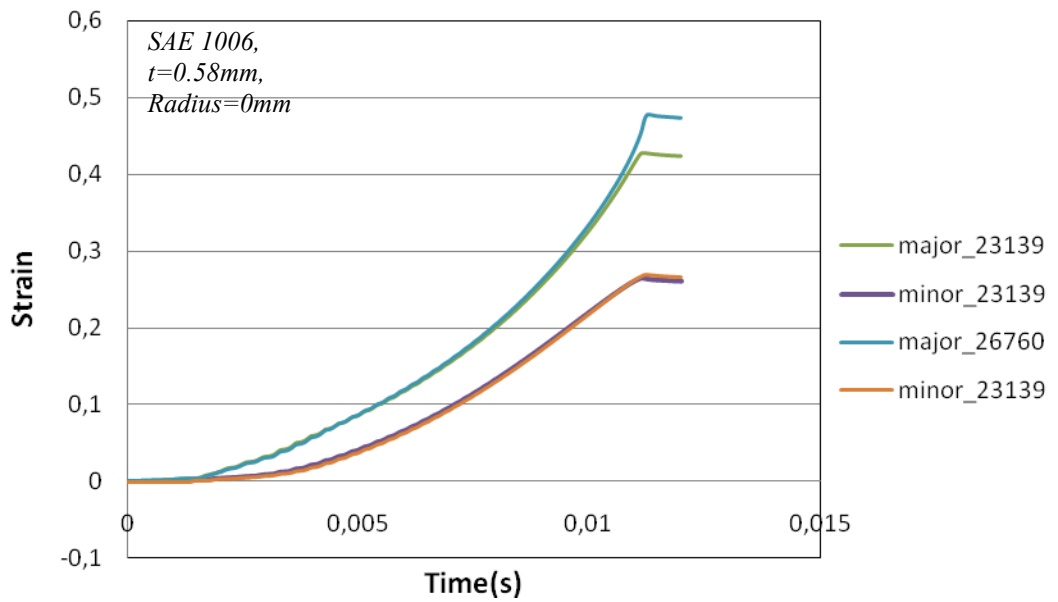


**Figure 7.9 Minor and Major Strains of the Reference Elements for R=0mm**

### 7.3 Limit Strains of the Strain Propagation Analysis for AA2024-O

In Chapter 6.2.3, the equivalent strain increments of the measuring elements AA2024-O are determined. Below in Figures (7.10)-(7.13), the principal limit strain histories of the reference elements are displayed for 4 specimen geometries of AA2024-O. In these figures, after the occurrence of localized necking, no further increase observed at the major and minor strain of the referenced necked elements. This shows that strain transfer can no longer be achieved between the elements.

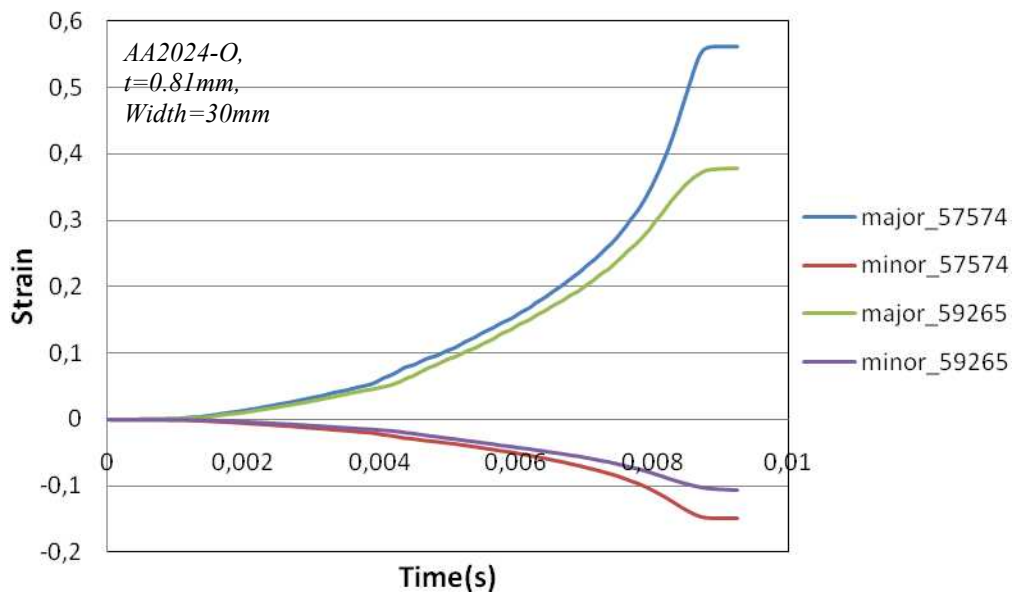


**Figure 7.10 Minor and Major Strains of the Reference Elements for W=30mm**

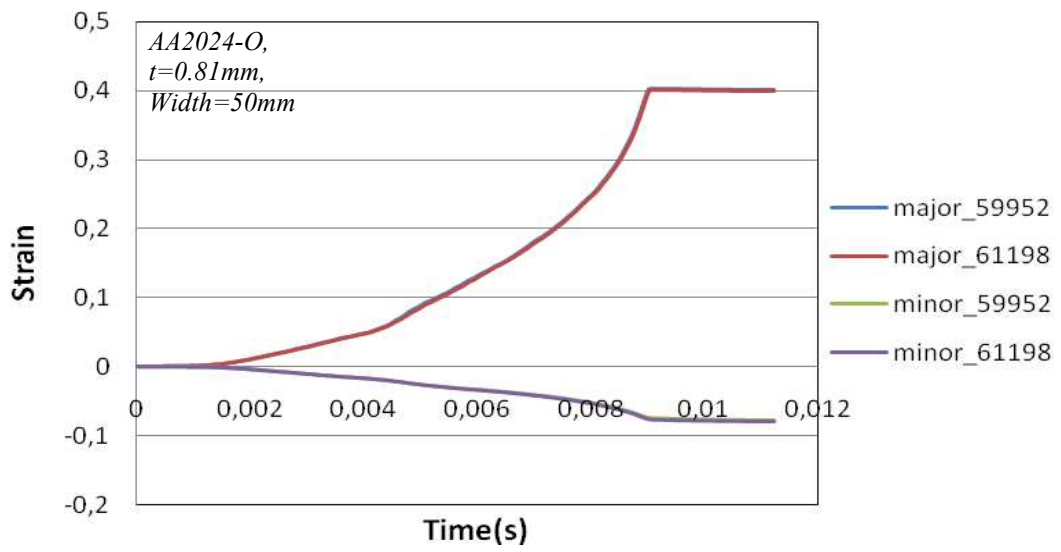


**Figure 7.11 Minor and Major Strains of the Reference Elements for W=50mm**

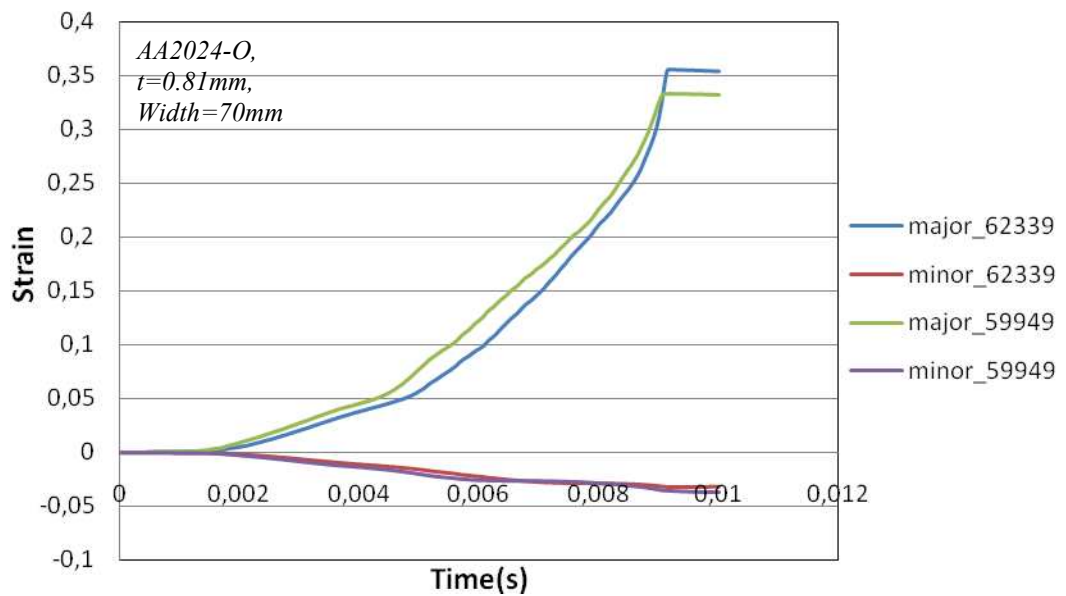


**Figure 7.12 Minor and Major Strains of the Reference Elements for W=70mm**

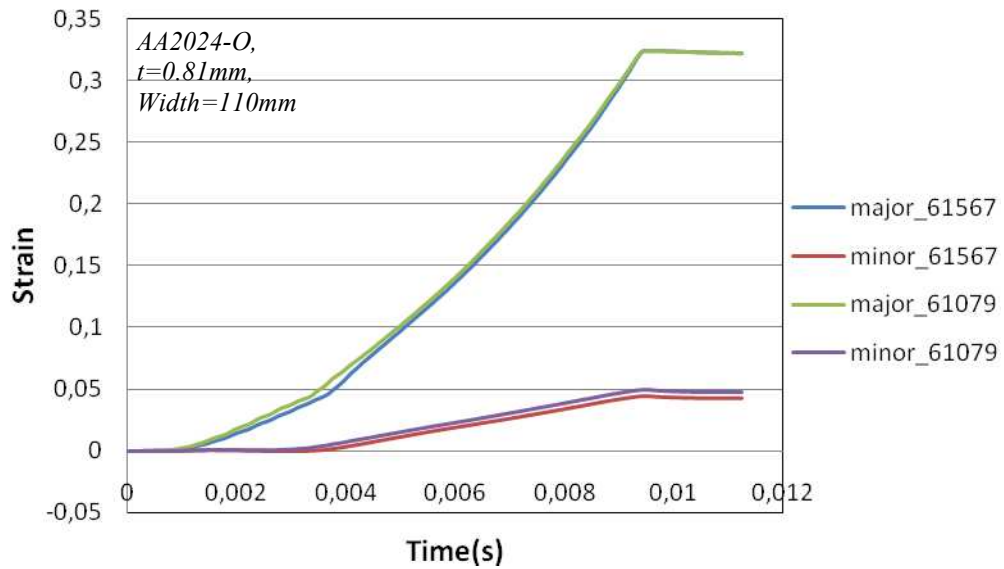


**Figure 7.13 Minor and Major Strains of the Reference Elements for W=110mm**

#### 7.4 Results of Maximum Load Criteria for SAE 1006

In this section, punch load vs. progression plots of 7 specimens for SAE 1006 is presented and the maximum points of the critical elements are shown. The reference necked elements have chosen as the most thinned element through the necking region of the deformed specimen which is generally located on the x-axis in the simulations. The obtained FLC using maximum load criteria is shown in section 7.1 with the experimental and all the other predicted FLCs.

##### 7.4.1 Radius=0mm

For biaxial stretching case, the element load vs. progression graph is shown in Figure 7.14. The critical reference element chosen is the element no.23140 as shown in Figure 6.33.

As can be seen from the Figure 7.14, the load reaches the maximum and necking takes place at 38.5mm punch depth and then there is a sharp decrease after 42mm. To

find the limit strains by applying maximum load condition, the major and minor strains of the measuring element, at 38.5mm punch depth are recorded.

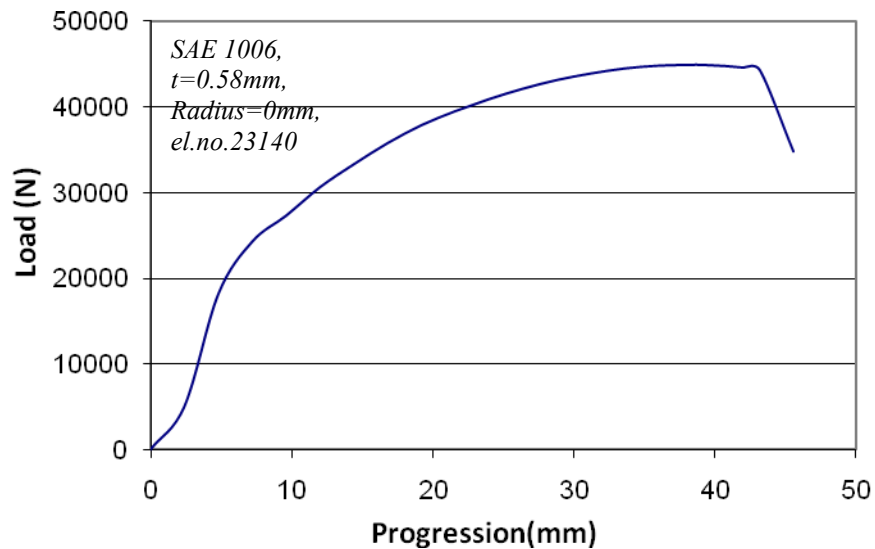


**Figure 7.14 Load vs. Punch Progression of Specimen R=0mm**

#### **7.4.2 Radius=35mm**

For the specimen R=35mm, the element load vs. progression graph is shown in Figure 7.15. The critical reference element chosen is the element no.22940 as shown in Figure 6.29.

As can be seen from the Figure 7.15, the load reaches the maximum and necking takes place at 36 mm punch depth and then the load decreases after that point. To find the limit strains by applying maximum load condition, the major and minor strains of the measuring element, at 36 mm punch depth are recorded.

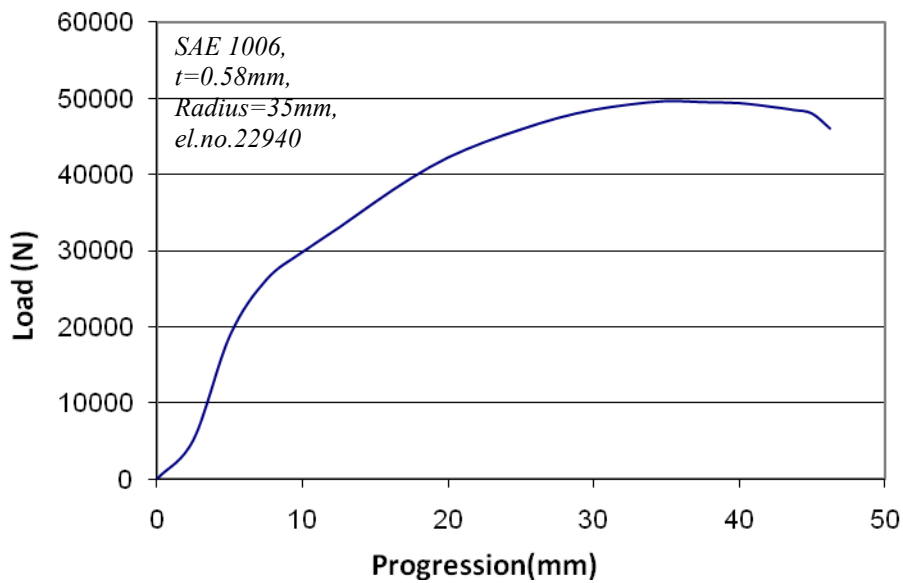


**Figure 7.15 Load vs. Punch Progression of Specimen R=35mm**

### 7.4.3 Radius=45mm

For the specimen R=45mm, the element load vs. progression graph is shown in Figure 7.16. The critical reference element chosen is the element no.22939 as shown in Figure 6.25.

As can be seen from the Figure 7.16, the load reaches the maximum and necking takes place at 37 mm punch depth and then the load start decreasing after that point. To find the limit strains by applying maximum load condition, the major and minor strains of the measuring element, at 37 mm punch depth are recorded.

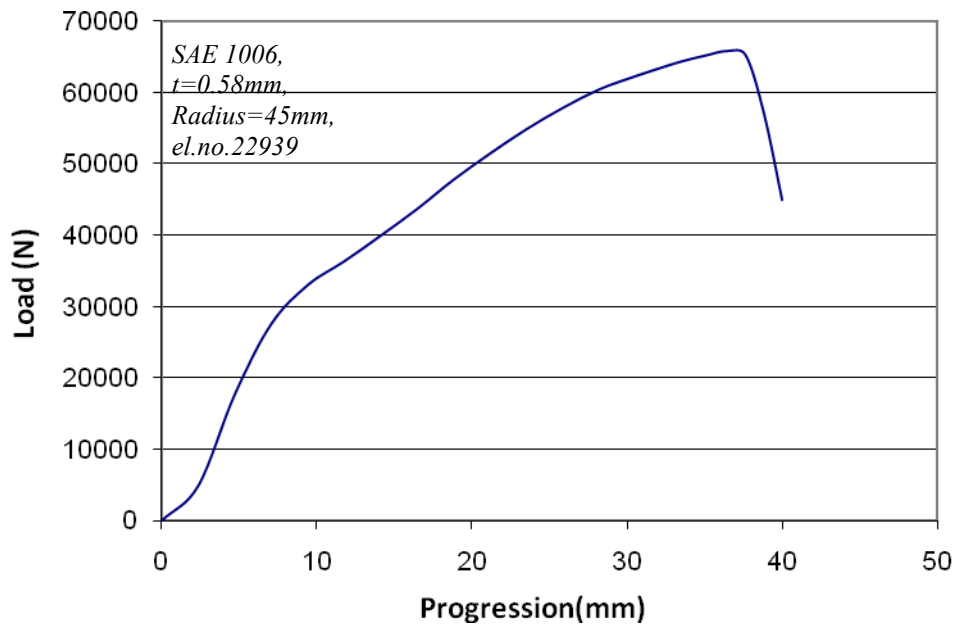


**Figure 7.16 Load vs. Punch Progression of Specimen R=45mm**

#### **7.4.4 Radius=50mm**

For the specimen R=50mm, the element load vs. progression graph is shown in Figure 7.17. The critical reference element chosen is the element no.25789 as shown in Figure 6.21.

As can be seen from the Figure 7.17, the load reaches the maximum and necking takes place at 39 mm punch depth and then the load start decreasing after that point. To find the limit strains by applying maximum load condition, the major and minor strains of the measuring element, at 39 mm punch depth are recorded.

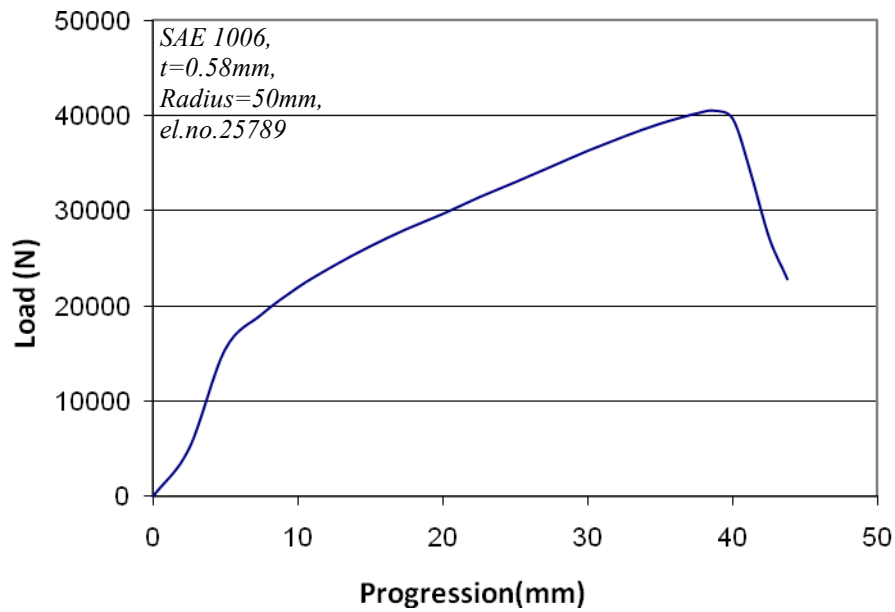


**Figure 7.17 Load vs. Punch Progression of Specimen R=50mm**

#### **7.4.5 Radius=65mm**

For the specimen R=65mm, the element load vs. progression graph is shown in Figure 7.18. The critical reference element chosen is the element no.21615 as shown in Figure 6.17.

As can be seen from the Figure 7.18, the load reaches the maximum and necking takes place at 42.5 mm punch depth and then the load start decreasing after that point. To find the limit strains by applying maximum load condition, the major and minor strains of the measuring element, at 42.5 mm punch depth are recorded. However at 42.5 mm punch depth the major and minor strains of element no.21615 are so high and not reasonable. The obtained major strain is 0.999 and the minor strain is -0.352. Therefore, these strains are not included in constructing the FLD.

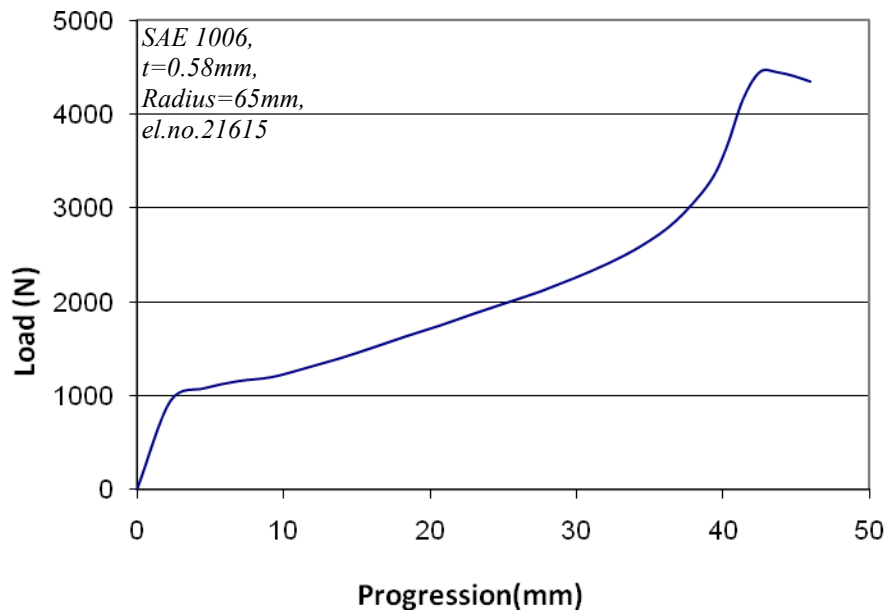


**Figure 7.18 Load vs. Punch Progression of Specimen R=65mm**

#### **7.4.6 Radius=75mm**

For the specimen R=75mm, the element load vs. progression graph is shown in Figure 7.19. The critical reference element chosen is the element no.21603 as shown in Figure 6.13.

As can be seen from the Figure 7.19, the load reaches the maximum and necking takes place at 39.9 mm punch depth and then the load start decreasing after that point. To find the limit strains by applying maximum load condition, the major and minor strains of the measuring element, at 39.9 mm punch depth are recorded. However at 39.9 mm punch depth the major and minor strains of element no.21603 are so high and not reasonable. The obtained major strain is 1.24 and the minor strain is -0.518. Therefore, these strains are not included in constructing the FLD.

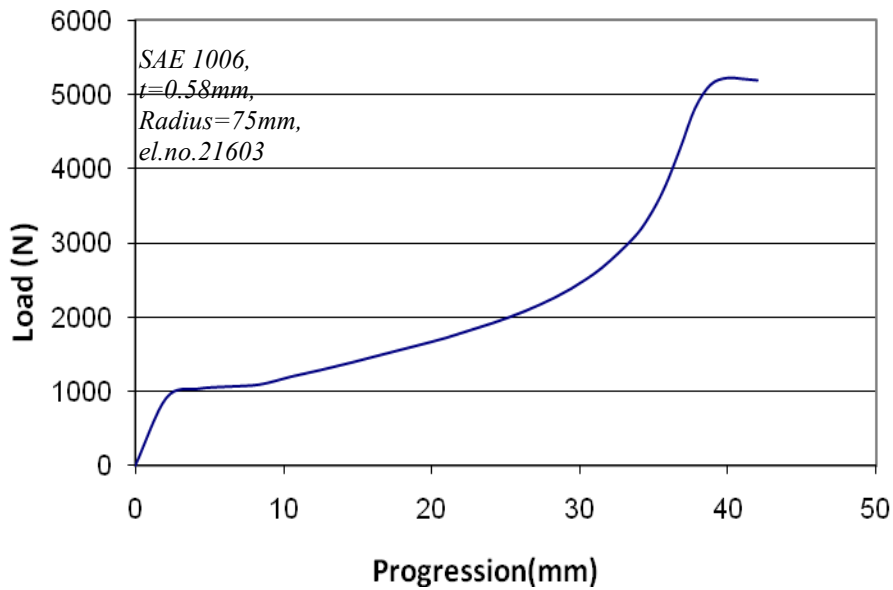


**Figure 7.19 Load vs. Punch Progression of Specimen R=75mm**

#### 7.4.7 Radius=85mm

For the specimen R=85mm, the element load vs. progression graph is shown in Figure 7.20. The critical reference element chosen is the element no.19361 as shown in Figure 6.9.

As can be seen from the Figure 7.20, the load curve continues increasing up to 38mm punch depth but peak is not observed. Since the load does not reach to a maximum point, one can conclude that maximum load criterion does not give a valid result for the specimen R=85mm and no data point for constructing the FLD is obtained.

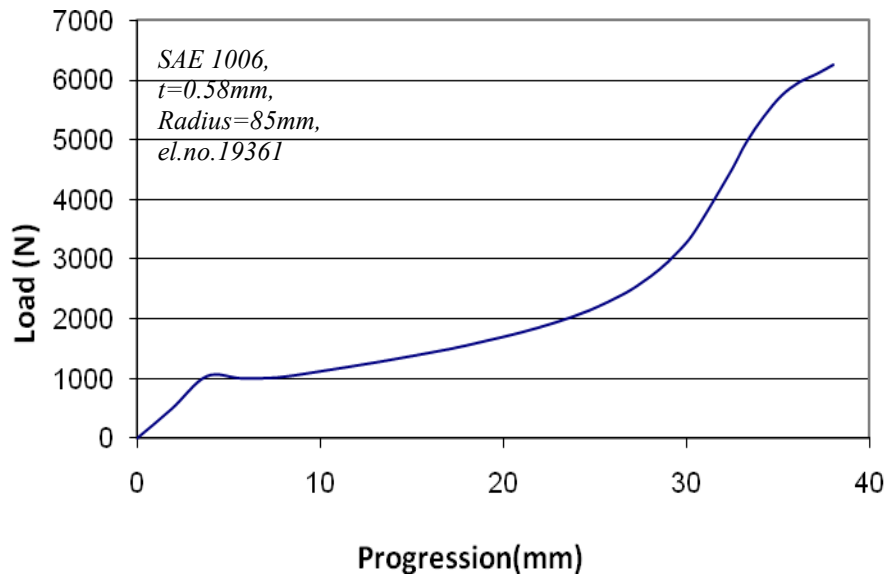


**Figure 7.20 Load vs. Punch Progression of Specimen R=85mm**

### 7.5 Results of Maximum Load Criteria for AA2024-O

In this section, punch load vs. progression plots of each specimen for AA2024-O is presented and the maximum points of the critical elements are shown as done in previous section. The reference necked elements have chosen as the most thinned element through the necking region of the deformed specimen which is generally located on the x-axis in the simulations. The obtained FLD using maximum load criteria is shown in section 7.1 with the experimental and all the other predicted FLDs.

#### 7.5.1 Width=30mm

For the specimen W=30mm, the element load vs. progression graph is shown in Figure 7.21. The critical reference element chosen is the element no.57573 as shown in Figure 6.39.

As can be seen from the Figure 7.21, the load reaches the maximum and necking takes place at 34.5 mm punch depth and then the load starts decreasing after that

point. To find the limit strains by applying maximum load condition, the major and minor strains of the measuring element, at 34.5 mm punch depth are recorded.

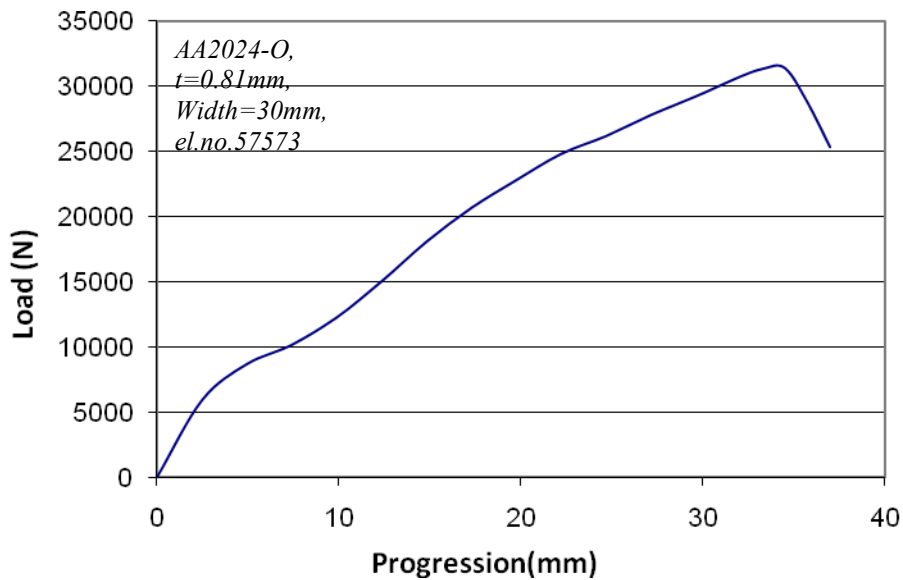


**Figure 7.21 Load vs. Punch Progression of Specimen W=30mm**

### 7.5.2 Width=50mm

For the specimen W=50mm, the element load vs. progression graph is shown in Figure 7.22. The critical reference element chosen is the element no.59951 as shown in Figure 6.43.

As can be seen from the Figure 7.22, the load reaches the maximum and necking takes place at 34.8 mm punch depth and then the load starts decreasing after that point. To find the limit strains by applying maximum load condition, the major and minor strains of the measuring element, at 34.8 mm punch depth are recorded.

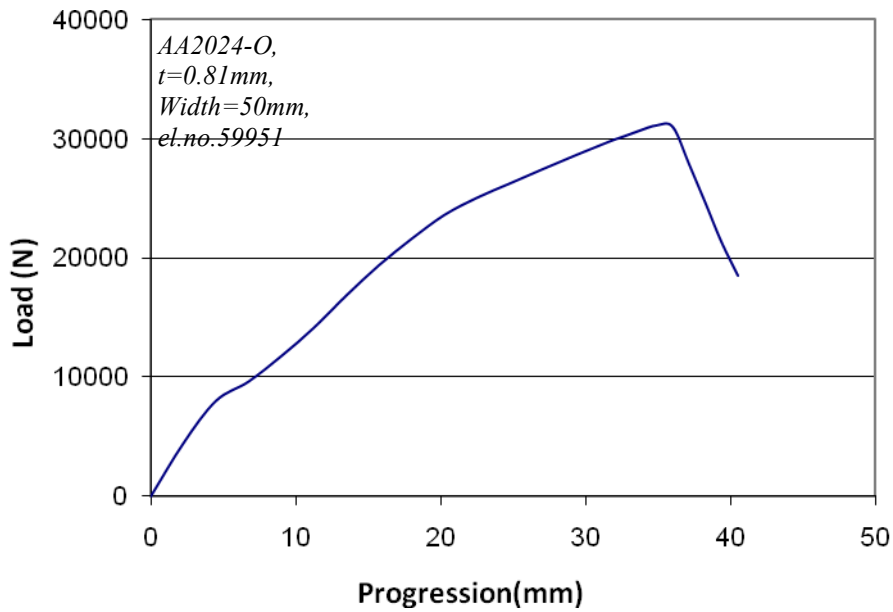


**Figure 7.22 Load vs. Punch Progression of Specimen W=50mm**

### 7.5.3 Width=70mm

For the specimen W=70mm, the element load vs. progression graph is shown in Figure 7.23. The critical reference element chosen is the element no.59950 as shown in Figure 6.47.

As can be seen from the Figure 7.23, the load reaches the maximum and necking takes place at 36 mm punch depth and then the load starts decreasing after that point. To find the limit strains by applying maximum load condition, the major and minor strains of the measuring element, at 36 mm punch depth are recorded.

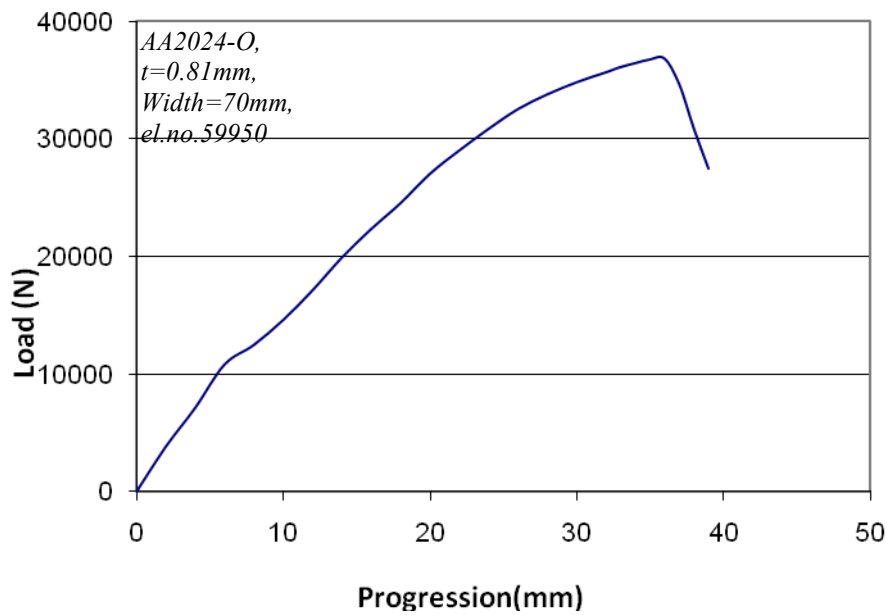


**Figure 7.23 Load vs. Punch Progression of Specimen W=70mm**

#### **7.5.4 Width=110mm**

For the specimen W=110mm, the element load vs. progression graph is shown in Figure 7.24. The critical reference element chosen is the element no.61080 as shown in Figure 6.52.

As can be seen from the Figure 7.24, the load reaches the maximum and necking takes place at 39 mm punch depth and then the load starts decreasing after that point. To find the limit strains by applying maximum load condition, the major and minor strains of the measuring element, at 39 mm punch depth are recorded.

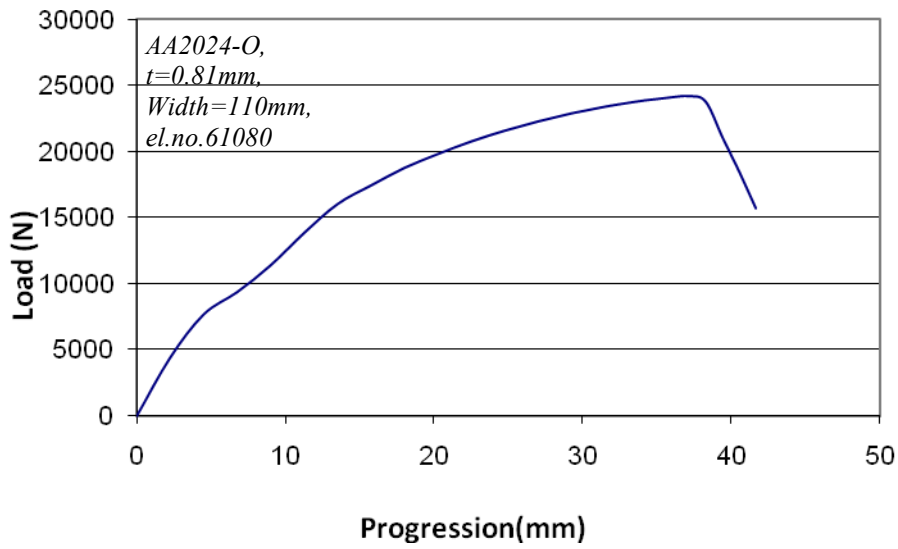
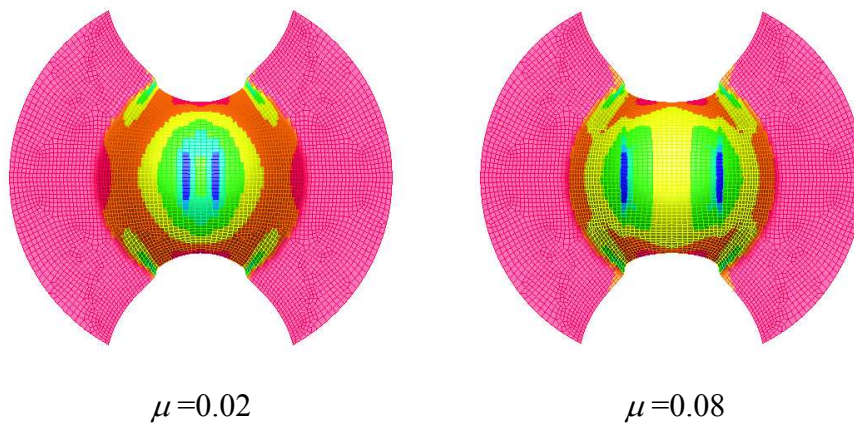


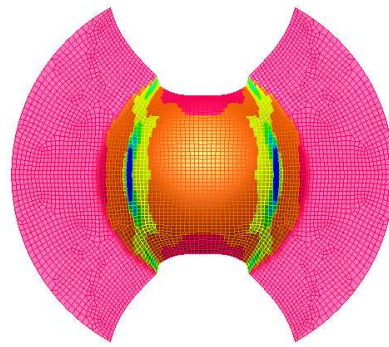
**Figure 7.24 Load vs. Punch Progression of Specimen W=110mm**

## 7.6 Effects of Process Parameters

### 7.6.1 Friction

Three friction conditions between the punch and the blank are simulated to see the effect of friction on the strain path and location of the necking region. As can be seen in Figure 7.25, three friction constants 0.02, 0.08 and 0.15 are studied.





$$\mu=0.15$$

**Figure 7.25 Effect of Friction on the Position of Necking**

The obtained results show that at lower friction constants the necking area is closer to the pole as in the case when  $\mu=0.02$ . For higher friction constant, at  $\mu=0.08$ , the necking area moves away from the pole and for  $\mu=0.15$  it moves further to the die radius. Therefore, in a real stamping process and FE analysis, the choice of the type of friction is highly influential on the deformations on the sheet.

### **7.6.2 Strain Hardening Coefficient**

The effect of strain hardening coefficient,  $n$ , on the strain distributions of the elements is studied. As can be seen in Figure 7.26, an aluminum specimen with 30mm width is analyzed using three different strain hardening coefficients 0.2, 0.2528 and 0.3.

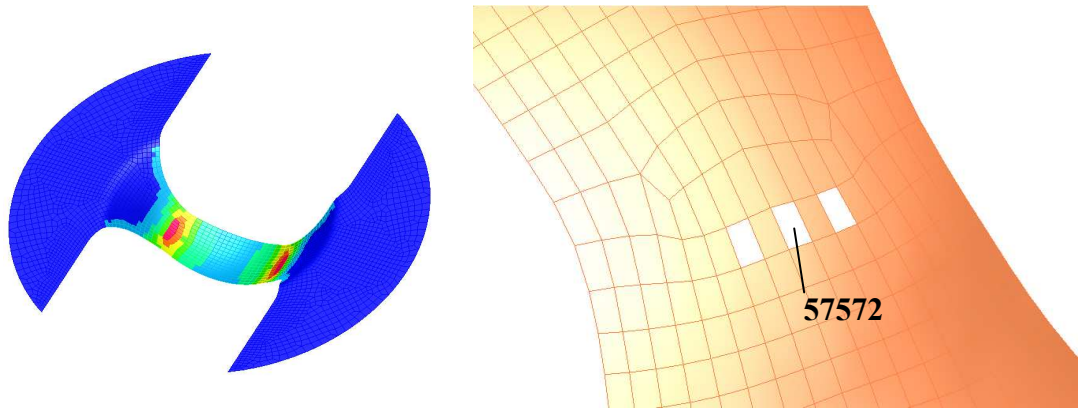


**Figure 7.26 Necking State of the Specimen W=30mm**

As shown in Figure 7.26, necking is observed at some distance from the pole. The position of the necking region does not vary with change of the strain hardening coefficient. However, if the element no.57572 is analyzed for different hardening coefficients, the thickness strain values vary. In Figure 7.27, the thickness history of element no.57572 throughout the deformation is plotted. After a critical punch progression reached, the thickness strain values become constant. As  $n$  increases, the increase in thickness strain stops at higher punch progression values. In addition, with increasing  $n$ , the final strain value of the element increases as well. Therefore, in the experiments and FE analysis, an accurate determination of the strain hardening coefficient from tensile tests is very important to obtain the right deformation characteristics.

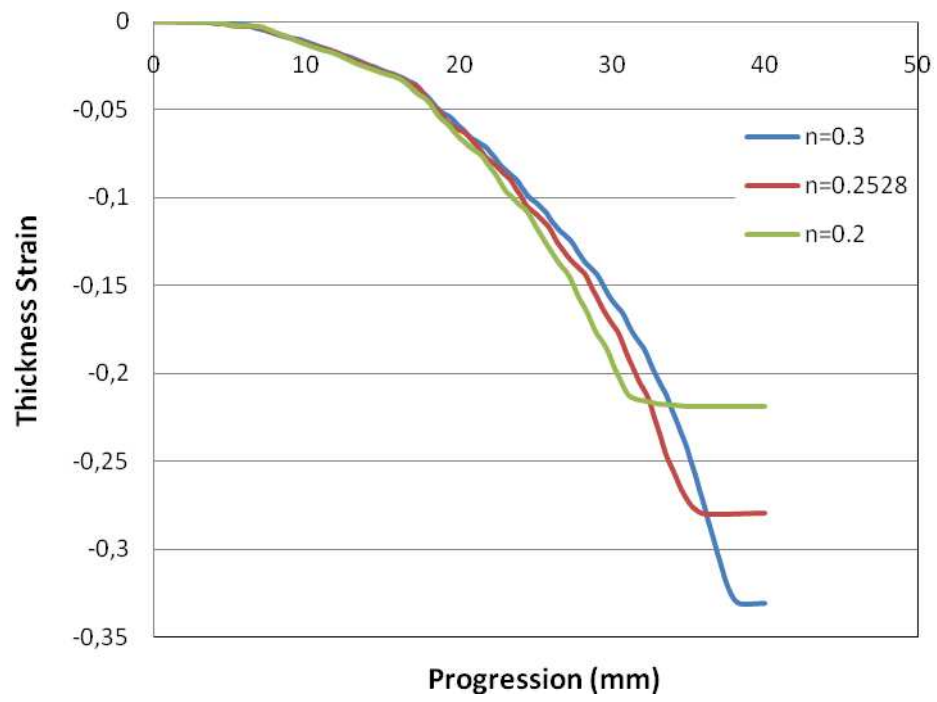


**Figure 7.27 Thickness Strain History of el.no.57572**

## CHAPTER 8

### CONCLUSION

Forming limit prediction is a very important issue that should be analyzed in detail in order to produce higher quality products in sheet metal forming processes. Especially in drawing and stretching operations, extensive knowledge of the deformation characteristics and the forming limits of a material are necessary in order to determine the best forming technique and the most suitable material to manufacture a higher quality product [15], [44].

Today, trial and error processes in determination of the forming limits of the sheet metals are still continuing although the last developments in sheet metal forming technology. This trial and error processes results in spending high amount time, material and producing high number of manufacturing tools in high costs. Therefore, several researches and studies are being done in this field to overcome these difficulties and disadvantages.

In this work, the formability of sheet metals, especially the failures due to tensile stresses, is predicted using theoretical and numerical methods. Nakazima testing method for the determination of FLD is simulated by applying strain propagation criteria using FE software Pam-Stamp 2G. In addition, theoretical methods which are Swift-Hill, Storen-Rice, Keeler and maximum load condition are used to obtain the forming limit curves of SAE 1006 and AA2024-O. The obtained FLDs are compared with the experimentally found FLDs in Figures 7.1 and 7.2 and the validity and effectiveness of each method are presented.

From the results of the present study, following conclusions can be made for the formability prediction of two materials, SAE 1006 and AA2024-O.

For SAE 1006, 7 specimens with different geometries are successfully analyzed in FEA and the location of the necking areas could be clearly observed. The following conclusions can be drawn:

- The most suitable criterion to predict the FLD is the strain propagation criterion using FEM as seen in Figure 7.1.
- Keeler's empirical model is also agreed well with the experimental curve.
- The predicted FLDs of Swift-Hill, Storen-Rice and maximum load condition underestimates the forming limits for SAE 1006 and therefore cannot be used as trusted methods for similar materials.

For AA2024-O, from 7 different specimens, plastic instability or necking could not be obtained for specimens having width 90mm, 130mm and 200mm. Therefore, full range of FLD for AA2024-O could not be determined using strain propagation phenomena and maximum load condition. The following conclusions can be drawn:

- None of the methods could describe the forming limits completely as seen in Figure 7.2
- Swift-Hill and Storen-Rice models give close results especially for the RHS of the FLD.
- Keeler's model, maximum load condition and strain propagation criterion overestimate the forming limits for AA2024-O.
- As previously mentioned, localized necking could not be observed for some specimens. The main reason for that could be the material properties ( $R_0$ ,  $R_{45}$ ,  $R_{90}$ ,  $n$ ) of AA2024-O or the process parameters such as finite element mesh size and friction conditions as shown in Figure 7.25.

Finally, general conclusions can be drawn throughout the study as:

- Predicting the forming limits of sheet metals theoretically are strongly depend on the type of the material considered. Furthermore, since these

theoretical models include several assumptions, they should be used cautiously.

- Strain propagation criterion could be applied to different types of materials for limit strain analysis and compared with the experimental findings.
- Frictional conditions have a crucial effect on the localization of necking. As shown in Figure 7.25, from  $\mu=0.02$  to  $\mu=0.15$  the localized region moves away from the pole.
- Integrating today's advanced FE analysis tools into the forming limit prediction process may substantially reduce the time and material wasted during the trial and error period and highly detailed formability analysis similar to real case could be performed accurately and eliminate the need and effort for the expensive experimental studies.
- For any manufacturing process, a suitable material and the right process parameters should be selected for a successful deformation behavior.

## REFERENCES

- [1] Marciniak, Z., Duncan, J., L., Hu, S., J., “Mechanics of Sheet Metal Forming”, Butterworth-Heinemann, London, 2002.
- [2] Marciniak, Z., “Assessment of Material Formability”, *Adv. Tech. Plasticity*, (1), 1984.
- [3] Banabic, D., Bunge, H., J., Pöhland, K., Tekkaya, A.E., “Formability of Metallic Materials”, Springer, Berlin, 2000.
- [4] Keeler, S., P., and Backhofen W., A., *Trans.ASM*, 1963, vol.56, pp.25-48.
- [5] Keeler, S., P., *Sheet Met. Ind.*, 1965, vol.42, pp. 683-91.
- [6] Swift, H., W., “Plastic Instability Under Plane Stress”, *J. Mech. Phys. Solids*, 1 1952, pp. 1-18.
- [7] Hill, R., *J. Mech. Phys. Solids*, 1952, vol.1, pp. 19-30.
- [8] Storen, S., Rice, J., R., “Localized Necking in Thin Sheets”, *J. Mech. Phys. Solids*, 1975, vol.23, pp.421-41.
- [9] Zhu, X., Weinmann, K., and Chandra, A.,”A Unified Bifurcation Analysis of Sheet Metal Forming Limits”, *ASME J. Eng. Mater. Technol.*, 2001, 123, pp. 329-333.
- [10] Chow, C., L., Jie, M., Hu, S., J., “Forming Limit Analysis of Sheet Metals Based on a Generalized Deformation Theory”, *Journal of Engineering Materials and Technology-Transactions of the ASME* 2003; 125; 260-5.

- [11] Sing, W., M., Rao, K., P., Swaminathan, K., "Influence of Limit Stress States and Yield Criteria on the Prediction of Forming Limit Strains in Sheet Metals", *Metallurgical and Materials Transactions* 1997, 28A (11), 2323-33.
- [12] Sing, W., M., Rao, K., P., "Role of Strain-Hardening Laws in the Predictions of Forming Limit Curves", *Journal of Materials Processing Technology* 63, 1997, 105-110.
- [13] Sing, W., M., Rao, K., P., "Study of Sheet Metal Failure Mechanism Based on Stress-State Conditions", *Journal of Materials Processing Technology* 67, 1997, 201-206.
- [14] Sing, W., M., Rao, K., P., "On the Prediction of the Effects of Process Parameters upon Forming Limit Strains in Sheet Metals", *International Journal of Mechanical Sciences*, Vol.42, 2000, pp.451-472.
- [15] Kaftanoğlu, B., "An Investigation of Stretch Forming in Relation to Deep-Drawing and Testing Sheet Metal", Ph.D. Thesis, Imperial College, London, 1966.
- [16] Goodwin, G., M., "Application of Strain Analysis to Sheet Metal Forming Problems in the Press Shop", *Society of Automotive Engineers*, 1968, No. 680093, 380-387.
- [17] Banabic, D., Aretz, H., Paraianu, L. and Jurco, P., "Applications of Various FLD Modeling Approaches", *Model. Simul. Mater. Sci. Eng.*, 2005, 13, pp. 759-769.
- [18] Banabic, D., Aretz, H., Comsa, D., S. and Paraianu, L., "An Improved Analytical Description of Orthotropy in Metallic Sheets", *Int. J. Plasticity*, 2005, 21 493–512.

- [19] Hora, P., Tong, L., and Reissner, J., “A Prediction Method for Ductile Sheet Metal Failure in FE-Simulation”, Proc. Numisheet’96 Conf., Dearborn, Michigan, 1996, pp. 252–6.
- [20] Arrieux, R., Brunet, M., Vacher, P., Nhat, T., N., “A Method to Predict the Onset of Necking in Numerical Simulation of Deep Drawing Operations”, CIRP Annals, Vol45, No.1, 1996, pp.255-258.
- [21] Toh, C., H., Kobayashi, S.,”Deformation Analysis and Blank Design in Square Cup Drawing”, Int. J. Mach. Tool Des. Res., Vol.25, No.1, 1985, pp.15-32.
- [22] Siguang Xu, Klaus, J., Weinmann, “Prediction of Forming Limit Curves of Sheet Metals Using Hill’s 1993 User-Friendly Yield Criterion of Anisotropic Materials”, International Journal of Mechanical Sciences, 9, 1998, 913–925.
- [23] Aghaie-Khafri, M., Mahmudi, R., “Predicting of Plastic Instability and Forming Limit Diagrams”, Int. J. Mech. Sci. 46, 2004, 1289-1306.
- [24] Wang L., Lee, T., C., “The Effect of Yield Criteria on the Forming Limit Curve Prediction and the Deep Drawing Process Simulation”, International Journal of Machine Tools and Manufacture, 46 (9), 2006, pp. 988-995.
- [25] Chakrabarty, J., Chen, F., K., “Influence of Loading Path on the Plastic Instability Strain in Anisotropic Plane Sheets”, Journal of Materials Processing Technology, 166 (2), 2005, pp. 218-223.
- [26] Bleck, W., Deng, Z., Papamantellos, K., Gusek, C., O., “A Comparative Study of the Forming Limit Diagram Models for Sheet Steels”, Journal of Materials Processing Technology, 83 (1-3), 1998, pp. 223-230.
- [27] Slota, J., Spišák, E., “Comparison of the Forming Limit Diagram (FLD) Models for Drawing Quality (DQ) Steel Sheets, Metalurgija, 44 (4), 2005, pp. 249-253.

- [28] Pepelnjak, T., Kuzman, K., “Numerical Determination of the Forming Limit Diagrams, J. Achiev. Mater. Manuf. Eng., Vol. 20, 2007, pp. 375-378
- [29] Huang, Y., M., Tsai, Y., W., Li, C., L., “Analysis of Forming Limits in Metal Forming Processes”, J. Mater. Process Technol., 201, 2008, 385–389.
- [30] Jie, M., Cheng, C., H., Chow, C., L., Chan, L., C., “Limit Dome Height and Failure Location of Stainless Steel Tailor-Welded Blanks”, Int. J. Mech. Sci., 2007, vol.221, 1497-1506.
- [31] Considere, A.,”Use of the Iron and Steel in Buildings (in French)”, Ann.des Ponts as Chaussees, 9, 1885, 574-575.
- [32] Hosford, W., F., ”On Yield Loci of Anisotropic Cubic Metals,” 7th North Amer. Metalworking Res. Conf. Proc., SME, Dearborn, 1979.
- [33] Keeler, S., P., “Plastic Instability and Fracture In Sheet Stretched Over Rigid Punches”, Thesis, Massachusetts Institute of Technology, Boston, MA 1961.
- [34] Gensamer, M., “Strength and Ductility”, Trans. ASM, 36, 1946, 30-60.
- [35] Keeler, S., P., Brazier, W., G., “Relationship Between Laboratory Material Characterization and Press-Shop Formability”, Micro Alloying, 1975, 21-32.
- [36] Levy, S., B., “A Comparison of Empirical Forming Limit Curves for Low Carbon Steel with Theoretical Forming Limit Curves of Ramaekers and Bongaertsi”, IDDRG WG3, Ungarn, 13-14 June 1996.
- [37] PAM-STAMP 2G User’s Manual, ESI-Software, France, October, 2002.
- [38] PAM-STAMP 2G Reference Manual, ESI-Software, France, October, 2002.

[39] “Metallic materials- Guidelines for the determination of forming limit diagrams”, ISO Standard 12004-2.

[40] Kaftanoğlu, B., “Determination of Coefficient of Friction Under Conditions of Deep-Drawing and Stretch Forming”, *Wear*, 25, 1973, 177-188.

[41] “ASM Handbook, Volume 1, Properties and Selection: Irons, Steels, and High Performance Alloys”, ASM International Handbook Committee, USA, 1993.

[42] “ASM Handbook, Volume 2, Properties and Selection: Nonferrous Alloys and Special Purpose Materials”, ASM International Handbook Committee, USA, 1992.

[43] Metal Forming Center of Excellence-Atılım University, Ankara, TURKEY.

[44] Kaftanoğlu, B., Alexander, J.M., “On Quasistatic Axisymmetrical Stretch Forming”, *International Journal of Mechanical Sciences*, 12, 1970, 1065-1084.

## APPENDIX A

### HILL'S GENERALIZED YIELD CRITERION AND DIFFERENT SPECIAL CASES

Hill's yield criterion is given as:

$$f|\sigma_2 - \sigma_3|^M - g|\sigma_3 - \sigma_1|^M - h|\sigma_1 - \sigma_2|^M + a|2\sigma_1 - \sigma_2 - \sigma_3|^M + b|2\sigma_2 - \sigma_3 - \sigma_1|^M + c|2\sigma_3 - \sigma_1 - \sigma_2|^M = \bar{\sigma}^M = f(\bar{\sigma}) \quad (\text{A.1})$$

For plane stress condition and anisotropic material, Hill proposed four special cases to encompass the anomalous behaviour of materials such as aluminum.

The conditions for the five cases are as follows:

Case 1:  $a = b = h = 0$  and  $f = g$  ;

Case 2:  $a = b$  and  $f = g = c = 0$  ;

Case 3:  $a = b, f = g$ , and  $h = c = 0$  ;

Case 4:  $a = b = f = g = 0$  ;

Case 5:  $a = b = c = 0$  and  $f = g$  .

For case 1, Eqn(A.1) becomes:

$$(1 + 2R)\left(|\sigma_1|^M + |\sigma_2|^M\right) - R|\sigma_1 + \sigma_2|^M = (1 + R)\bar{\sigma}^M \quad (\text{A.2})$$

For case 2, Eqn(A.1) becomes:

$$\frac{1}{(1+R)(2^{M-1}-1)} \left( |2\sigma_1 - \sigma_2|^M + |2\sigma_2 - \sigma_1|^M \right) + \left[ 1 - \frac{(2^M + 1)}{(1+R)(2^{M-1}-1)} \right] (|\sigma_1 + \sigma_2|^M) = \bar{\sigma}^M \quad (\text{A.3})$$

For case 3, Eqn(A.1) becomes:

$$\frac{R}{(1+R)(2^{M-1}-1)} \left( |2\sigma_1 - \sigma_2|^M + |2\sigma_2 - \sigma_1|^M \right) + \left[ 1 - \frac{R(2^M + 1)}{(1+R)(2^{M-1}-1)} \right] (|\sigma_1|^M + |\sigma_2|^M) = \bar{\sigma}^M \quad (\text{A.4})$$

For case 4, Eqn(A.1) becomes:

$$|\sigma_1 + \sigma_2|^M + (1+2R)|\sigma_1 - \sigma_2|^M = 2(1+R)\bar{\sigma}^M \quad (\text{A.5})$$

For case 5, Eqn(A.1) becomes:

$$|\sigma_1 + \sigma_2|^M + R|\sigma_1 - \sigma_2|^M = (1+R)\bar{\sigma}^M \quad (\text{A.6})$$